Completion of the Muon Veto for the Dortmund Low Background Facility and Proton Activation Measurements on Irradiated Metals from Proton Beam Therapy

Dissertation
zur Erlangung des akademischen Grades
eines Doktors der Naturwissenschaften
der Fakultät Physik
an der Technischen Universität Dortmund

vorgelegt von

CHRISTIAN NITSCH

Lehrstuhl für Experimentelle Physik IV
Fakultät Physik

technische universität
dortmund

Dortmund, Oktober 2018

Completion of the Muon Veto for the Dortmund Low Background Facility and Proton Activation Measurements on Irradiated Metals from Proton Beam Therapy

Dissertation zur Erlangung des akademischen Grades
eines Doktors der Naturwissenschaften
der Fakultät Physik
an der Technischen Universität Dortmund

vorgelegt von

CHRISTIAN NITSCH
Lehrstuhl für Experimentelle Physik IV
Fakultät für Physik
TU Dortmund

Teilergebnisse dieser Arbeit waren Gegenstand verschiedener
Veröffentlichungen und Tagungsbeiträge.
Eine Liste befindet sich am Ende der Arbeit ab Seite 163.

Vorsitzender der Prüfungskommission:	Prof. Dr. M. Schneider, TU Dortmund
Erstgutachter:	Prof. Dr. K. Kröninger, TU Dortmund
Zweitgutachter:	Prof. Dr. Dr. W. Rhode, TU Dortmund
Vertretung der wiss. Mitarbeiter:	Dr. B. Siegmann, TU Dortmund
Termin der mündlichen Prüfung:	17. Dezember 2018

Abstract

The Dortmund Low Background Facility is a highly sensitive gamma ray spectrometry system, operated in a low-background environment, which enables the measurement of traces of radioactivity with high precision.
A high purity germanium detector is set up within an artificial overburden, equivalent to 10 meters of water. This outer shielding reduces the contribution from cosmic muons during the measurement. Signals induced by cosmic muons that penetrate this shielding are suppressed by an active cosmic muon veto detector. Environmental radioactivity is effectively shielded from the germanium detector with an multi-layered inner shielding, which is featuring a neutron absorber inside a massive lead shielding.
During this work, the muon veto detector is completed with newly installed plastic scintillator detectors. The upgraded veto detector in combination with passive shielding techniques results in a remarkably low residual background count rate of $1.855(3)\,\mathrm{counts}/(\mathrm{kg_{Ge}min})$ between 40 keV and 2700 keV. Subsequently, detection limits below 1 mBq/kg are achieved. A detailed analysis of the remaining background spectrum is presented within this work, including Monte Carlo simulations, that are used to estimate the origins of different background contributions.
The irradiation of brass apertures wich high energetic protons during clinical proton beam therapy can create a radiation protection risk for personnel and patients. In cooperation with the West German Proton Therapy Centre Essen in Essen, Germany several metal samples are irradiated. Due to the high sensitivity of the Dortmund Low Background Facility, relatively short-lived radionuclides are identified and analysed within two irradiated brass aperture samples. The results, presented in this work, are also compared with FLUKA simulations and used for the estimation of the ambient dose rate caused by the activated samples.

Contents

1. Introduction

Low-level counting techniques were first used for the radiocarbon dating measurements developed by W. F. Libby, who used shielded gas counters for the method for which he later was awarded the Nobel prize in chemistry in 1960 [Noba, Lib64]. Even then, Libby's detector system featured a cosmic ray veto system, that actively reduced the contribution from cosmic radiation to the system's background [Lib64].

Through gas counters and liquid scintillation spectrometers the development lead to semiconductor radiation detectors and mass spectrometers, which mark the state of the art in low-level techniques today [The96, Pov18]. This variety of different detection techniques enables low-level applications to cover a wide span of fields from radiocarbon dating and the analysis of environmental processes to questions in fundamental physics and applications in medical physics.

Many of the fundamental questions in physics require the experimental detection of rare events. If these events are expected in the low energy region, ranging between approximately 1 keV and 5 MeV, a low-background environment is mandatory to perform sophisticated experiments, since this is the energy region where also most of the radioactive decay energies are located. Most of these experiments are located in laboratories deep underground to minimise the background contribution due to cosmic radiation. In order to minimise the contributions, brought into the experiment by detector components and shielding materials, radiopurity screenings of all these materials are performed by at least one of many different radiopurity assay methods. Gamma ray spectrometry, based on high purity germanium (HPGe) detectors, is commonly employed for this task, due to the excellent energy resolution and good sensitivity that is achieved in non-destructive measurements of large samples.

Some of the above mentioned questions arise around the nature of the neutrino. Neutrino less double beta decays, for example, are searched for (e.g. GERDA [ABB$^+$18], MAJORANA [A$^+$14, AAA$^+$18a], COBRA [E$^+$16b, EFG$^+$16]) to pro-

vide an answer to the question if the neutrino is its own anti particle, a so-called Majorana particle, and possibly determine its mass. The best limit for the neutrino less double beta decay in ^{76}Ge has recently been set to 8×10^{25} years [AAA+18a].

New neutrino physics can, for example, also be investigated via coherent elastic neutrino-nucleus scattering, which has been observed recently by the COHERENT experiment [A+17a, FLRX18]. This observation will soon be probed by the CONUS experiment, where the experience from low-background HPGe detectors, which are used primarily for radiopurity screenings (e.g. GIOVE [HWH+15]), is employed for the detection based on reactor neutrinos.

Another example for the employment of low-background environments is the search for Dark Matter signals, e.g. via nuclear recoil signals due to Dark Matter-Matter interactions, which are investigated by CRESST [ABB+16], XENON [A+17b] and other experiments.

Due to the increasing sensitivity of these experiments, radio assay and prescreening facilities, such as the DLB, have to achieve higher sensitivities as well.

The low-level analysis of radionuclides has additional applications in other sciences, such as environmental physics. These studies are often limited by the techniques employed for sampling and analysis of radionuclides with very low levels of activity. Applications range from the routine screening of food to the detection of anthropogenic tracer radionuclides in water to improve the understanding of environmental and marine processes, e.g. ground water origins or water circulation processes in the ocean [Pov18].

After more than 60 years, the levels of nuclear weapon tests induced radionuclides have decreased considerably. However, the ^{137}Cs content in the atmosphere is investigated routinely, also due to nuclear accidents, such as Chernobyl (1986) and Fukushima (2011). In addition to the trace amounts of activity, the data needs to be highly accurate and precise. This requires sensitivities well below the µBq/kg level, which can be achieved by lowering the background of the detection system.

A high sensitivity in terms of a radionuclide's activity, can be transferred into a high sensitivity in terms of half-lives elapsed. This can be useful, for example, in medical physics where the radionuclides of interest are often highly active but decay rather quickly. Therefore, highly sensitive detector systems are required to be able to detect sufficient signals, even after several half-lives have passend and

the activity is decreased considerably.

The Dortmund Low Background Facility (DLB) was designed and commissioned by T. Neddermann and H. Gastrich in 2009 [Ned09, Gas09]. It features a massive outer shielding, corresponding to an overburden of 10 meter water equivalent (m.w.e.), which reduces the intensity of cosmic muons by a factor of two, while other cosmic ray components are reduced even stronger. A multi-layered inner shielding is designed, with special regards to the location at this shallow depth, to reduce the background induced by environmental radiation and neutrons. An additional massive background reduction is achieved by the active cosmic muon veto detector, that covers the inner shielding and suppresses muon-induced events in the residual spectrum. The core of the DLB is a HPGe detector with 60 % relative efficiency.

This setup enables detailed radiopurity screening of different materials, with sensitivities well below 1 Bq/kg, which is used to support the development of the COBRA experiment and for the analysis of other materials, e.g. in the context of dosimetric applications in medical physics.

Chapter 2 gives an overview of different techniques for material radiopurity assays. The main aspects of gamma ray spectrometry are discussed and the analysis standards for gamma ray spectra are introduced.

Chapter 3 focusses on the different contributions for background radiation in low-level applications. The environmental radioactivity, consisting of primordial, airborne and anthropogenic radionuclides, is discussed, as well as cosmic ray induced detector events. Due to their high penetration power, cosmic muons are largely contributing to the background of detector systems that are not situated deep underground. Since the DLB is covered by 10 m.w.e., the reduction of cosmic muon induced events is crucial to achieve the desired sensitivity.

The DLB's experimental set up and its different shielding components are presented in Chapter 4. Additionally, the data acquisition and analysis software is briefly describes.

Monte Carlo (MC) simulations based on Geant4 are routinely used for the DLB to determine the full energy peak (FEP) detection efficiency, which is necessary to obtain accurate results from the spectrometric measurements. These simulations are explained in Chapter 5. Due to the large impact of cosmic muons for the DLB's residual background, MC simulations are performed to estimate the resulting background spectrum induced by cosmic muons. The results are discussed in

Section 5.2.

The muon veto detector of the DLB has been upgraded several times since its initial setup. The latest upgrade that leads to the completion of the muon veto detector is presented in Chapter 6. In Sections 6.1 and 6.2, new scintillation detectors are characterised and the integration into the existing setup is described. Section 6.3 focusses on the reduction of the residual background, that is achieved by different shielding techniques of the DLB.

In Chapter 7 the residual background is analysed base on an extensive measurement of the background after completion of the muon veto detector. Peaks in the remaining spectrum are discussed and the composition of different background contributions is estimated with MC simulations. The DLB is routinely used for different gamma spectrometric measurements, which are exemplary shown in Section 7.3.

During clinical proton beam therapy applications, brass apertures are used to form the lateral beam profile. These brass apertures are subject to radioactivation when irradiated with high energetic protons, which poses an radiation protection risk for personnel and patients that are exposed to the activated apertures. In Chapter 8 spectrometric measurements of activated materials are discussed, that are performed in cooperation with the WPE.

Finally, a summary of the results of this work is given in Chapter 9.

2. Radiopurity Assaying and Gamma Ray Spectrometry

Many fields of modern science as well as a variety of applications rely on detailed information about the composition of a material. If that material is thought to be used as a construction material for a low-level physics experiment for example, elaborate knowledge about any impurities is crucial. This information gains importance especially if any of these materials may introduce radioactive contaminations into the experiment's environment. These so-called radioimpurities may raise the intrinsic background of the experiment to an unacceptable level. Impurities can come from the raw material itself, which is often not radiopure from the beginning, or they are introduced later, either during the production processes or by accumulation of cosmogenic activation due to the exposure to cosmic rays.

In this chapter a brief overview of several spectrometry techniques used for radiopurity assays is given. Attention is turned to gamma ray spectrometry with HPGe detectors, which is not only a commonly used non-destructive assay technique, but also the main purpose of the DLB, which is presented in this work. A more extensive discussion on gamma ray spectrometry can be found e.g. in [Gil08], information on alternative techniques can be found in [The96, Heu95, Pov18]. N. Abgrall et al. give a convenient overview about how different low-level detection methods were employed for radiopurity assays for the MAJORANA [A$^+$14, AAA$^+$18a] experiment [AAA$^+$16].

2.1. Radiopurity assay techniques

Several different techniques for the investigation of a material's composition are available with various advantages and disadvantages. They are chosen depending on type and state of matter of the material that is to be investigated, the expected amounts of impurities, the type of radiation or the needed detection-sensitivity level. In general, sample sizes and measurement time are

often limited, so that a low-background environment is of crucial importance to reach the necessary sensitivity during the radiopurity assay measurements. A short overview of the available techniques is given in the following sections.

A very sensitive method that may be applied is **mass spectrometry**, where, amongst others, accelerator mass spectrometry (AMS) [FFF+15] or inductively coupled plasma mass spectrometry (ICPMS) [NCDDV17] should be mentioned here. The philosophy of measurement in mass spectrometry is here changed from the counting of radioactive decays to direct counting of atoms instead [Pov18]. Thereby very high sensitivities, e.g. for primordial radionuclides (see Section 3.1) can be achieved. Measurements of concentrations as low as 15 ppt (parts per trillion, 1×10^{-12} g/g) for thorium and 0.08 ppt for uranium are reported on in AMS measurements of ultra pure copper for example. Converted to specific activities these concentrations result in 59 µBq/kg for ^{232}Th and 1 µBq/kg for ^{238}U respectively [FFF+15]. ICPMS measurements at the Laboratori Nazionali del Gran Sasso (LNGS) are reaching even lower detection limits for uranium and thorium concentrations in the range of 0.01 ppt. Although the sensitivity for potassium is limited since the plasma is usually made from argon gas (atomic weight of 39.95 u), ICPMS detection limits of 1 ppt are achieved [NCDDV17]. These sensitivities for mass concentrations translate to specific activities of only a few nBq/kg for ^{238}U,^{232}Th and ^{40}K. Due to the very complex sample preparation that is necessary for the separation of the elements of interest, there is a relatively high risk of sample contamination. Although only very small sample sizes are sufficient for the measurement, mass spectrometry is a destructive method.

Today, AMS is used for the direct counting of carbon atoms in the aforementioned radiocarbon analysis. Due to the half-life of ^{14}C of 5730 years it is much more effective to directly count the ^{14}C atoms than to wait for their decay. Precisions of about 0.35 % of ^{14}C content are achieved, which translate into uncertainties of only 30 a for sample masses of only 500 µg [PBJV08].

Liquid scintillator spectrometry is sensitive for both alpha and beta decaying radionuclides, especially if the sample matrix is liquid or soluble. Due to this very efficient counting geometry in combination with a low background, this method can reach very high sensitivities of 1 mBq/kg for uranium and thorium [LK12]. Newly developed ultra low background (ULB) systems reach background levels of about 50 counts/d between 3 and 3600 keV which enable detection limits, e.g. for tritium, of about 250 mBq/kg [EAB+15, EOA+17]. On

the other hand, the poor energy resolution of liquid scintillators makes it difficult to analyse more complex spectra, especially if several nuclides with similar energies are present in the sample.

Dedicated detectors for **alpha spectrometry** are usually silicon based with small thicknesses and relatively large surface areas of 10 mm in diameter [PBJV08]. Since alpha particles of the natural occurring decay chains have energies between 4 MeV and 9 MeV, background is usually limited this energy region. Background levels of only 10.9 counts/d have been achieved in this energy region enabling for example precision measurements of alpha decaying radionuclides with half-lives in the region of 1×10^{15} a [WZK+17]. Due to the very limited penetration ranges of alpha particles, only very thin samples are used, which, in general, confines the sample mass and thereby the achievable sensitivity. Additionally, the measurement chamber needs to be evacuated to limit interactions with any residual gas, which increases the complexity of the detection system.

Gamma ray spectrometry is based on the detection of characteristic photons, so-called gamma rays, that are emitted during the de-excitation of the nucleus that often remains from the alpha or beta decay of a mother nuclide. Subsequent gamma rays provide a characteristic signature of this preceding decay, and are therefore often associated directly to the decay of the mother nuclide. Prominent example is the 661.6 keV gamma ray that is emitted with an intensity of 85 % by ^{137*}Ba [NNDCN18]. The gamma ray however, is often directly attributed to the beta decay of ^{137}Cs that results in the excited state of ^{137}Ba. Although this simplified notation might be misleading in some cases, it is the commonly used notation and therefore also used in this work.

Gamma ray spectrometry provides a non-destructive measurement with very high energy resolution, especially when HPGe detectors are used, enabling the analysis of several nuclides during the same measurement. While the handling and preparation of samples is relatively easy, larger samples are, in general, beneficial. When intrinsically very radiopure germanium crystals are used as detectors in an ultra low-background environment, sensitivities up to 1 µBq/kg, or about 1 ppt are achievable for ^{238}U and ^{232}U [Lau17]. In order to be directly detectable with gamma ray spectrometers, the radionuclide's decay under investigation has to be accompanied by the emission of gamma rays with sufficiently high intensity. Since common nuclides of interest, e.g. ^{238}U, ^{232}Th or ^{210}Po, do not

emit gamma rays during the de-excitation of their daughter nuclei, those decays are not directly observable. However, if these nuclides are part of decay chains (e.g. primordial decay chains discussed in Section 3.1) indirect detection may be enabled through gamma rays that are emitted by daughter nuclides further down the chain. This spectrometry method is the only technique able to detect a possible disequilibrium (see Section 3.1.1) in one of the naturally occurring decay chains.

Neutron activation analysis (NAA) can enable the direct measurement of a radionuclide due to the conversion into nuclides with shorter half-lives and higher activities, respectively. After the capture of a thermal neutron by the nuclide of interest, the mass number is increased by one and the nucleus can be in brought into an excited state, potentially emitting prompt gamma rays. Otherwise the produced nucleus can undergo a beta decay which can result in an excited daughter nucleus that is subsequently emitting characteristic gamma rays. This has been used on long-lived radionuclides such as ^{129}I, ^{232}Th and ^{238}U in environmental samples in the past [Pov17]. Recently measurements of the latter have been performed on copper samples with sensitivities in the range of 1 mBq/kg [KKP17]. The neutrons can be produced e.g. inside a nuclear reactor and if a certain nuclide is of interest the energy can be tuned according to the neutron capture cross section to increase the sensitivity.

The sensitivity for radioimpurities that is needed for construction materials for the next generation of underground experiments is reaching into the 10 nBq/kg scale, which is about two orders of magnitude better then currently available detection sensitivity with gamma ray spectrometry [Pov17]. Until now only mass spectrometry methods enable screening measurements with sufficient sensitivities, however, only under favourable measurement conditions. Today's gamma ray spectrometers are limited in sensitivity mostly by the residual background levels of the detector systems, and substantial improvements are needed here since the sensitivity is proportional only to the square root of the background (compare Equation (2.13)). The most searched for radionuclides are usually the same that contribute to the background of the detector systems due to material contaminations: ^{238}U and ^{232}Th decay chains with their daughter radionuclides and ^{40}K.

2.1.1. Gamma ray spectrometry

For the following sections the focus will be on the method of gamma ray spectrometry for the detection of radioimpurities in the low-level environment.

Scintillation Detectors

When ionising radiation passes trough a scintillating material, a few percent of the particle's energy are deposited in the medium via ionisation and excitation of the scintillator's atoms. During the atoms de-excitation, fluorescent light is emitted, which then can then be detected by a photomultiplier tube (PMT) attached to the scintillating medium. Scintillation detectors are therefore build with three main components, independent of the type of scintillator used. The scintillator itself is read out by a PMT that is connected to the supporting and readout electronics. The surface of the scintillator is usually protected from the environment and covered with reflecting surface, to reduce the loss of fluorescence photons. Initially-released electrons from the photocathode are then accelerated and multiplied by a number of dynodes inside the PMT. Scintillating materials are characterised by several different properties like energy-to-light-conversion factors, transparency to their own fluorescence light, their decay time or the photon absorption probability [The96]. Due to basic differences in the scintillation process, scintillating materials are categorised into organic scintillators and inorganic scintillators.

If the scintillation process is based on the electronic band structure of a crystalline structure it is called an **inorganic scintillator**. Examples for such crystals besides the commonly used sodium iodide (thallium-doped) (NaI(Tl)) are caesium iodide (thallium-doped) (CsI(Tl)), lanthanum bromide ($LaBr_3$) or bismuth germanate, $Bi_4(GeO_4)_3$ (BGO). All of those can be operated at room temperature with different properties and preferred usages. In some cases an activator impurity, e.g. thallium in NaI(Tl) or CsI(Tl), is used to shift the energy of the emitted photons and prevent re-absorption inside the bulk material [Gil08]. Compared to semiconductor detectors the costs for comparable detection efficiency are in general lower. The tradeoff is a much worse energy resolution of about 60 keV at 661.7 keV for NaI(Tl) [Gil08].

NaI(Tl) is the most common inorganic scintillator since it benefits from the high density of $3.67\,\mathrm{g/cm^3}$ which results in a high detection efficiency, even for relatively high-energetic gamma rays. For a long time, the cylindrical NaI(Tl) detec-

tor of 76 mm diameter and 76 mm height (sometimes referred to as 3 inch $\times$ 3 inch) has been the standard gamma-ray spectrometer detector [Gil08]. It is still used as a reference for the calculation of the relative efficiency of HPGe germanium detectors (see Section 2.2.1).

Due to intrinsic impurities inorganic scintillators are usually not directly used for low-level applications or gamma ray spectrometry. NaI(Tl) for example suffers from impurities due to the thallium-doping and because of the chemical similarity of potassium and sodium, ^{40}K can be found inside the crystals bulk material. ^{214}Bi for example is frequently found in BGO detectors. If no special processing is applied to the glass of PMTs, it is known to be subject to contamination with primordial radionuclides as well.

Sometimes however, NaI(Tl) is used for special purpose multi-detector setups such as anti-Compton systems. Active background suppression techniques are then used to overcome the drawback of the scintillator's impurities. Gamma rays, that are leaving the main detector, e.g. a HPGe detector, due to incomplete absorption by Compton scattering, are detected in the second high efficiency detector that is surrounding the main detector. If the data acquisition is then stopped from recording the event of incomplete absorption, the Compton continuum is reduced and the remaining FEPs can be measured with lower uncertainty and better sensitivity.

Organic scintillators are mostly used in form of plastics or liquids. The fluorescent material is embedded into an organic solvent or polymer base, such as toluene or benzene. The solvent is often mixed with an additive, a so-called wavelength shifter, to enhance light emission in the visible spectral regions, which are more suitable for the detection by PMTs. Due to a lower light yield compared to inorganic scintillators, the achievable energy resolution is generally worse for organic scintillators. On the other hand, their decay time is generally two orders of magnitude shorter and on the scale of only a few nanoseconds [The96]. This makes them especially beneficial in the use for trigger systems, such as anti cosmics veto detectors, which are used for active background reduction in low-background systems. Additionally, organic scintillators are relatively low priced and can be produced in practically any desired shape.

Recently, polyethylene naphthalate (PEN) has been identified as newly available scintillator material, that exceeds the performance of conventional organic scintillators without the need for a wavelength-shifter [NSTS11]. Since it has been found to be fairly radiopure it may be used as self-vetoing material in

low-background experiments such as GERDA [MEF+18]. However, a potential contamination with ^{40}K has been reported. In Section 7.3 the results of a screening measurement of a sample of PEN pellets are presented. Additionally, PEN proves to be a superior choice for dosimetry applications in brachytherapy [FFEE15].

The plastic scintillators used for the anti cosmic muon veto detector of the DLB are the multi purpose scintillators EJ-200 (*ELJEN TECHNOLOGY*) and BC-408 (*Saint-Gobain Crystals*). Both scintillation materials consist of polyvinyl-toluene with their major properties listed in Table 2.1 [ELJ, Sai18]. The properties of the inorganic NaI(Tl) crystal are given for comparison.

Table 2.1.: Properties of organic and inorganic scintillation materials. Data from [Gil08, ELJ, Sai18]. Wavelength denotes the wavelength of maximum emission.

material	polyvinyl-toluene (EJ-200, BC-408)	Sodium Iodide (NaI)
scintillator type	organic (plastic)	inorganic (crystal)
light yield [photon/keV]	10	38
wavelength [nm]	425	415
decay time [ns]	2.1	230
density [g/cm3]	1.023	3.67

Semiconductor Detectors

According to the structure of their electronic bands, materials are categorised into insulators, conductors and semiconductors. The electrons inside a material are disposed on specific energy bands with fixed numbers of electrons. The highest populated energy band is called valence band, the next available energy band is called the conduction band. The region between both bands is forbidden for electrons and called band gap. For semiconductors however, the band gap is relatively small and in the order of 1 eV [Gil08].

An absolutely pure semiconductor would have an equal number of electrons and holes due to thermal excitation and would be called an intrinsic semiconductor. But since absolute purity is not possible, the impurities have to be considered as well. Impurities with lower valency than the semiconductor material are

called acceptor impurities, and detectors with this type of impurity are called p-type. If the impurities have higher valency than the material, they are called donor impurities, and the semiconductor is called n-type. The active addition of impurities is called doping [Gil08]. If p-type and n-type regions are brought together, electrons from the n-type region will diffuse into the p-type region and recombine with holes until this process is stopped by the diffusion voltage. The resultant depletion region is the sensitive part of a semiconductor detector. It can be enlarged by applying an external (high) voltage to the detector.

An important contribution to the energy resolution of a radiation detector is the number of electron-hole pairs, that is produced per absorbed energy. It is given by the average energy necessary for the production of an electron-hole pair, that is relatively small for semiconductor materials. Typical values are: 2.96 eV for germanium, 3.62 eV for silicon, 4.64 eV for Cadmium Zinc Telluride, CdZnTe and 170 eV for NaI(Tl) [Gil08]. Another important component of the energy resolution is the mobility of electrons and holes inside the material, that ensures the efficient and quick collection of produced electrons and holes before their recombination.

Silicon is the most commonly used semiconductor in science and technology. Although silicon is available in high purity at reasonable costs, its main disadvantage for the detection of gamma rays is its low atomic number and therefore low detection efficiency. However, silicon detectors are often used in the detection of low-energy gamma rays and X-rays. Other examples for semiconductors used for radiation detection are Cadmium Telluride, CdTe or CdZnTe. Due to their higher atomic numbers, their absorption coefficients and subsequent detection efficiency is larger. Their size however, is limited by the intrinsic charge carrier mobility, which is considerably lower than for germanium for example, and since the holes are subject to trapping, these detectors suffer from charge collection problems. Additionally, the energy of about 4.64 eV that is needed to create charge carriers is higher than in germanium [Gil08]. The coplanar grid (CPG) technology [Luk94] is used to compensate for those drawbacks and COBRA uses newly developed 6 cm^3 CdZnTe detectors with four CPGs per detector. An energy resolution of about 33.3 keV (2.5 %) at 1332.5 keV has already been achieved [E+16a].

When germanium detectors were not available with insufficient purity of the

crystal, lithium drifting was used for the compensation for the impurity. This resulted in less good energy resolution of only 4 to 5 keV at 1332.5 keV [Gil08]. Today, the most substantial argument for HPGe detectors is the superior energy resolution compared to all other semiconductor detectors, which is based on the small amount of energy (2.96 eV) that is needed for the production of an electron-hole pair inside the crystal [Gil08]. The energy resolution at 661.7 keV (^{137}Cs) for example is 1.4 keV and 1.8 keV at 1332.5 keV (^{60}Co), measured with the DLB's HPGe detector. In addition to different parameters of the germanium crystal itself, readout electronics are influencing the final energy resolution. The small energy gap however, makes germanium detectors not operable at room temperature, since the leakage currents would be too high, when electric fields are applied. Germanium detectors are therefore cooled with liquid nitrogen during operation. As it was mentioned before, the relative efficiency of a germanium detector is given in comparison to a NaI(Tl) detector with a diameter of 7.62 cm and a height of 7.62 cm. It scales with about 1 % per 4.3 cm^3 or 23 g of germanium [Gil08].

2.2. General aspects of gamma ray spectrometry

Measurements in gamma ray spectrometry rely on the absorption of gamma rays and their energy transfer to electrons of the detector material. The three main processes for these interactions are the photo effect, Compton scattering and electron-positron pair production. In general, the cross sections depend on the atomic number Z of the absorber material and the gamma ray's energy. For energies below about 200 keV, the photo effect is the dominant interaction mechanisms of gamma rays in germanium. At mid-range energies, most of the gamma rays interact via Compton scattering. The production of electron-positron pairs is dominating the interactions above energies of about 5 MeV.

In the following sections some important aspects of gamma ray spectrometry, that are used in this work, are discussed briefly. A more comprehensive overview and discussion can be found in [Gil08].

2.2.1. Detection efficiency

The **absolute FEP detection efficiency** ϵ is one of the most important values for gamma ray spectrometry. It gives the ratio between the detected net count rate in the FEP area R_n that is measured in the time t_M and the emitted gamma rays of

a certain energy per time, that is given by the source activity A and the emission probability p_γ:

$$\epsilon = \frac{R_n}{A \cdot p_\gamma}. \tag{2.1}$$

The detection efficiency is affected by the detector-to-sample geometry, the solid angle covered by the detector, as well as self absorption effects inside non-point-like sources. It also includes the intrinsic efficiency of the detector that describes the absorption of gamma rays inside the germanium detector itself, which is mainly depending on the detector geometry and the gamma ray's energy.

The practical determination of ϵ is discussed in Section 5.1. In this work, the term detection efficiency will refer to the absolute FEP detection efficiency.

Another type of efficiency that is often referred to is the **relative efficiency** that is given to characterise HPGe detectors. This value compares the detection capabilities of a germanium detector to a NaI(Tl) detector, because "in the beginning there was sodium iodide" [Gil08]. A standard test configuration (IEEE 325-1996) is used for the comparison of the counts for the 1332.5 keV line of ^{60}Co. The standard NaI(Tl) detector for comparison is 76 mm in diameter and 76 mm in height. This was the most common standard detector before HPGe detectors became available.

2.2.2. Peak summing effects

Peak summing occurs when two separate gamma rays induce charge carriers in the sensitive volume of a detector nearly simultaneously, resulting in the summing of their relative energy depositions. The maximum time window for these interactions is given by the drifting time of the charge carriers inside the electrical field, which are induced by the first gamma ray's interaction. For HPGe detectors this drifting time is in the range of a few micro seconds. As a result of this process, the two separate interactions can no longer be differentiated, and the characteristic energy information of both gamma rays is lost.

Obviously, peak summing effects have to be taken into account during spectrometric measurements to obtain correct FEP detection efficiencies and subsequently correct activity determinations. Due to different reasons for peak summing, two different cases can be distinguished, that will be discussed briefly here. A very detailed discussion, especially on so-called true coincidence summing, is given by G. Gilmore [Gil08].

If two or more nuclei decay simultaneously (i.e. $\Delta t < 1\,\mu s$), their emitted gamma rays may deposit their energy inside the germanium crystal and contribute to one combined output signal. The summing of peaks caused by this randomly coincident interactions is called **random coincidence summing (RCS)**. The occurrence of RCS is count rate dependent and therefore strongly affected by the activity contained in the sample and the geometry between sample and detector. However, both causes can be influenced by e.g. an increase of the distance between sample and detector or simply, if possible, waiting for the decay of the activity to decrease to manageable levels.

Most spectroscopy amplifiers used for gamma ray spectrometry feature a pile-up rejection (PUR) system, which strongly reduces RCS effects during a measurement. Whenever a second pulse is detected during the inspection interval of the first pulse, a gating signal is generated which is then used to reject the entire (summed) pulse from the measurement [Gil08]. This also decreases the effective live time of the measurement. Of course, this PUR is not completly effective and leaves some randomly summed peaks in the spectrum. RCS should therefore not be underestimated, especially in high count rate measurements. During low-level applications however, the activity usually does not reach critical levels, enabling fairly large solid angles covered by the detector without the risk of RCS.

If more than one gamma ray is emitted by the same nucleus during its de-excitation, these gamma rays may interact truly coincidently with the germanium crystal. Peak summing is then called **true coincidence summing (TCS)**. More than one gamma ray is emitted during decays where the de-excitation of the daughter nucleus does not transfer directly to the ground state. The half-life of these energy levels is usually on the pico second scale. Examples are ^{60}Co or ^{133}Ba.

Since this effect depends only on the sample-detector geometry, it is also relevant for low-level applications of gamma ray spectrometry. However, if the FEP detection efficiency is determined by MC simulations with detailed and accurate data on the decay schemes, the effect of TCS is included and corrected during analysis.

2.2.3. Radioactive decay corrections

If a (specific) activity is obtained for a sample, it needs to be related to a certain reference point in time. In general, the decay of any radionuclides under investigation between this references time and the measurement has to be corrected according to the decay equation

$$A\left(t\right) = A_0 \exp\left(-\frac{\ln 2}{T_{1/2}} \cdot t\right) \quad , \tag{2.2}$$

where A is the activity at time t and $T_{1/2}$ the half-life of the radionuclide. Additionally, only for cases of very long half-lives compared to the measurement time, the activity of the radionuclide is practically constant and the decay during the measurement can be neglected. For example for primordial radionuclides such as ^{40}K with a half-life of 1.250 Ga corrections are usually only marginal. But errors of a few percent might occur if for example a radionuclide such as ^{60}Co with a half-life of 5.27 a is measured for a 30 d time period and the activity is decreasing by more than 1 % during this measurement time.

During activation analysis (see Chapter 8) radionuclides with half-lives as short as a few minutes or only seconds are of interest. This quickly leads to a decrease in activity by considerable factors during relatively short time periods. Based on Equation (2.2) the decrease of count rate during the measurement must be corrected accordingly.

Figure 2.1 shows a radioactive decay in arbitrary units with the dashed black line. The measurement time Δt between t_1 and t_2 is of the same scale as the half-life of the nuclide's decay. Assuming a constant activity during the measurement gives an activity A_m, which is the mean activity during Δt. Using this activity in Equation (2.2) to obtain the activity at the reference time, which is $t = 0$ in the presented scenario, gives a wrong result. The (standard) case of using the start time $t = t_1$ in Equation (2.2)results in a lowered reference activity, which is shown in Figure 2.1. When decay correction is neglected by using the mid-point of the measurement time for the activity-calculation, an error of 2 % occurs at reference time, even if $\Delta t \approx T_{1/2}$. Proper correction is therefore usually advised [Gil08].

Although the assumption of a constant activity A_m during the measurement time is wrong, the number of decays measured does give the correct number of the nuclide's decays. This means that the areas beneath both the decay curve (black line) and the apparently constant activity (red line) in Figure 2.1 must be equal. Mathematically, this can be expressed with:

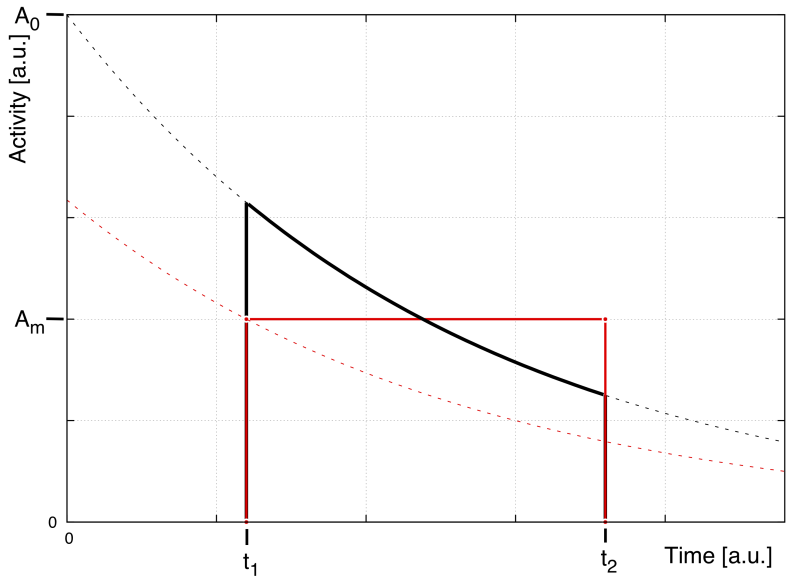

Figure 2.1.: Correction for the decay of a nuclide during measurement. The dashed black line represends the real decay of the activity, that is measured from t_1 to t_2. The red lines shows the activity A_m, based on the assumption on nearly constant activity during the measurement ($T_{1/2} \gg \Delta t$). This results in a wrongly calculated activity at reference time (here $t = 0$), indicated with the dashed red line.

$$A_m \left(t_2 - t_1\right) = \int_{t_1}^{t_2} A_0 \exp\left(-\frac{\ln 2}{T_{1/2}} \cdot t\right) \mathrm{d}t. \tag{2.3}$$

This leads to the correction term that is used in this work:

$$A_0 = A_m \cdot \frac{\Delta t}{T_{1/2}} \cdot \frac{\ln 2}{\exp\left(-\frac{t_1 \ln 2}{T_{1/2}}\right) - \exp\left(-\frac{t_2 \ln 2}{T_{1/2}}\right)} \quad , \tag{2.4}$$

where A_m is the measured activity, that is corrected, both for the decay before the measurement as well as during the measurement, to the real activity A_0. Similar correction formulas can be found in the literature, e.g. by R. Fitzgerald or E. Junod [Fit16, Jun74].

The correction term for the decay of a nuclide during measurement gets more complicated when dead time effects due to RCS and PUR (see Section 2.2.2) have to be taken into account. Due to the fact, that RCS is strongly effected by the activity of the radionuclide under investigation, which in this scenario is short-

lived and decaying during the measurement, the dead time is not constant but decreasing exponentially during the measurement as well. Correction terms for this case are provided by R. Fitzgerald [Fit16].

The measurements presented in Chapter 7 of this work are dealing with long-lived radionuclides where no correction for the decay during measurements is needed. In case of the analysis of rather short-lived nuclides presented in Chapter 8, the results are corrected for the decay of nuclides during the measurement. Additional dead time corrections are not necessary, since all measurements were performed with low enough overall activities that dead times were constant during measurements.

2.2.4. Analysis standards and decision limits

The analysis procedure used for gamma ray spectrometry measurements performed with the DLB is largely performed with software described in Section 4.7. The analysis tool `GeAna` was developed by T. Neddermann to incorporated the analysis standard of DIN ISO 11929:2011 for the analysis of gamma ray spectra [Ned14, DIN11]. During this Bayesian statistics based analysis the uncertainties of the measurement as well as the ones from weighting, sample treatment or efficiency calculations are considered. However, there is no automatic correction for the radioactive decay of the nuclide under investigation during measurement implemented.

The currently used standard DIN ISO 11929:2011 [DIN11] is the German version of the international standard ISO 11929:2010 'Determination of the detection limit and decision threshold for ionising radiation measurements' [ISO00]. Both standards are focussed on the measurement of radiation with high-resolution gamma spectrometry and consider the uncertainties of the measurement as well as the sample treatment and detection efficiency determinations. DIN ISO 11929:2011 is based on Bayesian statistics and is able to handle not only type A uncertainties (statistical uncertainties) but also type B uncertainties (based on other available information). It replaced the older german standard DIN 25482-5 [DIN97], which was based on conventional statistics. The Bayesian approach is, in contrast to conventional statistics, based on the non negativity of the measurand, i.e. the area of a peak in a spectrum [Ned14].

The type I error probability α gives the probability for a false positive decision, meaning that there is a wrong rejection of the null hypothesis. The type II error on the other hand, describes the probability β for a false negative decision

where the null hypothesis is false, but not rejected. Commonly used values are $\alpha = \beta = 0.05$, which give $k_{(1-\alpha)} = k_{(1-\beta)} = 1.645$. This corresponds to a probability of 5 % for a wrongful decision of sample contribution when there is only background, or 95 % of confidence that the measured sample contribution truly exists, respectively.

During gamma ray spectrometry performed with the DLB and the analysis tool `GeAna`, the net count rates and subsequent activities of radionuclides under investigation are calculated according to the guidelines from DIN ISO 11929:2011. The gross number of counts n_g inside a peak is obtained by calculating the sum over all bin contents in the region of interest (ROI) around the peak under investigation. The ROI stretches $\Delta\vartheta = \vartheta' - \vartheta$ around the channel ϑ that is associated with the peak's energy. Its width is recommended with 2.5 × FWHM [DIN11]. Since usually no exact knowledge of the different contributions to the peak area and its shape is available, a fit-based method would result in biased parameters due to a possibly inaccurate model [Ned14]. Instead, the number of net counts n_n in the peak can be determined by subtraction of the underlying continuum's counts z_0.

The spectral density of the continuum is described by a function $H(\vartheta; a_k)$. Usually the parametrisation for $H(\vartheta; a_k)$ is chosen linear ($H(\vartheta) = a_1 + a_2\vartheta$) or cubic ($H(\vartheta) = a_1 + a_2\vartheta + a_3\vartheta^2 + a_4\vartheta^3$) [DIN11]. 1.25 × FWHM from the centre of the ROI, the continuum ROIs are given with a width of 1.25 × FWHM each. Consequentially, the continuum counts z_0 below the peak are calculated by:

$$z_0 = \int_{\vartheta}^{\vartheta'} H(\vartheta; a_k)\,\mathrm{d}\vartheta. \tag{2.5}$$

The net count rate R_n is then determined from the gross counts $n_\mathrm{g,M}$, the continuum counts $z_\mathrm{0,M}$ and the run time t_M of the measurement (index M) by

$$R_\mathrm{n} = \frac{\left(n_\mathrm{g,M} - z_\mathrm{0,M}\right)}{t_\mathrm{M}} - \frac{\left(n_\mathrm{g,Bg} - z_\mathrm{0,Bg}\right)}{t_\mathrm{Bg}} \cdot \frac{f_\mathrm{M}}{f_\mathrm{Bg}}. \tag{2.6}$$

Additionally, the net count rates of any peaks in the detector's background spectrum (index Bg) are subtracted when peaked background correction (PBC) is applied. f_j is a correction factor for the normalisation of peak areas from different spectra to unity [Ned14]. Acquisition times for each spectrum are denoted with t_j.

In case of a peak that is not dominant in comparison to the continuum, the procedure is repeated with the width of the peak ROI reduced to 1.2 × FWHM,

although dominance is not explicitly defined in [DIN11]. However, the distance between the background regions and the peak centre is kept at least 2.5 × FWHM to not include parts of the peak in the background model [Ned14].

Eventually, the result for the specific activity A_{spec} of the sample can then be calculated from the net count rate of the peak by

$$A_{\mathrm{spec}} = \frac{R_{\mathrm{n}}}{f_{\mathrm{M}} M_S \varepsilon\left(E\right) p F_{dw}} \cdot 2^{\frac{t_{\mathrm{Start}} - t_{\mathrm{Ref}}}{T_{1/2}}} . \tag{2.7}$$

Here M_S denotes the sample mass, p the emission probability for the gamma line under investigation, $\varepsilon\left(E\right)$ the FEP detection efficiency obtained from MC simulation and F_{dw} the dry-to-wet-ratio, if the activity per dry mass is desired. Finally, the decay of the radionuclide between start t_{start} of the measurement and a reference time t_{Ref} is corrected with the radionuclides half-life $T_{1/2}$.

The uncertainties for the specific activity are calculated including all uncertainties of the different factors. Only the acquisition times are assumed with no uncertainty.

Strictly, the detector's background data has to be acquired under the exact same circumstances, such that self-shielding effects of the sample are considered as well, to perform PBC. This gains importance if large samples with high densities are measured, where the sample is actually increasing the shielding of the detector from the environment. However, this is practically impossible to perform for all samples and geometries during routine measurements. Consequently, a measurement of the residual detector background without a sample present is used, which results in a slight overcompensation for very radio-pure samples, that is usually negligible [Ned14].

In low-level gamma ray spectrometry, the radioactivity in samples is often so small that it can not be detected within reasonable measurement times. Due to the subsequent low count rates, the statistical significance of a peak has to be established [Gil08].

A quantity Y is given by the measured value y, for which the decision needs to be made, if a detection is valid or not [Cur68]. Therefore, the decision threshold (DT) (sometimes called critical limit [Gil08]) is applied, which is given by

$$y^* = k_{(1-\alpha)}\, \sigma_0 \quad , \tag{2.8}$$

where σ_0 denotes the standard deviation of the Gaussian distributed counts of the true value of Y. It is an a posteriori value and since it relies on the actually obtained count rate, it takes variations of the background during the measurement into account. If the measured net count rate exceeds the decision threshold the peak is 'detected', and the result is given with an interval of $(1-\alpha)$ confidence probability. Since, in practice, the standard deviation of the count distribution is unknown, the background counts B are used to estimate the variance of the net counts assuming zero measured counts. Equation (2.8) then becomes

$$y^* = 1.645\sqrt{2B} \tag{2.9}$$

for 5 % false positive decision probability [Gil08]. If the measured net counts do not exceed the DT, no contribution is observed, i.e. the measurement is compatible with the background count rate. Instead, an upper limit can be calculated to give the maximum reasonable counts for the measurement by

$$y^U = R_\mathrm{n} + k_{1-\gamma/2}\,\sigma_n \quad , \tag{2.10}$$

where R_n is the net count rate extracted from the measurement and σ_n its uncertainty [Gil08]. The coverage interval is given by $k_{1-\gamma/2}$, which is 1.96 for 95 % coverage probability.

A priori to the measurement, the detection limit (DL) $y^\sharp$ can be determined from a spectrum of the residual detector background by

$$y^\sharp = y^* + k_{(1-\beta)}\,\sigma_\mathrm{n}. \tag{2.11}$$

At the DL, the variance of the distribution is given by $\sigma_\mathrm{n}^2 = y^\sharp + 2B$, where B denotes the background counts. Rearranging the equation for a false negative decision probability of 5 % ($k_{(1-\beta)} = 1.645$) gives [Gil08]:

$$y^\sharp = 2.71 + 3.29\sqrt{2B}. \tag{2.12}$$

The DL gives the expectation of the minimal net counts that, with the given probability, are not an effect of the background. Therefore it can be used to check if the detection system is suitable for an intended measurement with the desired sensitivity. It can also be used to characterise the detector system and its detection capabilities under given circumstances.

The calculations above are usually given in absolute counts, but can be translated to count rates or activities as well. Any uncertainties, additional to

the statistical uncertainty of the net count rate, are then included according to DIN ISO 11929:2011. In general, all activities are given per sample mass (specific activities) with their standard uncertainty ($k = 1$). Additionally, the confidence interval (lower and upper limit) is given with 95 % coverage probability ($k_{(1-\gamma/2)} = 1.96$). The upper limit of the confidence interval is given in case the DT (5 % false positive probability, $k_{(1-\alpha)} = 1.645$) is not exceeded by the measurand.

A commonly used parameter for the characterisation of a low-level detector system is its minimum detectable activity (MDA), which is used to quantify the detection sensitivity of the system for a certain radionuclide (or its gamma ray energy respectively) under a given sample-detector geometry. It can be derived a priori from the measurement of the residual background system. A simplified proportionality can be used to estimate the sensitivity of a detector system [Gil08, Cur68]:

$$MDA \propto \frac{\sqrt{R_{\mathrm{Bg}}} \cdot \mathrm{FWHM}\,(E_\gamma)}{\epsilon\,(E_\gamma) \cdot \sqrt{t_{\mathrm{M}}}}. \tag{2.13}$$

It should be noted, that the MDA is in fact not the lowest activity detectable, which actually is given by the DT. However, the MDA can be used in a 'what if' context to evaluate a measurement method [Gil08].

In case of very low count rates, the Poisson distribution can not be estimated with a Gaussian distribution. Hurtgen et al. [HJW00] advise to replace the Poisson distribution with a binomial distribution for the estimation of counting uncertainties, when the background counts are < 100. With a coverage factor of $k = 2$, the confidence level becomes 95.45 %, which corresponds to a coverage factor $k = 1.69$ for a one-tailed probability [HJW00]. Compared to Equation (2.12), the DL becomes then:

$$y^{\sharp}_{\mathrm{low}} = 2.86 + 4.78\sqrt{B + 1.36}. \tag{2.14}$$

During the analysis performed in this work this special case is not applied since background counts all exceed 100 counts. This is usually the case for gamma spectrometry measurements [Gil08].

3. Sources of Background Signals

A key value for the characterisation of any low-level detector system and its operation is its sensitivity. Mathematically (compare Equation (2.13)), it can be increased, i.e. the MDA can be lowered, in several ways. In the majority of cases, the measurement time is limited from the beginning. If not, its square root term makes the increase in measurement time eventually pointless. An increase of the detection efficiency would be a very effective way, but it is hardly possible (compare Section 2.2.1). The geometric factors are often set by the sample's geometry and can not be optimised. The intrinsic efficiency of a detector system, e.g. a HPGe detector, is fixed once the detector system is completely installed and commissioned, which is also the case for its energy resolution.

This leaves the reduction of the characteristic background as the only possible way to increase the sensitivity of a given detector system. In order to reduce any residual background, or even avoid background during the set up of the system, one has to know the sources and origins of the different background contributions. In the following chapter, the main sources of background in (low-level) gamma ray spectrometry measurements performed with HPGe germanium detector systems are discussed with a focus on photon radiation. A very detailed review with more information on the topic of background sources and low-background shielding techniques are given by G. Heusser [Heu95].

3.1. Background from the detector environment

Sources for background contributions can be categorised into two main groups. One is given by the radioactivity from the environment of the detector system that contributes to the residual background spectrum of the detector. The second is given by detector signals that are induced directly or indirectly by cosmic rays, among them mostly cosmic muons. The latter will be discussed in more detail in Section 3.2.

Radioactivity from the environment, i.e. from impurities in the detector assembly material or the surroundings, can further be sub-categorised into:

- Primordial nuclides and decay chains: Mainly ^{232}Th, ^{238}U, ^{235}U and ^{40}K.
- Airborne radioactivity, mostly as part of the decay chains: ^{222}Rn and ^{220}Rn.
- Anthropogenic radioactivity that was introduced to the earth's atmosphere during nuclear weapon tests and accidents: ^{137}Cs and ^{60}Co.

3.1.1. Environmental radioactivity

Naturally occurring radionuclides in the environment that are present since the stellar nucleosynthesis of our solar system are called primordial radionuclides. Their half-lives are of the order of magnitude of the Earth's age ($\sim 10^9$ years) and they can be found commonly in the crust of the earth, with average values for uranium, thorium and potassium given in Table 3.2. Some of these primordials are the starting nuclides of decay chains, which contain a series of daughter nuclides with half-lives from the microsecond scale to thousands of years. Due to their relatively high average abundance in the environment, primordials can be found in many minerals and materials. Metals for example can be subject to contamination if no chemical purification process is done, due to the presence of primordials in the mined ores. Due to their general presence in building materials, primordial radionuclides are contributing to the residual background of all detector systems and can be found in every detector's background spectrum.

^{238}U and ^{235}U are the starting nuclides for two of the three most abundant decay chains, which all end in different stable isotopes of lead. Since natural uranium contains only 0.72 % of ^{235}U but 99.27 % of ^{238}U, the latter is dominating the background contribution of uranium [MBCB$^+$16]. Additionally, uranium contains less then 0.01 % of ^{234}U, which is often neglected in the composition of natural uranium and only discussed as daughter-nuclide in the ^{238}U decay chain.

The third nuclide of the major decay chains is ^{232}Th, which is contained with 99.999 % in natural thorium. One of the prominent members of the ^{232}Th decay chain is ^{208}Tl. Its gamma ray energy of 2614.5 keV is referred to as highest gamma ray energy occurring in nature, when using the restriction of 'significant emission probability' ($p_\gamma = 99.75\,\%$), which is often not explicitly stated. However, since higher energetic gamma rays are only emitted with much less intensity, e.g. dur-

Table 3.1.: Specific activities of uranium, thorium and potassium radioisotopes [NNDCN18, Lab18].

Isotope	Rel. nat. abundance [%]	Half-life [1×10^9 a]	Atomic weight [u]	Specific activity [MBq/kg]
^{238}U	99.27	4.468	238.03	12.44
^{235}U	0.72	0.704	238.03	78.94
^{232}Th	100	14.02	232.04	4.076
^{40}K	0.012	1.250	39.098	270.5

ing the de-excitation of ^{214}Bi with less then 0.05 %, the 2614.5 keV line is used as high energetic reference point in many works including this work.

At some point of their chain all three major decay series include an isotope of the noble gas radon (see Section 3.1.2). If radon gas diffuses out of the material that contains the mother nuclide, it can lead to the disturbance of the secular equilibrium of the decay chain. Secular equilibrium is the state in which the decay rate of a nuclide is equal to its production rate, which is possible for decays where the mother nuclide is much longer-lived than the daughter nuclide. Any disequilibrium is especially important to consider if the activity of the complete decay chain is to be determined, e.g. with gamma ray spectrometry. The situation is then challenging, because several daughter nuclides are not directly emitting gamma rays at all or only with very low emission probabilities.

Table 3.1 lists the most commonly found primordial radionuclides and some of their characteristic properties together with their specific activities.

Potassium, that is occurring naturally, contains three isotopes, of which only ^{40}K is radioactive with a relative abundance of about 0.012 %. However, potassium is $5 - 10 \times 10^3$ times more abundant in the Earth's crust than uranium and thorium (compare Table 3.2). ^{40}K is also the most common radionuclide in the human body. Because of the chemical characteristics of potassium, ^{40}K is stated to be the most difficult contamination for low-background applications to be removed from a material [Pov17].

Another example for a primordial radionuclide is ^{113}Cd, which decays via beta minus decay into the ground sate of ^{113}In with a half-life of about 8×10^{15} a [DRW$^+$09]. The natural abundance of 12.22 % in cadmium makes the signal the strongest source of background for the ultra low-background spectrum of the COBRA demonstrator experiment. Both properties cause a constant decay rate,

Table 3.2.: Average abundances of uranium (U), thorium (Th) and potassium (K) in the earth's crust [Hay15]. The unit ppm refers to 1×10^{-6} g of element per gram of sample. Average activities due to the radioisotopes ^{238}U,^{235}U,^{232}Th and ^{40}K are calculated with values from Table 3.1.

Element	Avg. nat. abundance [ppm]	Avg. Activity in Earth's crust [Bq/kg]	
Uranium	2.7	33.58	(^{238}U)
		1.534	(^{235}U)
Thorium	9.6	39.13	(^{232}Th)
Potassium	20 900	678.8	(^{40}K)

that can be used to investigate the stability of the CdZnTe detectors by monitoring the decay rate of ^{113}Cd over time [EGG$^+$16]. Recently, COBRA used a precise measurement of the spectral shape of this fourfold forbidden non-unique beta decay for an estimation of the effective value of the weak axial-vector coupling strength g_A [BD$^+$18].

^{190}Pt and ^{144}Nd are long lived alpha emitters with half-lives on the scale of 10^{11} a to 10^{15} a. Scintillation detectors made of $LaBr_3$ are not used for low-level applications, due the primordial ^{138}La with a half-life of 1.04×10^{11} a. Although its abundance is only about 0.1 %, both decays (electron capture and beta minus decay) are accompanied by high energetic gamma rays preventing a low background [Ned14, MBCB$^+$16, NNDCN18].

Nuclides that are subject to double beta decays, and therefore investigated for neutrinoless double beta decays by the experiments mentioned in Chapter 1 are also primordials, e.g. ^{116}Cd, ^{130}Te, ^{76}Ge or ^{136}Xe.

Table 3.2 gives the natural abundance in the Earth's crust for the elements uranium, thorium and potassium. Isotopes of these three elements are the major sources for background contributions due to environmental radioactivity. The average abundance is therefore converted into the average specific activity of the given isotope in the Earth's crust.

It should be noted that the given average concentrations may vary considerablly for different locations or types of bedrock. In general, the highest specific activities can be found in granites [Heu95].

Building materials surrounding the detector system, e.g. concrete walls or rock

overburdens, can contain rather high concentration of primordial radionuclides. Due to the strong Z-dependence of the absorption coefficient for gamma rays, they can sufficiently be absorbed by high-Z material used as shielding. 15 cm of lead ($Z = 82$) for example decrease the intensity of 3 MeV gamma rays by more than three orders of magnitude [BHS+10]. It should however be noted that more lead can increase the background contribution from tertiary neutrons induced by cosmic ray muons via muon capture or by photonuclear reactions [Gil08, PBJV08]. These background contributions are discussed in Section 3.2.2.

Another possibility for primordials to contribute to the background of a detector system is due to contaminations of construction parts of the system itself. While the major component, the germanium crystal, is of extremely high purity, other components can suffer from radioactive impurities. If low-background conditions are desired, these need to be addressed, especially if they are located close the the crystal. HPGe crystals themselves have impurity concentrations of less then 10^{-12}, that make HPGe one of the most purest materials [Gil08].
Due to its low atomic number of $Z = 13$, aluminium is widely used for end-caps and crystal holders. Because aluminium is usually contaminated with thorium and uranium levels around 1 Bq/kg, specially produced ultra-clean material is used for low-level applications [PBJV08]. However, this low-background material can still have a negative impact on the residual background of a detector system (compare Section 7.1).
Unusually high concentration of radionuclides, even in single tiny surface-mount devices or printed circuit boards of electronic components, can make the removal from a detector system necessary to reach the desired background levels [Lau17]. In other cases, additional radiopure shielding material is introduced to the detector setup to shield against impurities, e.g. from field effect transistors [LBP+15] or capacitor units [HMS+18].

Finally, background contributions can originate from the materials that are intended to shield the detector against background contributions from the environment. Lead for example, is primarily used as shielding material due to its high atomic number of $Z = 82$, its high density of 11.342 g/cm^3 and other advantageous properties [PBJV08]. However, it has the disadvantage of being almost always contaminated with ^{210}Pb. As part of the ^{238}U decay chain this lead isotope decays with a half-life of 22.2 a via beta minus decay to ^{210}Bi with the subsequent emission of 46.54 keV gamma rays. The following decays of ^{210}Bi (beta minus) and ^{210}Po (alpha) are relatively short-lived and not accompanied

by high-intensity gamma rays. End-point of the chain is the stable lead isotope ^{208}Pb [Lab18]. While specific activities around 100 Bq/kg are common for ^{210}Pb in standard lead, there is low-activity lead commercially available with lead levels around and below 1 Bq/kg. A very limited supply of ultra-pure lead is available in the form of 2000 year old lead bricks from sunken ships in the Mediterranean Sea (so-called 'roman lead').

In order to construct (ultra-) low-level gamma ray spectrometry systems it is inevitable to perform radiopurity screenings for almost all construction parts in order to select the purest materials [Lau17]. If possible, the production and storage of these materials needs to take place underground to avoid cosmogenic activation as far as possible [LHG+04]. Some materials, like very radiopure copper, can actually produced underground in direct proximity of the experiments [BBI+17].

3.1.2. Airborne radioactivity

Radioactive isotopes of the noble gas radon are components of all three major decay chains of uranium and thorium. Due to its gaseous state, it has the ability to diffuse and escape from the matrix containing the mother nuclide and thereby break the equilibrium of the decay chain. This is particularly the case for the longest-lived isotope of radon, ^{222}Rn, which therefore has the highest average concentration in air.

^{222}Rn, originating from the ^{238}U decay chain, is the strongest source of airborne radioactivity due to its comparatively long half-life of 3.8 d [Heu95]. It is therefore crucial in terms of background contribution in low-background applications. The most prominent gamma ray emitting daughter nuclides are ^{214}Pb (351.9 keV, 295.2 keV), ^{214}Bi (609.3 keV, 1764.5 keV, 1120.3 keV) and ^{210}Pb (46.5 keV). Only ^{210}Pb has a half-life exceeding the scale of minutes to days with about 22.2 a [Lab18].

The isotope ^{220}Rn is part of the ^{232}Th decay chain and has a half-life of 55.8 s. Its sub-chain decays via ^{212}Pb (238.6 keV) with a half-life of 10.6 h and ^{208}Tl (583.2 keV and 2614.5 keV) with a half-life of 3.1 min [Lab18]. Usually, the concentration of ^{220}Rn is less than 1 % of the ^{222}Rn concentration [Heu95].

Because the ^{235}U decay chain is usually less present in the environment, the radon isotope ^{219}Rn is mostly negligible for low-level spectrometers. Additionally, the half-life of ^{219}Rn is only about 3.9 s and the gamma rays in this sub-chain only have limited intensities [Lab18].

Mean values for radon concentrations in air are reported with 5 Bq/m^3 to

10 Bq/m^3 in free air and 50 Bq/m^3 to 100 Bq/m^3 inside of buildings [The96]. For Germany, the Bundesamt fuer Strahlenschutz (BFS) reports a value of 50 Bq/m^3 for the average radon concentration indoors, with individual measurements up to 1000 Bq/m^3 [Bun18].

To reduce radon levels inside the sample chamber as well as prevent any sample contamination, gaseous nitrogen that is boiling of from the detector-cooling dewar is usually used to flush the sample chamber. An air-tight sealing around the entire shielding and slight overpressure avoids the diffusion of radon through the detector shielding. Alternative methods are the filtration of incoming air or active radon-reduction techniques to reduce radon contents in the air of gamma ray spectrometry laboratories, which is used for example at the Laboratorio Subterrneo de Canfranc (LSC) in Canfranc, Spain [Ian16]. Special care must be taken if primordial decay chains are under investigation inside a sample. Due to the possibility of a disequilibrium, it is recommended to store samples in sealed containers, possibly under controlled and preferably radon-free conditions, for sufficient time to reestablish equilibrium [Lau17].

3.1.3. Anthropogenic radioactivity

Man-made radioactivity was introduced into the earth's atmosphere mainly through fission products during nuclear weapons tests in the late 1950s [The96]. Additional large amounts of activity were brought into the environment due to reactor disasters as they occurred in Chernobyl, Ukraine in 1986 and in Fukushima, Japan in 2011. Small amounts of radionuclides are released also during normal operation of other nuclear installations.

A commonly found isotope in the today's environment, due to these tests and incidents, is ^{137}Cs. Its half-life of 30.1 a leads to considerable long-term contaminations in areas hit by the fall-outs [Lab18]. The decline of the activity over the last decades on the other hand is a major motivation for the development of new ultra-sensitive radio-analytical techniques [Pov18].

Other nuclides such as ^{207}Bi, ^{108m}Ag or ^{60}Co and several more radionuclides were released into the environment by humans as well [Lau17].

Iron and steel products are commonly subject to contamination with ^{60}Co, which is induced during the industrial production process. Previously, cobalt was used in blast furnaces to monitor their wearing down and can be found until today due to the heavy recycling of iron [The96]. Additional contamination

was introduced to the recycling process of iron by the improper disposal of high-activity sources of ^{60}Co [K^{+}04].

In terms of radioimpurities in shielding material and construction parts, ^{137}Cs only plays a minor role. The contamination of iron products with ^{60}Co however, has to be considered during installation of low-level applications. One possibility is the use of old iron, preferably from before 1940, where ^{60}Co was not induced in the first place or the half-life of 5.27 a has lead to vanishing activity levels today. But very limited availability of these materials often makes screening for radioimpurities of construction materials inevitable. Within existing low-level experiments, ^{60}Co might still be present, regardless of the careful material selection, due to cosmogenic activation processes. The topic of cosmogenics is discussed separately in Section 3.2.4.

3.2. Background from cosmic radiation

Cosmic rays, and thereof mainly cosmic muons, are a major background component for all low-level applications and experiments in general and for gamma ray spectroscopy systems in particular. Their background contribution is induced either by direct interactions with the detector or indirectly via production of cosmogenic radionuclides inside detector components and shielding material. Even if the experiment is located deep underground, where it is relatively protected against cosmic radiation, cosmogenics might still contribute to the residual background as a remnant of the production period above ground. Experiments with only shallow overburdens, such as the DLB, need to address cosmic radiation with special care in order to reach the desired sensitivities and low-background levels. Adapted shielding concepts as well as active background reduction techniques are usually employed for this purpose, if the detector system is not installed several hundred meters below the surface. Even existing detector systems might benefit considerably from improvements of active reduction systems, which will be shown in Section 4.4. Due to the importance of this component for background, the origin of cosmic rays as well as their different ways of contribution to the background spectrum will be discussed in more detail in the following sections. A very extensive review of cosmic rays on Earth is given by P. Grieder [Gri01].

3.2.1. Cosmic radiation and cosmic muons

Cosmic radiation was first discovered by V. Hess in 1912 , when he undertook balloon flights and measured a component of the total radiation that increased with the balloon's height above ground, independently of the time of day or night [Lib65]. In 1936, Hess was awarded the Nobel Prize in Physics 'for his discovery of cosmic radiation' [Nobb]. Since then, a vast field of research has developed around cosmic rays spanning various directions from particle physics and astrophysics to geophysics and biological and medical physics [Gri01].

Primary cosmic rays

The primary cosmic radiation, which is composed of about 98 % hadrons and 2 % electrons, has various sources. Our Sun is only directly contributing to the low-energetic part of cosmic rays with particle energies below 50 MeV. The particle fluxes, however, are comparatively high for this so-called solar cosmic radiation. The galactic component of cosmic rays, from outside of our solar system, is consisting of particles with higher energies but lower mean fluxes. Particles of the highest energies are probably of extragalactic origin, but their sources and exact acceleration mechanisms are still a matter of scientific debate [Gri01]. Amongst others, supernova explosions and active galactic nuclei (AGN) are possible sources. Recently, the blazar TXS 0506+056 has been identified as a promising candidate for the acceleration of very high-energetic cosmic rays [AAA$^+$18c, AAA$^+$18b].

Both the energy and the flux of cosmic rays are subject to both periodic and aperiodic temporal variations Here, only two examples will be given to illustrate these variations. The sun is not only contributing directly to the particle flux, mainly with protons and electrons, but also modulating it with its magnetic field. A modulation effect of about 10 % can be observed due to the solar cycle of eleven years [Nie08, Gri01]. Another influencing factor is the density of earth's atmosphere. The effect of atmospheric temperature for example has been measured on the basis of high-energetic cosmic muons at the LNGS underground site, yielding about (1.29 ± 0.07) % relative amplitude and a phase of (179 ± 6) d [B$^+$12a].

Secondary cosmic rays in the atmosphere and at sea level

When entering the Earth's atmosphere, incident hadrons from the primary cosmic radiation interact with molecules of the air and atmospheric nuclei, such

as nitrogen and oxygen, and produce cascading showers of secondary particles. This secondary cosmic radiation can be divided into three major components: A hadronic component, an electromagnetic component and a muonic component. The composition of these components changes with atmospheric depth due to interactions, life times and decays of the different particles.

At sea level, the atmospheric depth is about $1030\,\mathrm{g/cm^2}$, which corresponds to 10.3 m.w.e.. Historically, the remaining cosmic radiation at sea level is divided into two components: a soft component that contains electrons, positrons and photons and a hard component that consists of protons, neutrons and muons. Since neutrinos are not considered here, cosmic muons are the most numerous particles at sea level. The flux values of the different particles are often universally reported with: 190 muons/$(\mathrm{m^2\,s})$, 64 neutrons/$(\mathrm{m^2\,s})$, 46 electrons/$(\mathrm{m^2\,s})$, 1.4 protons/$(\mathrm{m^2\,s})$ and 0.13 pions/$(\mathrm{m^2\,s})$ [PBJV08, The96, Heu95].

By definition, the soft component is stopped after 15 cm of lead, which corresponds to an areal density of $170.1\,\mathrm{g/cm^2}$ (with a density of lead of $11.342\,\mathrm{g/cm^3}$) or 1.7 m.w.e., which is achieved relatively easy with about three standard building floors. The hard component on the other hand can further be divided into a nucleonic component consisting of protons and neutrons and a muonic component. Secondary nucleons are attenuated exponentially with a mass attenuation coefficient of about 1.6 m.w.e. and therefore often negligible after a few meters of water equivalent [The96]. Although the DLB's overburden of 10 m.w.e. is reducing the flux considerably, secondary neutrons will be discussed further in Section 3.2.3. Cosmic muons are not only the most numerous particles at sea level, their high penetration power makes them also very important in terms of background contribution for low-level applications. Below, many different parameters describing the spectrum, intensity and attenuation of cosmic muons are discussed.

Muons are Leptons with a mass of 105.66 MeV and a mean lifetime of about 2.2 µs. Their flux at sea level arises mainly from the decay of charged pions of the secondary cosmic radiation high in the atmosphere, typically at heights of 15 km [Gri01]. They lose about 2 GeV of their initial energy to ionisation processes in the atmosphere until they reach the surface with a mean energy of 4 GeV. At this point, their energy spectrum and angular distribution are given by a convolution

of their production spectrum, energy loss and decay [Tan18]. Their charge ratio (μ^+/μ^-) is caused by an excess of positive pions and kaons which leads to an overall excess of positive muons and depends weakly on the muon momentum [Gri01, Tan18]. A mean ratio of about 1.28 has been measured in the energy range of 5 GeV to 1000 GeV[K$^+$10], which is very close to the commonly used approximated of $\mu^+/\mu^- = 1.3$ [B$^+$06, Rey06, Tan18].

Properties of cosmic muons

The intensity I_μ of cosmic muons can be described with several different units. $I_\mu\left(\theta, \phi, p_\mu\right)$ is used to describe the directional intensity per unit solid angle $\mathrm{d}\Omega$, per unit horizontal area $\mathrm{d}A$ and per unit time $\mathrm{d}t$ and is given in units of $1/(\mathrm{m}^2\,\mathrm{s}\,\mathrm{sr})$. The solid angle is given by the zenith angle θ and by the azimuth angle ϕ. While the intensity is generally treated as uniformly distributed in ϕ, the relation between the directional intensity $I_\mu\left(\theta, \phi, p_\mu\right)$ and the vertical intensity $I_{\mu,0}\left(\theta = 0\right)$ is given by

$$I_\mu\left(\theta, \phi, p_\mu\right) = I_{\mu,0}\left(\phi, p_\mu\right) \cdot \cos^n \theta. \tag{3.1}$$

The $\cos^n$ distribution in θ considers the higher atmospheric depth that has to be penetrated by cosmic muons at larger zenith angles. Although the coefficient n depends weakly on the muon momenta, it is usually approximated with a constant value. Different values have been reported in the literature, between $n = 1.85$ [Gri01] and $n = 2.2$ [PDM$^+$17]. However, this work uses the most common approximation of $n = 2$, which has proven to be valid for most applications, especially for muon momenta of around 3 GeV [Tan18]. For higher muon energies the zenith angle dependence is better described proportional to $\sec\theta$, which is used for deep underground experiments where only high energetic muons arrive.

The flux of cosmic muons J_1 is often reported as crossing a horizontal area, e.g. a detector system, from above, and can be calculated by the integration of $I_\mu\left(\theta, \phi, p_\mu\right)$ over the upper hemisphere of the solid angle:

$$J_1 = \int I_\mu\left(\theta, \phi, p_\mu\right) \cos\left(\theta\right) d\Omega. \tag{3.2}$$

J_1 is reported in units of $1/(\mathrm{m}^2\,\mathrm{s})$ and will be referred to as flux of cosmic muons at sea level and ground respectively throughout this work. Alternatively the flux is sometimes reported as omnidirectional flux J_2, that is calculated

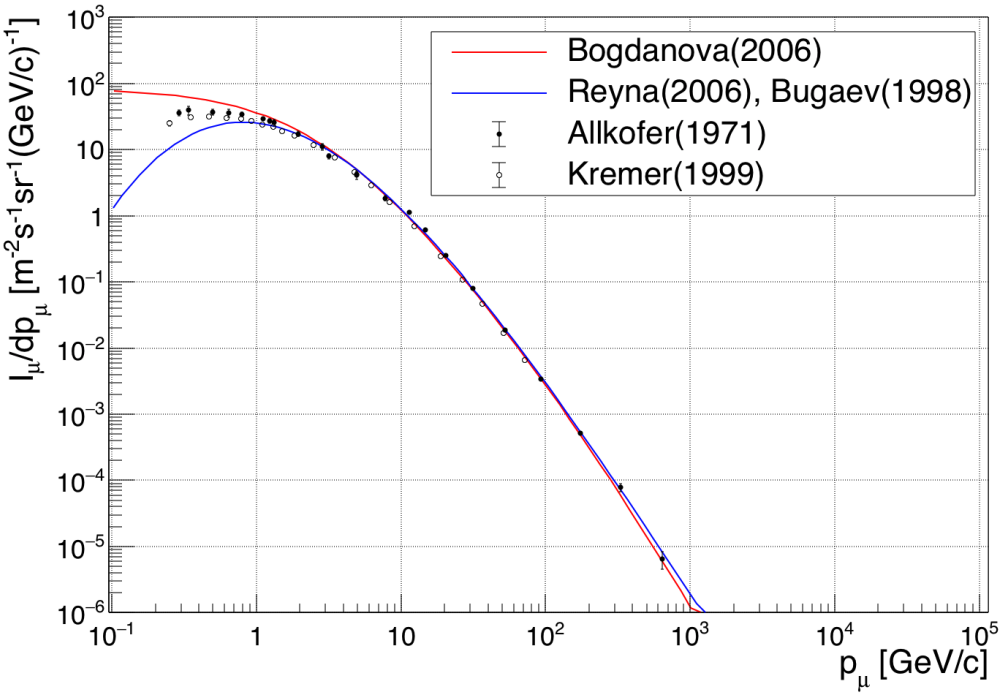

Figure 3.1.: The vertical differential momentum spectrum of cosmic muons at sea level. Solid lines according to the Bogdanova model [B$^+$06] (red), and Reyna/Bugaev model (blue) [Rey06, BMN$^+$98]. Data points are from Allkofer et al.[ACD71] and Kremer et al. [K$^+$99] respectively.

by the integration of I_μ over the upper hemisphere of dΩ. The flux of 190 muons/(m^2 s), that is mentioned above, is expressed as omnidirectional flux and can be converted to the horizontal flux via $J_1 = \frac{3}{4} \cdot J_2 \Rightarrow \frac{3}{4} \cdot 190$ muons/(m^2 s) = 142.5 muons/(m^2 s).

Especially for MC simulations including the particle flux of cosmic muons for a given detector system, the differential momentum spectrum $j_\mu\left(\theta, \phi, p_\mu\right)$ is of interest. The integration of the vertical differential momentum spectrum results in the vertical flux J_1.

The vertical differential momentum spectrum of cosmic muons at sea level is shown in Figure 3.1. Plotted are two different parameterisations that will be discussed briefly in the following: The first from L. N. Bogdanova et al. [B$^+$06] (red line) and second one from E.V. Bugaev et al. [BMN$^+$98] with a parameter set proposed by D. Reyna [Rey06] (blue line). Other models, that were proposed in the past, for example from A. Tang et al. [THSKT06], are not used since Reyna showed that the data is generally less well described by them [Rey06].

Bogdanova uses an analytical formula, similar to a proposal by S. Miyake [Miy73], for the calculation of the cosmic muon flux at shallow depths underground. The formula's empirical parameters are optimised to describe the totality of the experimental spectrum for the vertical muon intensity [B$^+$06]. Bogdanovas approximation of the muon energy distribution at sea level is given by:

$$j_{\mathrm{B}}\left(p_\mu, \theta\right) = \frac{18}{p_\mu \cos\theta + 145} \left(p_\mu + 2.7 \sec\theta\right)^{-2.7} \frac{p_\mu + 5}{p + 5 \sec\theta} \quad , \tag{3.3}$$

where θ denotes the zenith angle and p_μ is the muon momentum in GeV/c between 1 and 1×10^5 GeV/c. The three terms can be interpreted as muon production and the decay effects of pions and muons respectively. In combination with energy dependent range tables (e.g. in [GMS01]) the vertical muon intensity can be calculated.

Reyna provides another parameterisation [Rey06], which is based on a five parameter model for the vertical cosmic muon intensity by Bugaev [BMN$^+$98]. The model is based on the propagation of high energetic nucleons as well as pions and kaons in the atmosphere. Bugaev provided several parameter sets for different muon momentum intervals. Reyna on the other hand, uses a scaling factor to relate the Bugaev parameterisation for the vertical intensity to that at any solid angle and included data for all zenith angles and muon momenta for his new fit of the coefficients [Rey06]. The result is the following, improved approximation:

$$j_{\mathrm{R}}\left(p_\mu\right) = 0.0025\, p_\mu^{-1\left(0.246 + 1.288 \log_{10}\left(p_\mu\right) - 0.256 \log_{10}^2\left(p_\mu\right) + 0.021 \log_{10}^3\left(p_\mu\right)\right)}. \tag{3.4}$$

This model describes the muon intensity for all zenith angles and can be considered valid for muon momenta between 1 and 2000 GeV/cos θ. Reyna recommends the use of this modified model for simulations at depths of less than 100 m.w.e. [Rey06].

Figure 3.1 shows both models from Bogdanova ($j_{\mathrm{B}}\left(p_\mu, \theta\right)$, red line) and Reyna/Bugaev ($j_{\mathrm{R}}\left(p_\mu, \theta\right)$, blue line). Additionally, experimental data from Allkofer et al. [ACD71] and Kremer et al. [K$^+$99] is included in the graph. Both approximations cover most of the cosmic muon spectrum in a similar way, especially between 2 and 100 GeV. For muon momenta above 100 GeV, both models start to drift apart slightly, although both claim to be valid for energies

up to about 10 TeV [B$^+$06, Rey06]. The particle fluxes at these energies and above, however, is several orders of magnitude smaller. For the modelling of the background contribution in shallow underground laboratories these high energetic muons are negligible. The necessary energy for a cosmic muon to reach a depth of 100 m.w.e. is about 22.2 GeV (compare Equation (3.7)). Calculation of the integral intensity for muon momenta of p_μ >22 GeV results in portions of less than 2.9 %. For p_μ >200 GeV, the integral intensity gets even below 0.03 %. In the low energy region however, deviations are more notable, due to their large contributions to the integral intensity. While the models are specified to be valid down to 1 GeV and 2 GeV respectively, neither describes the experimental data very well below these energies. In case of the DLB, both models might still be valid since the overburden of 10 m.w.e. can only be penetrated by cosmic muons with energies above 1.5 GeV. Reyna reports that, if compared with experimental data, his parameterisation describes the data with the smallest reduced χ^2 [Rey06]. When used to calculate the overall vertical intensity of cosmic muons at sea level J_1, the Bogdanova model gives a flux of 207 muons/(m^2 s) whereas the Reyna/Bugaev approximation results in a flux of 138.2 muons/(m^2 s). Compared with the familiar flux values mentioned in this section and measurements reported in Chapter 6 the Reyna/Bugaev model gives better results and will therefore be used primarily throughout this work.

If values for the flux of cosmic muons from the literature are compared, it is important to pay close attention to the conditions under which they apply. Often the directional intensity I_μ or the total flux crossing a horizontal area J_1 are used, but sometimes the omnidirectional flux J_2 is given instead. The Particle Data Group [Tan18] for example, reports the directional intensity of cosmic muons with about 70 muons/(m^2 s sr), which corresponds to a vertical flux of 110 muons/(m^2 s) for muons with momenta above 1 GeV. In the same document however, the value given for the vertical flux is ≈1 muon/(cm^2 min) which can be transferred to a vertical flux of 167 muons/(m^2 s)[Tan18]: A difference of about 50 %. Additionally, the Particle Physics Booklet of the Particle Data Group gives a flux of 130 muons/(m^2 s) for cosmic muons vertically crossing a unit area [B$^+$12b].

In general, it is recommended to provide the energy interval of cosmic muons that is used to describe the integral flux. For actual measurements it usually is given by a lower energy cutoff, that is confined by the detector system used. Additional parameters that should be specified cocerning the (geomagnetic) location, especially the latitude as well as the altitude at which the measurement

was performed.

Due to the geomagnetic field, the cosmic muon energy spectrum shows a latitude dependence for energies below 15 GeV. These energies strongly influence the integral intensity. Another effect that may be neglected for most applications is the asymmetry between the geomagnetic dipole and the Earth's rotation axis that causes a longitude effect [Gri01].

An extensive list of measurements, which include their locations geomagnetic latitude, is given in [Gri01]. The measurements have been performed at or near to sea level and have their energy interval listed as well. Allkofer reported values at sea level between 113.9 muons/$(\mathrm{m}^2\,\mathrm{s})$ near the geomagnetic equator and 156.1 muons/$(\mathrm{m}^2\,\mathrm{s})$ in Kiel, Germany [ACD71, AAD68]. More recent measurements are listed in [PDM+17] with values ranging from 97.66(8) muons/$(\mathrm{m}^2\,\mathrm{s})$ to 143.4(19) muons/$(\mathrm{m}^2\,\mathrm{s})$ for different locations around the globe. The measurement with the closest geomagnetic latitude to the location of the DLB is provided by Wentz with 134.1 muons/$(\mathrm{m}^2\,\mathrm{s})$ for muon momenta of $p > 0.6\,\mathrm{GeV}$, measured in Karlsruhe, Germany (about 300 km south of the DLB's location) [Gri01].

Finally, the particle flux of cosmic muons needs to be corrected for the altitude of the location of measurement. At 4300 m above sea level, for example, the flux of cosmic muons is more than twice as high as at sea level [B+12b]. However, corrections might be beneficial at lower altitudes as well [HMH16]. For the DLB, which is located at an altitude of about 118 m above sea level, this results in a relative increase of the cosmic muon flux by about 6 %, according to data recorded by R. Bellotti et al. [BCC+99].

According to the Bethe-Bloch formula, cosmic muons with a mean energy of 4 GeV are minimal ionising particles with a mean stopping power of about $2\,\mathrm{MeV}/(\mathrm{g\,cm}^2)$ [Pau71]. In matter their energy loss is mainly caused by direct ionisation and by radiative processes such as bremsstrahlung, direct electron-positron pair production and photo-nuclear interactions [Gri01, GMS01]. The mean stopping power of cosmic muons can therefore be described as a function of the distance X in matter traversed by

$$-\frac{dE_\mu}{dX} = a\left(E_\mu\right) + b\left(E_\mu\right) \cdot E_\mu \quad , \tag{3.5}$$

where E_μ is the total energy of the muon (or another heavy charged particle) [BBC+52]. The parameter $a\left(E_\mu\right)$ represents the electronic stopping power and

$b\left(E_\mu\right)$ the fractional energy losses by radiation processes. Although both parameters are actually slowly varying functions of the muon energy [GMS01], they are approximated with constant values for the integration over the energy to obtain the energy-range-relation [Gri01]:

$$E_\mu(X) = \left(E_\mu^{\text{sea}} \cdot \frac{a}{b}\right) \exp\left(bX\right) - \frac{a}{b}. \tag{3.6}$$

Equation (3.6) describes the energy of a cosmic muon E_μ at a given depth X, when started with an initial energy at sea level of E_μ^{sea}. This equation can be used to determine the minimal energy E_μ^{min} that is necessary for a cosmic muon to reach the depth of X:

$$E_\mu^{min}\left(X\right) = \frac{a}{b}\left(\exp\left(bX\right) - 1\right). \tag{3.7}$$

a and b are chosen according to the penetrated medium and the mean muon energy at sea level of 4 GeV: a =2.336 $\times 10^{-3}$ GeV cm^2/g and b =1.1 $\times 10^{-6}$ cm^2/g. Tabulated values for several elements and compounds as well as polymers and biological materials can be found e.g. in [GMS01]. The inversion of Equation (3.7) results in the mean range X_R of a cosmic muon with given energy E_μ:

$$X_R\left(E_\mu\right) = \frac{1}{b}\left[\ln\left(E_\mu \frac{b}{a}\right) + 1\right]. \tag{3.8}$$

Equation (3.7) can now be used to calculated the integral intensity $J_{1,\mu}\left(\theta, \phi, E_\mu, X\right)$ of cosmic muons at the depth X according to

$$J_1 = \int_{E_\mu^{min}}^{E'_\mu} j\left(E_\mu, \theta\right) \mathrm{d}E. \tag{3.9}$$

The vertical differential momentum spectrum of cosmic muons at sea level is discussed above and shown for two different parameterisations in Figure 3.1. Equation (3.9) is used to obtain depth-dependent integral intensities based on the models presented above.

The results for the vertical intensity in shallow ($X < 100$ m.w.e.) and medium (100 m.w.e. $< X <$ 1000 m.w.e.) depths are shown in Figure 3.2. Experimental data from different underground laboratories (for references see Table 6.5) and low-level experiments [AAdA$^+$17, ABB$^+$] is included for the comparison of the different parameterisations discussed before. Smaller deviations between the

data points and the plotted functions occur since the data is not corrected for the geomagnetic location or altitude, which are often not reported together with the muon flux measurements. Some experiments only provide generously rounded attenuation factors, which are converted to integral intensities with an approximated uncertainty of 25 % in order to include these values here.

Figure 3.2 includes an additional approximation for the vertical intensity of cosmic muons. Theodorsson's empirical formula describes the attenuation of cosmic muons with a stated accuracy of 5 % below 100 m.w.e. and 10 % below 1000 m.w.e., respectively [The96, NGG$^+$16]. The vertical position of the curve (green line) in Figure 3.2 therefore depends strongly on the muon intensity at surface, that is used for the calculation. The shown curve is plotted for a surface muon flux of 140 muons/(m^2 s).

The fourth function (yellow line) in Figure 3.2 is given by C. Berger et al. (Fréjus Collaboration) [BFM$^+$89]. It shows the calculated vertical flux of cosmic muons at the location of their production within the atmosphere. It is plotted with coefficients from W. Rhode et al. (Fréjus Collaboration), which are obtained from experimental data of the Fréjus detector [R$^+$96]. Due to the deep underground location of this detector with an overburden of about 4800 m.w.e., only high energetic cosmic muons are measured and effects like the decay of cosmic muons can be neglected. Therefore, the vertical flux of cosmic muons at the location of their production can be measured.

By contrast, the previously discussed parameterisations by Bogdanova, Reyna /Bugaev and Theodorsson are based on measurements of the spectrum of cosmic muons at sea level. Thereby, effects such as the atmospheric depth of about 10.3 m.w.e. are neglected, which leads to the different trend at shallow depths below 100 m.w.e. visible in Figure 3.2.

However, amongst the discussed approximations of the cosmic muon flux the Reyna/Bugaev parameterisation is the most sufficient to directly describe the experimental data at shallow depths without further corrections necessary [Rey06]. It can be used for the approximation of the muonic background contribution for shallow underground experiments with overburdens of up to 100 m.w.e.. The results of the MC simulations performed for the DLB and based on the Reyna/Bugaev model are discussed in Section 5.2.

Figure A.1 in Appendix A shows the integral intensity of cosmic muons over a larger range of depths, up until 10 km.w.e.. The figure also includes additional experimental data from deep underground laboratories and recently reported measurements of the cosmic muon flux from deep underwater exper-

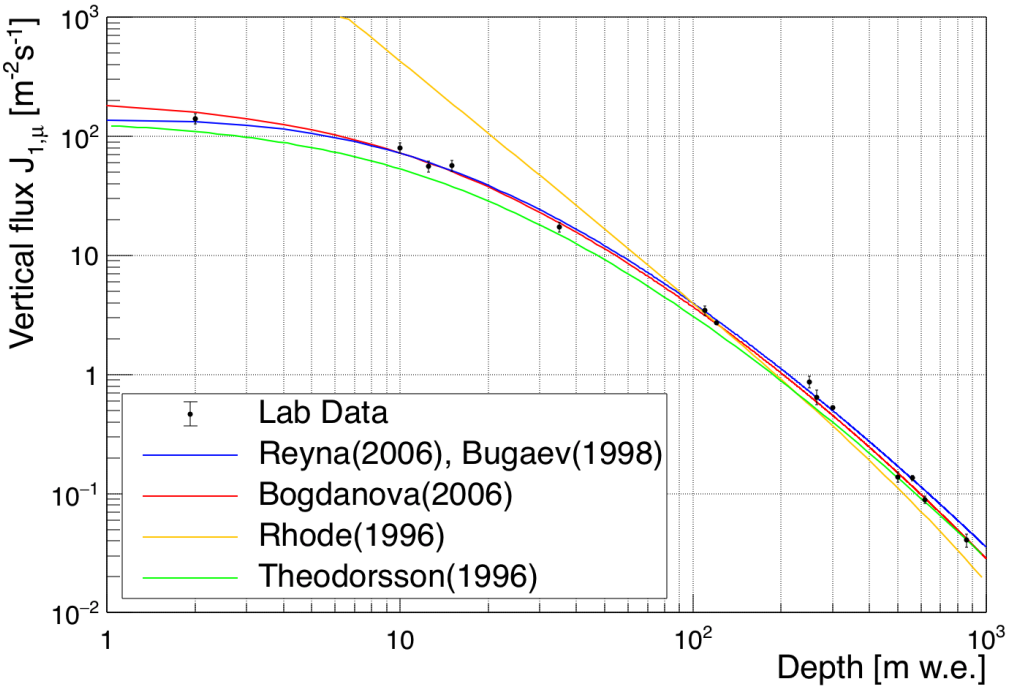

Figure 3.2.: Depth intensity relation for cosmic muons between 1 m.w.e. and 1 km.w.e.. For references of the displayed experimental data of different underground laboratories see Table 6.5 and [AAdA+17, ABB+].

iments [AAA+15]. The parameterisations used to approximate of the cosmic muon flux at shallow depths fail to reproduce the vertical flux of cosmic muons at larger depths.

3.2.2. Cosmic muon-induced background

Cosmic muons are very penetrating particles and therefore a major source of background in low-level experiments, even if these are located underground. In this section direct interactions of cosmic muons that lead to background contributions will be discussed. Indirect contributions from muons via tertiary neutrons and activation are focussed on in the following Sections 3.2.3 and 3.2.4.

Direct hits of the germanium crystal by cosmic muons will result in energy depositions of tens of MeV, depending on the energy of the incident muon, the geometry of the detector and the path of the specific muon inside the crystal. The mean stopping power of cosmic muons in germanium is 1.370 MeV cm^2/g.
With a density of 5.323 g/cm^3 for germanium this leads to a mean energy deposition of 7.292 MeV per cm of germanium [GMS01]. In case of the DLB's

germanium detector geometry, the mean energy deposition is about 48 MeV. Measurements in the high-energy range in [Ned09] as well as MC simulations of the cosmic muon induced background in [Ger16] confirmed this. Due to the large amount of energy deposited by direct muon-interactions, these events do not interfere with normal gamma ray spectrometry measurements, which are taking place at much lower energies, usually below 3 MeV.

The majority of background events in the relevant energy interval for gamma ray spectroscopy is caused by the deceleration of cosmic muons, that results in the production of electron-proton showers from delta electrons, direct electron-positron pair production and bremsstrahlung [Heu95]. The resulting spectrum is dominated by a continuous distribution of counts due to the bremsstrahlung. Additionally, there is a superimposed peak at 511 keV, caused by annihilation radiation from pair production or μ^+ decays. The intensity of this peak depends strongly on the incident muon flux, but also on the material and amount of the shielding. Decelerated negative muons may be captured by a nucleus of the high-Z shielding. Consequently, gamma rays as well as fast neutrons are emitted by the de-exciting nucleus. Depending on the incident muon intensity and the size of the shielding, a significant neutron flux can be the result. Those neutrons can induce additional contributions to the background spectrum, that are discussed in the following section.

3.2.3. Cosmic neutron-induced background

The background induced by neutrons is still a rather poorly understood component for germanium detectors in low-level gamma spectrometry [BVP18]. Depending on the depth of a laboratory, the production mechanisms for neutrons, that penetrate the system, change.
In surface-laboratories, neutrons are mostly part of hadronic showers of the secondary cosmic radiation and therefore called secondary neutrons. At depths below 10 m.w.e. the dominating neutron flux is caused by cosmic muon-interactions inside the shielding material, and secondary neutrons may be negligible. Muon induced neutrons are so-called tertiary neutrons. In deep underground facilities, below several hundred m.w.e., the neutrons from spontaneous fission and (α, n)-reactions from natural radionuclide chains inside the walls and surroundings of the facility become more important. Below depths of 1 km.w.e. fission processes and (α, n)-reactions are even the dominating sources for neutrons penetrating a

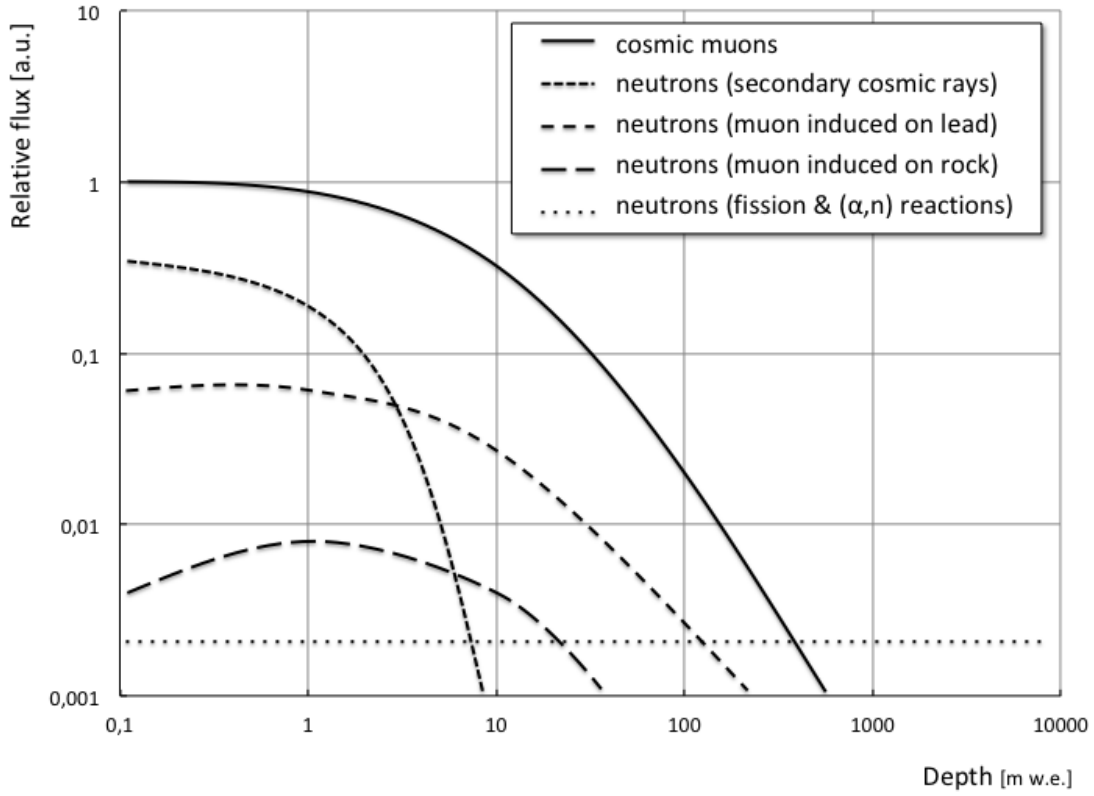

Figure 3.3.: Particle fluxes of cosmic muons and neutrons from different origins in dependence of depth in m.w.e.. The particle flux composition for the DLB can be seen at a depth of 10 m.w.e.. Adapted after Figure 13.17 from G. Gilmore [Gil08].

low-background experiment. This causes adapted shielding designs, which differ from the layouts at shallow depths primarily by having the neutron absorber placed at the outside of a lead shielding instead of it being integrated into the lead layers (see Section 4.3 [E$^+$16b]).

The different particle fluxes for the mentioned production mechanisms of neutrons are illustrated in Figure 3.3 where, for reference, the decrease of the cosmic muon intensity with depth is indicated as well. Neutrons induced by muon-interactions with the (rock) overburden are usually of less importance. The plot shows, that inside the 10 m.w.e. outer shielding of the DLB (see Section 4.1), the most dominating component of cosmic rays are muons. While direct cosmic muon-induced background components can effectively be reduced by active suppression techniques, e.g. active muon veto detectors as discussed in Section 4.4, neutron-induced background components have to be addressed separately.

Secondary neutrons are however, strongly attenuated and the neutron flux is dominated by tertiary neutrons formed in muon-lead interactions. According to Theodorsson [The96], the attenuation of secondary neutrons can be estimated by

$$A_n \sim \exp\left(-d/1.6\right) \quad , \tag{3.10}$$

where d gives the overburden in m.w.e.. With 10 m.w.e. the secondary neutron-component is attenuated to less than 0.2 %. The flux of secondary neutrons inside the DLB's outer shielding can therefore be estimated to about $0.12\,\text{neutrons}/(\text{m}^2\,\text{s})$ and thereby about three orders of magnitude less then the cosmic muon flux. At a depth of 17 m.w.e. a neutron flux of $0.081\,\text{neutrons}/(\text{m}^2\,\text{s})$ was measured [Nie08].

From Figure 3.3 it can be seen, that the overall neutron flux at a depth of 10 m.w.e. is dominated by tertiary neutrons. Both, neutrons from rock-interactions as well as those from fission and (α, n)-reactions are negligible at this depth, especially if neutron absorbers are used inside the detector's shielding. After the capture of a slow negative muon, several microseconds can pass until the muon is absorbed by the nucleus and one or several tertiary neutrons are emitted [B$^+$06]. Hence, background components that are (tertiary) neutron-induced are not completely suppressed by active muon veto detectors.

During the capture of a negative muon, the atomic number of the nucleus is decreased by one and the excited nucleus emits gamma rays and fast neutrons when the structure is re-arranged. G. Heusser calculates the flux of fast neutrons produced by muon capture to be $1.1\,\text{neutrons}/(\text{m}^2\,\text{s})$ for a cosmic muon flux of $80\,\text{muons}/(\text{m}^2\,\text{s})$, which is close to the muon flux measured inside the DLB [Heu95]. These fast neutrons can lead to activation and excitation of the shielding material and the detector itself by (n, p), (n, α), $(n, 2n)$ and $(n, n'\gamma)$ reactions [Gil08].

The interactions of fast neutrons with the different isotopes of the germanium crystal lead to broadened peaks with asymmetric shapes to higher energies, due to the nuclear recoil of the target nucleus, which is creating electron-hole pairs inside the detector. Inelastic scattering via $(n, n'\gamma)$ reactions on ^{72}Ge and ^{74}Ge, for example, leads almost immediately (compared to the charge collection time) to a de-excitation of the nucleus with 691.4 keV and 595.9 keV gamma rays, respectively [Gil08].

In contrast to inelastic neutron scattering on germanium nuclei, the interaction in materials around the detector crystal leads to sharp peaks in the spectrum since the recoil energy of the target nucleus remains in the material and only the emitted gamma ray has a certain chance to be detected in the germanium detector. Typical isotopes of shielding materials that contribute to the background spectrum due to neutron interactions are for example ^{63}Cu, ^{65}Cu, ^{206}Pb or ^{207}Pb.

Thermal neutrons on the other hand will enable several neutron capture reactions (${}^{A}_{Z}X(n,\gamma){}^{A+1}_{Z}X$), that lead to prompt gamma rays as well as decay gamma rays from the capture products [Gil08]. If the half-life of the de-excitation of these metastable states is longer than the applied rejection time, the subsequent background contributions are not suppressed by active reduction techniques such as muon veto systems. A list of several typical neutron-induced gamma-rays is given in Table 3.3. Only gamma rays where the half-life of the excited or metastable radionuclide is shorter than the rejection time can be suppressed by active reduction systems that are placed outside of the lead shielding. The rejection time for the muon veto of the DLB is 50 µs.

Even if neutron-induced gamma rays are not suppressed by active reduction techniques, their intensity can still be reduced by an effective neutron shielding. Since most of the tertiary neutrons are produced in the high Z lead shielding, the neutron shield must be placed inside the lead shield, which on the other hand also increases the potential target for cosmic muon interactions in the first place.

Neutron shielding consist of low Z materials, so-called moderators, to thermalise fast neutrons. Usually materials like paraffin or polyethylene are used for neutron-moderation and components with large thermal neutron cross sections are added to completely absorb tertiary neutrons. Boron loaded polyethylene (BPE), which is commonly used for this purpose in shallow as well as deep underground laboratories (see e.g. [PBJV08, HWH^{+}15, E^{+}16b]) is used inside the inner shielding of the DLB that is discussed in Section 4.3. Scintillating material that is sensitive to neutrons, e.g. organic plastic scintillators, may be used alternatively to be able to actively veto neutron-induced background contributions [Heu95, HWH^{+}15].

Regardless of the origin, the suppression or rejection of neutron-induced background components and the understanding of these background contributions is a central issue for many experiments, also beyond low-level gamma ray spectrometry. MC simulations are crucial for the understanding of the neutron con-

Table 3.3.: Isotopes of germanium and copper that are subject to neutron reactions. Energies labelled with (b,a) give broadened and asymetric peaks,respectively. The label (s) denotes the sum energy of two gamma rays emitted within a very short time. Data taken from [Heu93] and [NNDCN18].

Isotope	Abundance [%]	Neutron reactions	Half-life of product	Energy [keV]	Remarks
^{70}Ge	20.5	$^{70}\mathrm{Ge}(n,\gamma)^{71m}\mathrm{Ge}$	79 ns	174.9	
			20.4 ms	198.4	
^{72}Ge	27.4	$^{72}\mathrm{Ge}(n,\gamma)^{73m}\mathrm{Ge}$	499 ms	53.4	
			499 ms	66.7	(s)
		$^{72}\mathrm{Ge}(n,n')^{72*}\mathrm{Ge}$	444.2 ns	691.0	(b,a)
			3.35 ps	834.0	(b,a)
^{73}Ge	7.8	$^{73}\mathrm{Ge}(n,n')^{73*}\mathrm{Ge}$	1.74 ns	68.8	(b,a)
^{74}Ge	36.5	$^{74}\mathrm{Ge}(n,\gamma)^{75m}\mathrm{Ge}$	47.7 s	139.7	
		$^{74}\mathrm{Ge}(n,2n)^{73m}\mathrm{Ge}$	499 ms	53.4	
		$^{74}\mathrm{Ge}(n,n')^{74*}\mathrm{Ge}$	12.41 ps	595.8	(b,a)
^{76}Ge	7.8	$^{76}\mathrm{Ge}(n,\gamma)^{77m}\mathrm{Ge}$	52.9 s	159.7	
		$^{76}\mathrm{Ge}(n,2n)^{75m}\mathrm{Ge}$	47.7 s	139.7	
		$^{76}\mathrm{Ge}(n,n')^{76*}\mathrm{Ge}$	18.2 ps	562.9	
^{63}Cu	69.2	$^{63}\mathrm{Cu}(n,\gamma)^{64*}\mathrm{Cu}$	21 ps	159.3	
			< 9 ps	278.3	
		$^{63}\mathrm{Cu}(n,n')^{63*}\mathrm{Cu}$	0.198 ps	669.6	
			0.57 ps	962.1	
			0.61 ps	1327.0	
			1.7 ps	1412.1	
			116 fs	1547.0	
^{65}Cu	30.8	$^{65}\mathrm{Cu}(n,2n)^{64*}\mathrm{Cu}$	21 ps	159.3	
			< 9 ps	278.3	
		$^{65}\mathrm{Cu}(n,\gamma)^{66*}\mathrm{Cu}$	n.a.	186.0	
		$^{65}\mathrm{Cu}(n,n')^{65*}\mathrm{Cu}$	0.282 ps	1115.5	
			0.41 ps	1481.7	

tribution to the residual background of an experiment and the consequential optimisation of rejection techniques. So far, studies (both measurements and simulations) mainly focussed on the interactions of neutrons with germanium to provide important knowledge of germanium peak shapes. Recently, the investigations are also extended to more complex background compositions with the help of MC simulations [BVP18].

3.2.4. Cosmogenic activation

Shielding materials (e.g. copper or steel), the detector housing (e.g. aluminium) or the germanium crystal itself are subject to cosmogenic activation when exposed to cosmic radiation. Radionuclides may then be produced during the production process or during storage above ground, but also during operation if thermal neutrons are present inside the shielding. The activation by the hadronic cosmic component can even lead to activity levels higher than the residual contamination with primordial radionuclides [Heu95]. This will lead to characteristic peaks in the background spectrum of the detector. However, cosmogenic radionuclides in low-level spectrometry are usually shorter-lived and often only clearly visible in the background spectrum at the beginning of an underground operation.

^{7}Be or ^{14}C for example are produced during spallation reactions of cosmic particles with oxygen and nitrogen in the atmosphere [Lau17]. Due to the permanent activation and decay, the content of ^{14}C is constant in the atmosphere and since breathing plants and animals are exposed to this constant levels until their death, the radiocarbon method can be used for their age estimation [Lib64]. Other cosmogenic radionuclides such as ^{3}H, ^{10}Be or ^{36}Cl are negligible in most low-level gamma ray spectrometry applications, although they are of primary interest in Earth science for example [Heu95]. In some special cases, for example if conductive silver is used for the electrical contacting of detectors, more uncommon cosmogenic radionuclei are of importance. During the activation of silver by cosmic neutrons significant amounts of ^{108m}Ag and ^{110m}Ag can be produced [Ned14].

The cosmogenic radionuclides which are produced directly from germanium, in addition to those from Table 3.3, are for example ^{54}Mn, $^{56-58}$Co and ^{65}Zn. Additionally, ^{68}Ge is produced by cosmic neutrons via the $^{70}\mathrm{Ge}(n,3n)$ reaction. It decays with a half-life of 270.95 d via electron capture and no gamma ray emis-

sion into ^{68}Ga, that further decays with a half-life of 67.83 min through beta plus and electron capture decays with associated gamma rays [NNDCN18]. At sea level, activity levels of tens to hundreds of µBq/kg of germanium can be reached [PBJV08]. Up to a few mBq/kg are possible, depending on the height above sea level during storage [LH09]. The activation peaks from the germanium crystal itself can clearly be identified due to their associated peaks caused by summing with electron capture X-rays, which are otherwise absorbed before reaching the sensitive volume [Gil08].

Shielding materials such as copper and iron are subject to cosmogenic activation as well, which is especially crucial since these materials are used for parts in the very close proximity of the detector. The DLB's innermost shielding layer and detector cup, that is holding the crystal, are made of copper, the detector arm is made of stainless steel. Exposed to cosmic muon-induced fast neutrons, radionuclides like ^{57}Co, ^{58}Co and ^{59}Fe with half-lives less than one year are produced in copper as well as longer-lived radionuclides, such as ^{60}Co with a half-life of more than five years. See Section 7.1 for the analysis of these background contributions to the residual background of the DLB. Typical cosmogenics in iron are ^{52}Mn and ^{54}Mn in addition to the aforementioned ^{60}Co contaminations. Depending on the composition of the actual alloy of stainless steel, additional radionuclides can be formed trough activation of nickel or chrome as well [LH09].

After a rather long time of shielded operation, activation and decay of a specific isotope lead to a saturated level of activity, which strongly depends on the depth of the laboratory. For ultra-low-background applications cosmogenic activation products are sometimes more important than intrinsic contaminations of the natural decay chains. To avoid activation of the crucial parts of a detector system, it is recommended to have the materials stored underground as soon as possible after their production. The production process, of course, needs to be optimised for background reduction as well, i.e. additional contamination is to be avoided. For further background reduction, it is even discussed to have germanium detector crystals grown directly underground [LHG$^+$04]. Shielding material like oxygen-free high thermal conductivity (OFHC) copper is already produced underground, e.g. at the LSC underground laboratory [BBI$^+$17].

4. Dortmund Low Background Facility

The DLB has been built to enable high sensitive low-level gamma ray spectrometry. Low-level in this context means the ability to measure specific activities below 1 Bq/kg accurately. Therefore a HPGe detector is placed inside a massive shielding and operated with regard of lowering the background and optimising the sensitivity.

If background contributions are reduced by the removal of the radionuclides from the vicinity of the detector or by placing the detector in a location with an environment of lower background, these methods are referred to as passive shielding techniques. In contrast, methods that identify counts in the spectrum as originating from background and prevent the recoding of those events by the multi channel analyzer (MCA) are referred to as active reduction techniques.

4.1. Outer shielding

If a low-background environment is desired for spectrometry measurements, the detector system is usually situated underground. This either means that the facility is located literally underground, i.e. below the surface or ground level [HCK+00], or that the facility is placed alongside a tunnel that crosses a massive rock overburden [HLN06, LBP+15]. If these options are not available, unconventional overburdens are utilised to shield the detector system against cosmic radiation as much as possible. This may be an old cooling cellar of a brewery [KDL+09], the basement of a building [HWH+15] or the lowest floor of an underground car park [PCLP04]. The CELLAR network classifies 10 m.w.e. of overburden for a detector system as 'being underground'.

The DLB is located above ground in the experimental hall of the Faculty of Physics at the TU Dortmund University. A massive overburden was especially constructed from the previous shielding of a betatron to shield the detector system against cosmic radiation. 1 m to 1.5 m thick blocks of barite concrete were

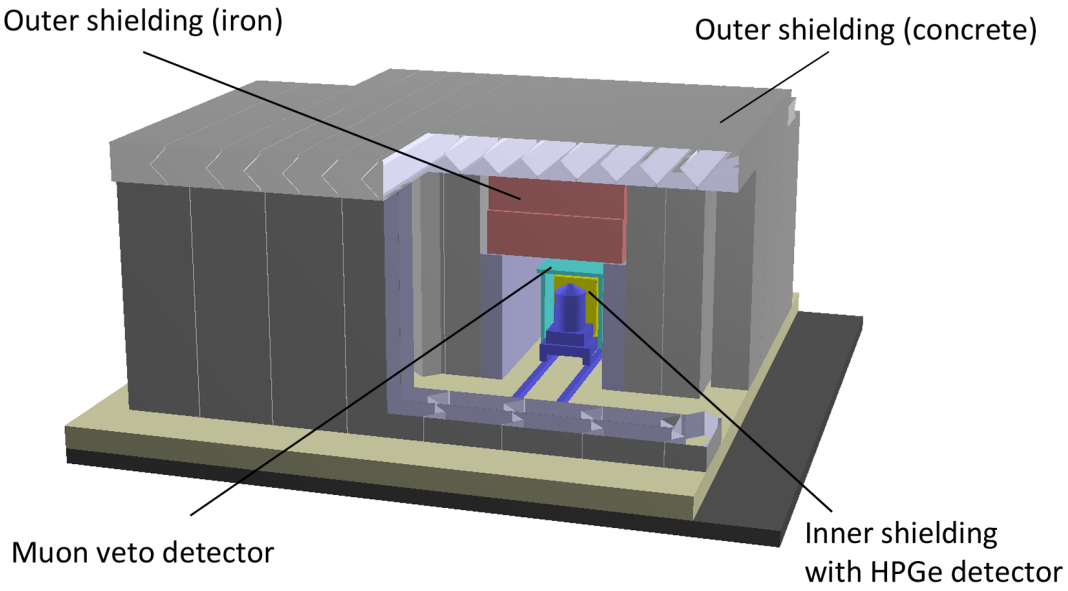

Figure 4.1.: Digital model of the Dortmund Low Background Facility implemented in GDML.

used to assemble an enclosure of roughly 7 m × 7.5 m × 3.5 m outer dimensions, that houses a control room as well as a measuring tunnel for the detector system [Ned14]. Additional cast iron blocks of 1.17 m thickness form the ceiling of this measuring tunnel that has the dimensions of 3 m × 1.4 m × 1.7 m ($l \times w \times h$). The outer shielding, also referred to as overburden, has a total mass of more than 368 t, thereof 43 t of cast iron and 319 t of concrete. A digital model of the outer shielding including the active muon veto and the inner shielding is illustrated in Figure 4.1. Details on the construction of the outer shielding can be found in [Ned09] and [Gas09].

The outer shielding corresponds to an angular distribution in overburden that is shown in m.w.e. in Figure 4.2. While the contour of the cast iron ceiling above the detector position is clearly visible in the figure with up to 12 m.w.e. of overburden, at least 10 m.w.e. are covering the germanium detector for zenith angles θ of less than 45°. For larger angles, the overburden decreases to about 5 m.w.e. at θ =90°, but since the cosmic muon flux decreases approximately with $\cos^2(\theta)$, the overburden becomes less important for larger zenith angles. The calculation for Figure 4.2 is performed analytically by integration over the density of the material along a path for the entire solid angle of the upper hemisphere as seen by the germanium detector [Ned09].

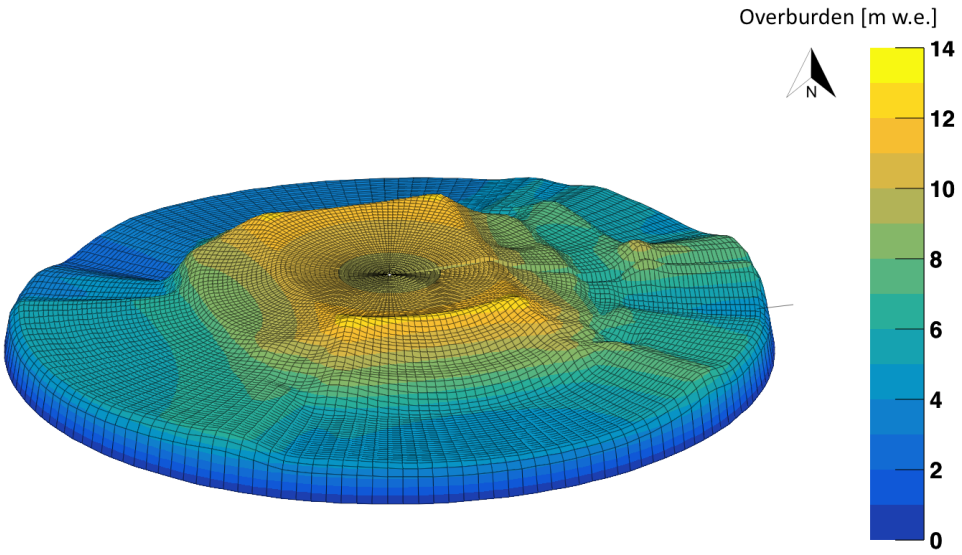

Figure 4.2.: Angular distribtion of the overburden of the DLB. The zenith angle θ corresponds to the radius, the color coding to the overburden in meters of water equivalent (m.w.e.). The influence of the cuboid-shaped iron block directly above the germanium detector is clearly visible.

The outer shielding is sufficiently shielding the soft component of the cosmic radiation incident on the detector system, that is housed inside. As it was discussed in Section 3.2, the soft component, i.e. electrons, positrons and photons, of the secondary cosmic radiation is stopped by 170 g/cm^2. Ten meters of water equivalent are therefore sufficient to completely stop this component.

The hadronic component on the other hand can not be stopped completely by the outer shielding. The particle flux however, is decreased considerably by three orders of magnitude to practically negligible levels. Protons for example need at least an energy of 15 GeV to penetrate 10 m.w.e. of overburden [Ned09]. The integral intensity of protons reaching energies above this threshold is some orders of magnitude smaller than the overall flux and therefore neglected inside the outer shielding [Gri01].
Neutrons are attenuated to the same extent, although their higher initial flux at sea level causes about ten times more secondary neutrons than protons beneath the DLB's overburden. Additional neutrons are also produced in the first few meters of water equivalent of the overburden by secondary protons, but they only contribute insignificantly to the total neutron flux below 10 m.w.e. [The96]. However, tertiary neutrons, that are induced by cosmic muon interactions have to be considered for the design of an inner shielding around the germanium detector.

Cosmic muons are the only cosmic ray particles that are able to penetrate the overburden to a considerable extent. T. Neddermann calculated the minimal energy for a cosmic muon to pass through the barite concrete roof and the cast iron ceiling to 1.56 GeV [Ned09]. However, these calculations were based on a mean muon energy of only 1 GeV and only ionisation effects were considered. Based on Equation (3.7), that is evaluated with constant values for a and b at a muon energy of 4 GeV taken from [GMS01]. Thereby, the minimal energy to penetrate the concrete roof and iron ceiling is now calculated to about 1.808 GeV. The reduction of the cosmic muon flux can then be approximated with Equation (3.9), which is based on the Reyna/Bugaev approximation for the vertical differential muon momentum spectrum (see Equation (3.4)). About 45 % reduction in flux are calculated using this equation, which results in a muon flux of about 81 muons/$(\mathrm{m}^2\,\mathrm{s})$ inside the DLB's outer shielding.

Additional shielding techniques, both active and passive, therefore have to be employed to reduced background that is induced by the penetrating portion of the cosmic rays.

4.2. Airborne radon

For Germany, the BFS reports a value of 50 $\mathrm{Bq/m^3}$ for the average radon concentration indoors [Bun18]. However, the average radon concentration in free air at the location of the TU Dortmund University is reported ranging between 3 and 6 $\mathrm{Bq/m^3}$, while the radon concentration in the ground is reported with an average value of 35 $\mathrm{Bq/m^3}$ [Bun18].

In 2010, without any radon reduction-measures, the radon concentration inside the outer shielding of the DLB was measured with a mean value of 32.11(96) $\mathrm{Bq/m^3}$. Completely sealing the outer shielding and actively ventilating the inside to maintain a slight overpressure resulted in a mean radon concentration of 20.86(45) $\mathrm{Bq/m^3}$. Uncertainties for both measurements are only of statistical nature [Ned14]. The ventilation system takes filtered air from the experimental hall, that serves as thermal buffer and indirectly provides fresh air with a lower radon content.

Since 2016, the radon levels inside the outer shielding are monitored continuously with a *CANARY*pro radon monitoring system. One year of continuous data, recorded between 2016 and 2017, is used to obtain an average concentration of: 29.5(63) $\mathrm{Bq/m^3}$ with daily mean values ranging between 11.0(104) $\mathrm{Bq/m^3}$

and $59.9(224)\,\mathrm{Bq/m^3}$. The concentration mentioned above was measured for a relatively short period of time of only two days in February 2010. Long term variations may therefore not be covered by this mean value.

Additionally, several environmental parameters such as the air's temperature, humidity and pressure are recorded inside the outer shielding since 2016 as well. A preliminary evaluation of this data indicates a correlation between the radon concentration and the air temperature. Similar effects have been reported in the literature before, since the radon diffusion coefficient, emanation coefficient and exhalation rate are known to be correlated with the indoor air temperature and relative humidity [AMG13]. Other studies, however, do not find a clear correlation between indoor temperature and indoor radon concentration [XLK15]. Since fresh air is constantly added to the compartment, additional radon from the outside may be introduced this way. Comparing the average radon concentration in free air with the measured value on the other hand, indicates that most of the radon inside the outer shielding is probably evaporating from the barite concrete walls and not introduced via the ventilating system.

The measurement stated above was performed during the winter of 2010. Therefore the relatively low result may have been caused by a lower than average air temperature. However, more data needs to be recorded over a longer time period of several years and additional analysis should be performed in order to reduce the radon concentration in the facilities air as far as possible.

4.3. Inner shielding

To shield the germanium detector against environmental radioactivity and secondary as well as tertiary neutrons, the DLB features a multilayer inner shielding, especially designed for the above-ground operation, where the entire shield is exposed to cosmic radiation. The design is based on the shielding concept developed by W. Wahl [Wah07]. A very detailed description of the assembly, including the construction and cleaning procedures, can be found in [Gas09, Ned14].

The shielding's outer dimensions are $0.6\,\mathrm{m} \times 0.6\,\mathrm{m} \times 0.8\,\mathrm{m}$, with a total mass of 2.8 t. As shown in Figure 4.3, the shielding consists of five different layers. No more than 150 mm of lead are used to avoid an enhancement of tertiary neutron production.

In order to easily access the sample chamber without corrupting the shielding, a removable plug is installed on the top of the lead castle consisting of the same

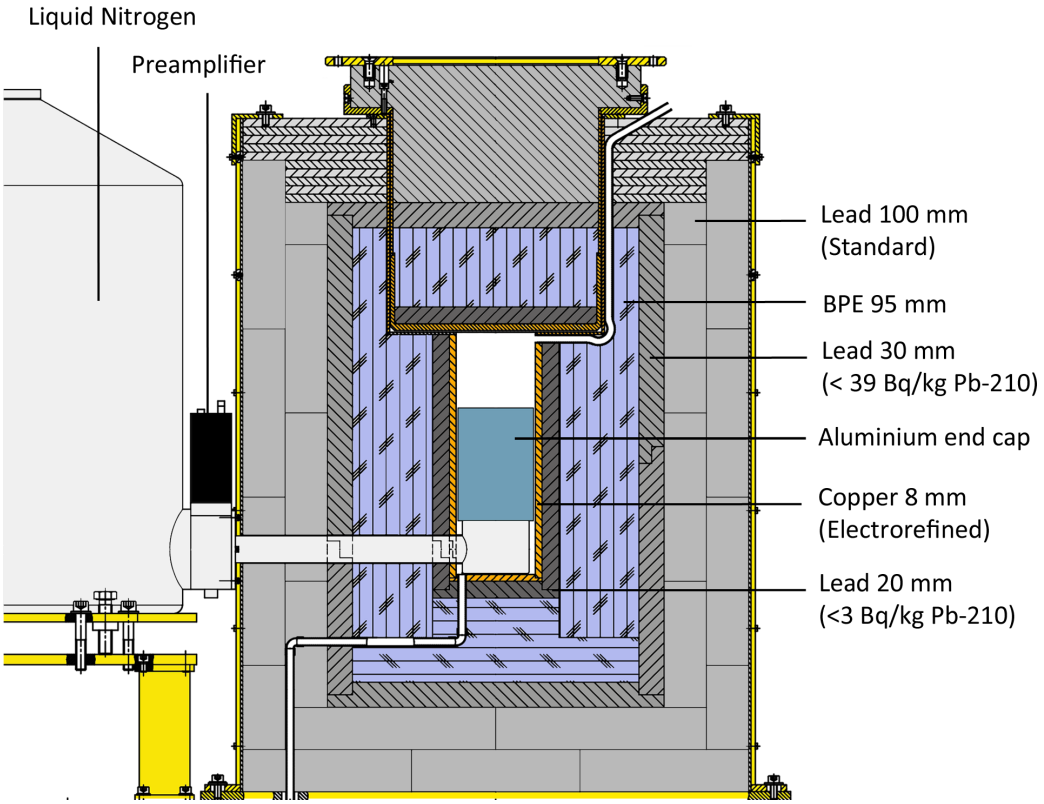

Figure 4.3.: Schematic drawing of the inner shielding-layers. Inner shielding and the liquid nitrogen dewar are mounted on a waggon that can be moved with an electrically powered engine.

multilayer layout as the rest of the shield. Only the thicknesses of the outermost lead layer and the copper pot enclosing the layers differ slightly from the structural design. The plug can be moved with an electrically powered crane which is installed in the laboratorie's ceiling.

The neutron shield is placed inside the massive shielding to minimise the effect of neutron interactions with the innermost layer of copper and any accompanying activation processes. Hence, most of the high-Z material is located outside, and tertiary neutrons induced by muons penetrating through the lead are moderated and finally stopped in large part within the BPE layer, which contains about 14.4 wt% hydrogen [WB09]. By mixing diboron trioxide into the material, a boron content of about 2.7 wt% is achieved. The neutron shield is positioned close to the detector, with only 20 mm of lead in between, for which reason it needs to be adequately radiopure. Screening measurements of the used material are reported in [Ned14].

Between the BPE and the germanium detector, an ultra-low-activity layer of

lead is placed to absorb the gamma rays that can be emitted during the neutron capture in boron. In 93.7 % of the $^{10}\mathrm{B}\,(n,\alpha)\,^{7}\mathrm{Li}$ reactions, a gamma ray of 477.6 keV is emitted by the excited ^{7}Li. The attenuation of the gamma ray intensity due to the innermost lead layer is analytically calculated to be 98.1 %. Due to the remarkable low-background levels achieved by the improvements reported in this work, the gamma rays stemming from the neutron-capture reaction can now be detected in the residual background spectrum (see Section 7.1).

The entire setup, including the inner shielding with the germanium detector inside, is mounted on a vibration-damped heavy-load wagon and can be moved on rails with an electrically powered engine. To achieve maximum angular coverage of the overburden, the wagon can be moved under the cast iron that forms a tunnel. Consequently, the setup is moved out of the tunnel to introduce or change samples and refill the nitrogen reservoir.

The inner shielding is surrounded by steel sheets which provide a sealing and encapsulation of the system against radioactivity from radon in the laboratory's air (compare Figure 4.3). Additionally, airborne radon is flushed out of the measuring chamber by constant evaporation of gaseous nitrogen from the detector-cooling dewar. The inner volume of the measurement chamber is exchanged completely in less than three minutes.

4.4. Muon veto detector

Due to the relatively shallow overburden of the DLB, it suffers from a considerable background contribution induced by cosmic radiation, mainly cosmic muons. An active cosmic muon veto detector is therefore employed to detect cosmic muons that are penetrating the inner shielding and reject their direct and indirect events from the measurement.

Plastic scintillators, that are read out by PMTs, are placed around the inner shielding, to achieve the best possible angular coverage around the detector while minimising the additional instrumentation. Organic plastic scintillators provide a high photon yield and fast signal times of a few nano seconds, making them suitable for trigger and veto detector applications. Since the veto is placed outside of the inner shielding, radiopurity of the scintillator and especially the PMT is not crucial. All used scintillators are polyvinyltoluene based and either *Saint Gobain* BC-408 or *ELJEN Technologies* EJ-200 with practically similar properties (see Table 2.1). The wavelength of maximal emission of the scintillation light is equal to the wavelength of maximal sensitivity for both of

the used PMTs: *Hamamatsu* R2490-05 and ET 9900B by *ET Enterprises*. Within characterisation measurements, a threshold is determined for each detector individually for optimal noise suppression. The output signals above these thresholds are converted to logical NIM pulses by NIM-standard discriminator modules. Logically combined to one overall signal, that is representing the entire muon veto detector, the signal is connected to the gate-input of the germanium detector's multi channel buffer (MCB).

The first version of a cosmic muon veto inside the DLB was realised shortly after the construction of the outer shielding with a Π-shaped detector, consisting of a top module and two lateral modules covering approximately the upper half of the inner shielding [Ned09, Ned14]. Scintillator plates of 5 mm thickness with an active area of 1220 mm × 200 mm are used. Their scintillation light is guided onto PMTs with PMMA light guides, that also transform the cross sections accordingly. Since minimal ionising particles, like cosmic muons with a mean energy of 4 GeV, lose on average about 2 MeV/cm in a plastic scintillator, the thickness of only 5 mm is insufficient for the discrimination between muonic or environmental gamma ray energy depositions. Therefore, the muon veto makes use of a setup with two separate scintillators covering the same sensitive area. If read out in coincidence, only particles passing both detectors are registered and consequently interpreted as cosmic muons. Environmental gamma rays, interacting in both scintillators randomly coincident, are very unlikely and therefore usually negligible. Although this two-scintillator setup results in a muon detection efficiency comparable to a thicker scintillation detectors, certain drawbacks remain. These are discussed in Chapter 6.

Due to the insufficient angular coverage of this initial muon veto detector design, it has been upgraded several times since. The author enlarged the veto detector during his master's thesis [Nit14] based on a design by T. Quante [Qua12] to increase the lateral side coverage of the inner shielding. Additionally, during this upgrade, a backside module was installed by M. Gerhardt [Ger14]. This upgrade stage made use only of 5 mm plastic scintillators and therefore used the two-layer setup throughout. This state of the veto detector and the impact on the residual background spectrum of the germanium detector is reported in [NGG+16].

Finally, the muon veto detector based on two-layered 5 mm plastic scintillators was completed with the addition of the remaining frontside module, between the inner shielding and the nitrogen dewar (compare Figure 4.3). Since this module

has only limited space available, the light-guided readout is modified based on a concept developed and tested during the author's bachelor thesis [Nit12]. The frontside module was installed within the master's thesis of M. Gerhardt [Ger16] and supervised by the author. The resulting background reduction as well as the different impacts of the individual veto modules are reported by the author in [NGGK17].

Compared to the initial veto detector design, the completed detector, that practically covers the entire solid angle of the upper hemisphere around the germanium detector, lowered the residual background count rate by a factor of two. Additionally, due to the consequent implementation of the two-layered scintillators, the signal-to-noise ratio (SNR) was increased, while keeping the veto-induced dead time of the gamma spectrometer at about 1.4 %, compared to 1.1 % when using the initial setup [Qua12]. The veto count rate of the complete muon veto was measured to be (275 ± 1) counts/s which has to be compared to the calculated cosmic muon flux of about 200 counts/s through the instrumented areas. The counts that are not induced by cosmic muons are caused by the insufficient discrimination between cosmic muons and environmental gamma radiation in the scintillators.

4.5. Germanium detector

The main component of the DLB is its HPGe detector in a ULB version manufactured by *Canberra Semiconductor NV* in Olen, Belgium. The standard electrode (p-type) semi-coaxial diode has a sensitive mass of (1.247 ± 0.002) kg with dimensions of 71 mm in diameter and 66 mm in length resulting in a volume of 234 cm^3 corresponding to a relative efficiency of 60 %. At 1332.5 keV (^{60}Co), the energy resolution quoted by the manufacturer is 1.84 keV (0.14 %) [Can09, Can10].

In addition to the parameters describing the germanium crystal quoted by the manufacturer, several measurements were performed to characterise the detector and its geometry accurately [Ned14]. Detailed information about the detector crystal is necessary for reliable MC simulations, that are used for the determination of the FEP detection efficiency.

The scanning of the front window of the sensitive crystal volume was performed after the installation of the detector. The dimensions of the sensitive crystal front window of the detector are determined by using a calibrated ^{241}Am source inside a custom-made collimator. It is placed on a positioning plate with precisely known positioning points across the detector end-cap. By using the

59.54 keV gamma rays as well as the peaks at 98.97 keV and 102.98 keV of ^{241}Am, an extensive study was performed to determine the exact position of the crystal as well as the homogeneity of the detector's front dead layer. The term dead layer refers to the outer electrode contact, which is not contributing to the sensitive crystal volume. The local thickness of the dead layer can be determined for each measuring point by calculating the ratio between the two peak areas, because the number of counts in the peak areas depends on the absorption coefficients between the source and the sensitive volume of the detector. The average count rate at 59.54 keV across the detector surface deviates by $-20\,\%$ to $+11\,\%$ of the overall mean count rate [Ned14].

A value for the dead layer thickness can then be calculated under the assumption that only the thickness is causing this effect. Additional measurements based on the same method are performed using a calibrated ^{133}Ba source. In the measured spectrum, the ratios of the peak areas of the gamma lines at 53.2 keV, 79.6 keV, 81.0 keV and 160.6 keV are determined. A weighted average of $437(16)\,\mu$m is then calculated for the effective dead layer thickness, by combination of the three different ratios [Ned14].

Permanent cooling with liquid nitrogen is provided by a ULB U-style cryostat which prevents any direct paths for radiation into the shielding. Except for two controlled thermal cycles, the detector has been kept permanently cooled since its delivery in 2008 to suppress slow diffusion of the lithium atoms of the outer contact into the crystal's bulk material. The detector is mounted inside a holder made of 99.99 % pure copper within an end cap made of radiopure aluminium with an uranium and thorium content of less than 1 part per billion (ppb) [Can08]. The aluminium end-cap and the thickness of the outer contact lead to a typical energy threshold of about 40 keV and low sensitivity to energies marginally above. Directly above the germanium detector is the measurement chamber of approximately $(94 \times 94 \times 93)\,\mathrm{mm}^3$ size.

The HPGe detector is regularly calibrated using a ^{232}Th source placed on top of the detector end cap. After fitting Gaussian functions to a list of standard-peaks in the spectrum, the resulting mean channels of the peaks are used for the linear calibration function. In general, maximum deviations between the measured energies and the known peak energies are well below 0.02 %. The energy resolution $\omega(E)$ of the HPGe detector depends strongly on the incident gamma ray energy and is here defined as full width at half maximum (FWHM) of the peak in keV. Its energy dependence is described with a curve parameterised as

$$\omega^2(E) = e^2 + p^2E + c^2E^2 \quad , \tag{4.1}$$

where the three parameters represent the electronic noise (e), the statistical fluctuation of the charge production (p) and the charge collection (c) [Gil08]. The energy resolution of the DLB's germanium detector at 1332.5 keV (^{60}Co) is measured to be (1.772 ± 0.001) keV, corresponding to a relative energy resolution of 0.13 %.

4.6. Data acquisition electronics

Figure 4.4 gives a schematic of the data acquisition (DAQ) used in the DLB. The illustration is an updated version of the DAQ system shown in [Ned14]. It already includes the veto detector modules with plastic scintillators of 50 mm thickness that were installed during this work (see Chapter 6). However, all basic modules and devices used are unchanged and the reader is referred to [Ned14] for a more detailed and complete description of the DLB's DAQ readout system. The brief overview given here is focused on the implementation of the muon veto detector.

The raw output signals of the individual PMTs of the different muon veto detector-modules are converted into fast negative NIM logic outputs by several discriminator units. Each threshold, adjustable per channel or unit, is chosen to match the amplification characteristics of the individual PMT. The signals are then checked for coincidences within the overlaying 5 mm scintillators. Eventually, the coincident signals are combined with the 50 mm scintillator signals within logical-OR units to one single overall veto signal.

For each overall veto trigger, provided by the muon veto detector, an adjustable time window is applied to the gate input of the MCA. All germanium detector signals are rejected for this duration and do not appear in the resulting spectrum. Typical values of 2 µs up to almost a millisecond can be found at other detector systems [Ned14]. However, the actual time window depends on the geometry and composition of the individual setup of the spectrometry system. A tradeoff between effective rejection of cosmic-induced events and maximum live time of the detector system has to be made. Studying the background count rate of the DLB's germanium detector in dependence of the applied rejection time window resulted in the optimum time window of 50 µs [Qua12]. This assures a high rejection efficiency with a sufficiently low veto-induced dead time of about 1.4 %, corresponding to the aforementioned overall veto count rate. In order to deter-

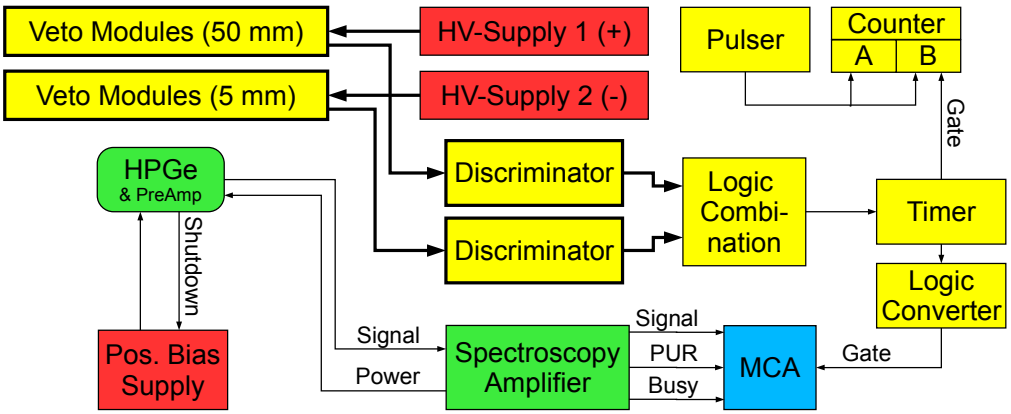

Figure 4.4.: Data acquisition electronics of the DLB. Bold lines indicate multiple connections and bold bordered modules indicate multiple devices of the same type. The logic combination module represents several logical units (concidences, multiplicity logic units and OR units), that are combining the discriminated signals coming from the PMTs so that the two-layer coverage is assured.

mine the relative dead time due to the muon veto, a counter is gated by the veto signal while counting pulses from a pulser. This number is then divided by the total number of pulses applied.

The chain of DAQ electronics ends with an *Ortec TRUMP®-PCI-8K* multi channel buffer (MCB), that receives the output signals of the germanium detector's preamplifier, including PUR and *BUSY* signals, as well as the overall muon veto signal at the gate-input. It is read out by the *Ortec Maestro®-32* multi channel analyzer (MCA) software. Recorded energy spectra are stored in ASCII SPE formatted files for later analysis (see Section 4.7). It is planed however, to replace the MCB with an event-based system based on three four-channel flash analog-to-digital converters (FADCs) with a sampling rate of 75 MHz. This allows for the simultaneous recording of several input channels individually, including timestamp information for all events. Thereby, some drawbacks of the MCB-based system can be overcome [Ned14]. The cosmic muon veto will then be applied to the measurement during offline analysis based on the timing information provided by the FADC. Preliminary tests are undergoing to investigate the energy calibration and energy resolution characteristics as well as timing-dependent parameters. The veto rejection time window of 50 µs for example has been confirmed using a FADC [Jan18].

4.7. Data analysis software

At the end of the DAQ electronics chain, the recorded energy spectra are stored in ASCII SPE files. The storage is automated and happens in predetermined time intervals, so-called *runs*. These time intervals define the minimal time resolution of the given overall measurement if a longer measurement is examined time-dependent. Each SPE file contains the start time of the measurement, the live time as provided by the MCA and the counts for each of the MCB's channels.

Actual processing and analysis of the obtained data is performed with ROOT [BR97]. Developed at CERN, ROOT is a data analysis framework that uses the programming language C++ and provides interactive data processing. Analysis within this work is performed with ROOT 5.34.23.

Raw data conversion, energy calibrations and energy resolution calibrations conducted during this work were performed with pre existing software tools. The determination of net peak areas is done with the standard DLB analysis tool `GeAna`. For a very detailed description of all DLB software tools and the internal workflow, the reader is referred to [Ned14] and the references therein. Only a brief overview of the three main classes is given here.

The `ge-multi-convertingtool` is used to convert all raw data from SPE files belonging to the same measurement into one ROOT output file. It is command line executable using the libraries of ROOT with several settings that are set when the tool is executed. The energy calibration is usually provided with a separate calibration file, containing the energy calibration function and the corresponding energy resolution function (Equation (4.1)). If needed the energy calibration can be set with specific values as well. Another option can be used to prevent the application of the externally provided veto-induced dead time for the calculation of the final live time of the measurement. For details on the determination of the so-called veto time see Section 4.6. The output file contains a calibrated sum spectrum of all runs, as well as the used calibration function and the corresponding resolution function.

The DLB is routinely checked in terms of energy calibration and energy resolution. Therefor measurements with known gamma ray emitters, e.g. ^{232}Th, are performed. These measurements can then be used to obtain calibration files that contain the energy calibration function as well as a energy resolution function. Additionally, the measured spectrum of the calibration source itself is stored in the calibration file. The class `GeCal` is used for this mostly automated

process [Qua12]. Based on a predefined list of common radionuclides, the peaks are located in the spectrum and fitted - including their local background regions - to obtain the calibration points.

`GeAna` is another class with a large number of methods and functions to be used with ROOT. The analysis of gamma ray spectra is based on the DIN ISO 11929:2011 analysis standard [DIN11]. If needed, analysis according to the older DIN 25482-5 analysis standard is still possible.

Briefly described, the workflow of `GeAna` is the following. A calibrated spectrum of the measurement is loaded as well as the adequate MC generated simulation spectrum for the radionuclides under investigation. Additionally, a background spectrum can also be loaded for peaked background correction, if peaks in the background spectrum are too close to the peaks under investigation. The start time of the measurement is extracted from the measurement and set as reference date as default. However, a definite reference date can be set separately. All relevant sample parameters such as its mass and dry-wet-ratio are entered.

The FEP detection efficiency is obtained from the provided MC simulation (see Chapter 5). Simulated energy spectra are convoluted with a energy resolution function, that is provided by the input file of the measurement, since charge transport and electrical fields are not included in the MC. The systematic uncertainty of the detection efficiency can be set separately since statistical uncertainties are usually negligible. 5 % are set for the uncertainty by default, which is based on the investigation of the energy dependence and precision of the FEP detection efficiency in [Ned14].

If needed, the standard values for decision error probabilities and their corresponding quantiles can be changed. By default, the values are set according to DIN ISO 11929:2011 (compare Section 2.2.4).

`GeAna` contains an extensive list of the commonly needed, most prevalent naturally occurring radionuclides with data taken from the Decay Data Evaluation Project (DDEP) [Lab18]. The predefined gamma ray energies are selected in such a way, that they are not subject to TCS and do not interfere with dominant gamma ray energies from other common radionuclides [Ned14]. If several gamma lines of one radionuclide are evaluated, the final result is calculated as a weighted mean of the individual activities. A detailed how-to manual with further commentary can be found in chapter 4.4 of [Ned14].

5. Monte Carlo Simulations

Geant4 is a MC framework, developed at CERN, for the simulation of particle transport trough matter in high energy physics [AAA+03]. It is used widely for particle and nuclear physics applications. The code simulates the interactions of particles traversing matter and covers all relevant physical processes for gamma ray spectrometry applications, including gamma ray and neutron processes [BVP18].
For the present work, Geant version 4.10 is used with the simulation program VENOM, which is developed by the COBRA collaboration and based on the low energy extensions of Geant4 [AAA+03] [Ned14, Köt12]. It provides particles, geometry interfaces, interaction models and algorithms of Geant4 for the generation of a particle or decay within an implemented geometry and the subsequent tracking of particles and their interactions in this geometry. The relevant output-data, which is produced during the tracking of particles, is extracted and stored in structured ROOT files for analysis. VENOM uses Geant's physics-list of the dark matter experiment (DMX) example, which includes all necessary physics processes for gamma ray spectrometry [Ned14]. Radioactive decays are simulated by the Geant4 radioactive decay module (GRDM), which is able to reproduce the emission characteristics of the radionuclides, including TCS. The charge transport inside the germanium crystal as well as the simulation of electric fields are not included in VENOM and the underlying Geant4. Therefore, the simulated spectra are convoluted with the energy dependent detector resolution, which is regularly obtained by calibration measurements.

A precise model of the geometry of the entire DLB is implemented in GDML, an XML based programming language. The model is based on the mechanical drawings that were created during the initial setup of the DLB, but has been updated and refined over the last years. Further modification and extension was done by the author so that the model now includes not only the very detailed inner shielding of the DLB but also the complete outer shielding and the cosmic

muon veto detector. Additionally, several standard sample matrices and source geometries are also implemented.

Whereas the dimensions of the outer and inner shielding are known precisely, several parameters of the germanium detector and its sensitive crystal volume, that are given by the manufacturer, need to be adapted to increase the precision of the MC generated energy spectra for the germanium detector. Comparative studies were performed to match the simulated data with calibration measurements. The model of the detector was optimised for various parameters of the germanium crystal, e.g. the dead layer thickness or the distance between the crystal and the end cap. Details on this procedure and the implemented values are provided by T. Neddermann [Ned14].

5.1. Full energy peak detection efficiency

For the accurate determination of specific activities within samples measured with an HPGe detector, the absolute FEP detection efficiency $\epsilon\left(E_\gamma\right)$ has to be known as precisely as possible. Therefore, corrections for the confined coverage of the solid angle of the sample as well as for self-absorption effects inside the sample and for the scattering of gamma rays into the surroundings of the detector have to be considered. Additionally, the total detection efficiency is strongly affected by the limited intrinsic efficiency for the detection of a gamma ray with a given energy inside the sensitive volume of the germanium crystal.

The FEP detection efficiency for a specific gamma ray energy and sample geometry can be obtained in different ways. Empirical measurements of reference sources with well known activities, geometries and compositions usually provide the most accurate results for the detection efficiency. If the reference source as well as the sample are of the same geometry and composition, even complicated effects like TCS are included correctly. These results can, to a limited degree, also be transferred and interpolated to samples with other gamma ray energies of interest or other geometries and sample matrices. But since it is practically impossible to have reference sources for all sample geometries, only some standardised sample geometries may be used to keep the uncertainty within reasonable ranges.

A more versatile approach is given by MC simulations. Since the interaction

mechanisms of gamma rays are well known, the FEP detection efficiency could, in principle, directly be calculated for the energy of interest in a given sample and detector geometry. In practice however, MC codes are used to reproduce the reality by simulation of the emission of particles and tracking these trough a detailed model of the measurement setup. Interactions of the simulated particles are included according to their probabilities given by their mathematical descriptions. By this method, extensive sample preparation and measurements of calibration sources for each new sample configuration can be avoided.

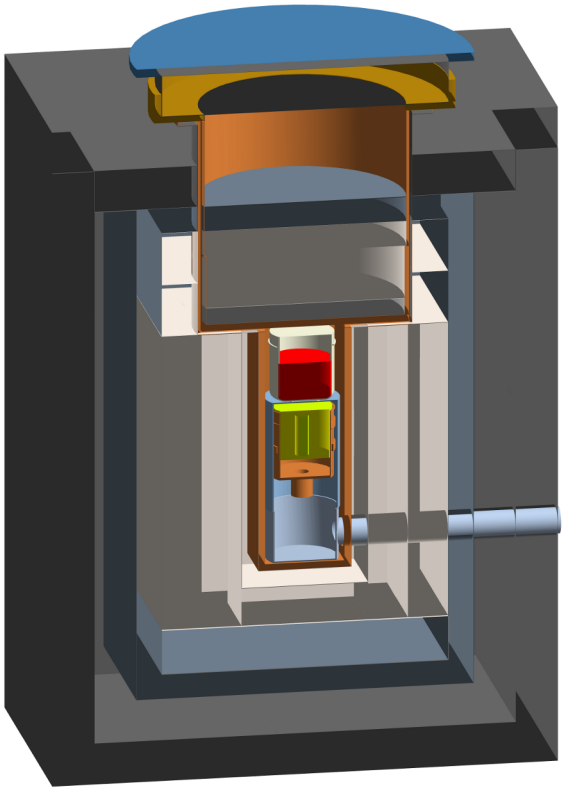

Figure 5.1.: GDML model of the geometry of the inner shielding including the germanium detector [Ned14]. Different shielding layers according to Figure 4.3. The germanium crystal is colored in yellow. A sample container, containing a red colored sample, is placed on top of the end cap.

The germanium detector as well as the inner shielding of the DLB have been implemented very detailed in GDML [Ned14]. A visualisation of the model can be seen in Figure 5.1. The different shielding layers are implemented based on mechanical drawings with materials as described in Section 4.3. Detector parameters, such as the crystals dead layer thickness or core hole dimensions have been optimised to achieve the best agreement between simulations and measurements [Ned14]. During routine simulations to determine the FEP detection efficiency of

a given sample, only the inner shielding, as seen in Figure 5.1, is used for the MC simulations, since influences from outside of the lead shielding are negligible.

5.2. Muonic background component

To further improve and decrease the background level of the DLB, the analysis of the residual background and its different components is necessary. The potential for improvement depends on the contribution of the individual sources of background to the overall background level. An analysis and discussion of the peaks found in the background spectrum is presented in Section 7.1.

Cosmic background contributions are dominating the background for all gamma ray spectrometry facilities that are only covered by a relatively shallow overburden. Active reduction techniques are therefore mandatory if certain sensitivity levels are aimed for. For facilities situated deeper underground, below several hundred meters of water equivalent, cosmic ray induced background becomes less significant and may be negligible depending on the other background components and the radiopurity of the setup. However, even these spectrometer might still benefit from muon veto detectors, even if only the top part of a shielding is instrumented, which is usually sufficient due to the angular distribution of the overburden [HMS+18]. In very deep underground laboratories such as the LNGS or Laboratoire Souterrain de Modane LSM, i.e. a few kilometres of water equivalent deep below the surface, the cosmic ray's contribute is less than 1 % to the remaining background spectrum. The radioactive contaminations of construction parts surrounding the detector are dominating the residual background for these systems [BBL+18].

Based on the reduction due to the cosmic muon veto detector, the muonic background component of the DLB's background spectrum without veto detector applied is at least 90 % (compare Table 6.3). Even with the muon veto detector applied during the data-taking, the muonic contribution is still relevant in comparison to the radioactive contamination of the setup. In order to understand the composition of the background spectrum, the contributions to the spectrum due to cosmic muons are studied with MC simulations carried out with Geant4 and VENOM. The typical energies of cosmic muons are in order of tens of GeV and more, thus making Geant4 a suitable simulation code for their interactions with matter.

In addition to the above mentioned GDML implementations of the inner

shielding, illustrated in Figure 5.1, the outer shielding of the DLB has also been implemented in GDML. A rendering of the entire DLB model is shown in Figure 4.1. This model is used for the MC simulation of the cosmic muon induced background component.

The propagation of cosmic radiation through the Earth's atmosphere is not considered during the simulations. Instead, the 'source' of cosmic muons within the MC model is placed directly above the outer shielding of the DLB and the muon-parameters are chosen according to cosmic muons at sea level as discussed in Section 3.2. Muons are generated within a thin plate with a size of 35 m $\times$ 35 m in downwards direction. This simplified model covers the zenith angle θ for the germanium detector up to 80.3°, accounting for more than 97 % of the angular distribution of cosmic muons, which are considered to be $\cos^2(\theta)$ distributed.

The default particle generator of VENOM for cosmic muons is optimised for underground laboratories at depths between 1 km.w.e. and 8 km.w.e., e.g. the LNGS at a depth of about 3.8 km.w.e.. Since extrapolating this generator to shallow depths of only a few meters of water equivalent does not give sufficient results, a new particle generator was added to the framework by M. Gerhardt [Ger16]. This new particle generator is based on the parametrisation of the cosmic muon momentum spectrum at sea level given by the Bogdanova approximation (see Equation (3.3) [B$^+$06]), which is discussed in Section 3.2. Their starting vertices are distributed with $\cos^2(\theta)$ and their charge ratio (μ^+/μ^-) is considered to be 1.28. In principle the particle generator can also be used to generate cosmic muons at a given shallow depth via the following relations [Ger16]: The depth-intensity-relation (Equation (3.9)) describes the intensity as a function of the muon's depth X. Their energy spectrum after traveling along a slanted path $X_S = X \cdot \sec(\theta)$ to reach the vertical depth X is given by

$$i\left(E_\mu, X, \theta\right) = j\left(E_\mu, \theta\right) \cdot \exp\left(bX_S\right) \quad , \tag{5.1}$$

with the differential energy spectrum $j\left(E_\mu, \theta\right)$ (compare Equation (3.3)) [O$^+$14]. The systematic uncertainty of the MC simulations is approximated with ± 10 %. Uncertainties on a similar scale are reported in the literature as well [BBL$^+$18].

For cosmic muons penetrating the germanium detector directly, an average energy deposition of about 45 MeV is expected due to the geometry of the germanium crystal. Indeed, the MC simulation revealed the expected peak at about 45 MeV, confirming the results of previous measurements [Ger16, Gas09]. A MC simulation was performed using the newly implemented particle generator for

cosmic muons to generate 33.1×10^9 events. Using the above mentioned particle generator, cosmic muons were simulated with an energy distribution according to a depth of $X = 0$ m.w.e., i.e. at the surface or at sea level. The obtained results are reported by M. Gerhardt [Ger16]. A reasonable agreement between simulation and measurement was achieved during these studies, confirming the above mentioned major contributions from cosmic muons to the the residual background spectrum of the DLB. Gerhardt concluded (without muon veto applied) that more than 95 % of the background is caused by cosmic muon induced events.

It was already discussed in Section 3.2, that the Reyna/Bugaev approximation (Equation (3.4)) of the cosmic muon flux at shallow depths is considered to be the preferential model (compare also the discussion in [Rey06]). A similar decision was made during MC simulations of the cosmic ray-induced background in a comparable 15 m.w.e.-overburden facility situated in Heidelberg, Germany [HMH16]. Therefore, with the help of M. Gerhardt, the Reyna/Bugaev parametrisation is implemented into VENOM as well and can be chosen alternatively for future simulation studies. 22.8×10^9 cosmic muons are generated in a second MC simulation with an energy distribution according to the approximation proposed by Bugaev with parameters according to Reyna (compare Section 3.2). The particle flux however, is corrected for the geomagnetic location and the altitude of the experimental hall, where the DLB is situated. The result of this simulation contains more than 54 000 entries in the energy spectrum and is shown in Figure 5.2 in comparison to the measured spectrum without muon veto detector applied to the MCB.

The simulation is scaled to the sensitive mass of the germanium detector in order to achieve comparability with other detectors. Additionally, the simulated spectrum is convoluted with an energy resolution function obtained from the measurement of the background. Based on the flux of cosmic muons at ground level of the DLB location, with adaptions according to the altitude and geomagnetic latitude (see discussion in Section 3.2), the MC is scaled to the corresponding time period. A cosmic muon flux of 146.3 muons/$(\mathrm{m}^2\,\mathrm{s})$ is used as scaling factor. Although this value is confirmed with laboratory measurements presented in the following Chapter 6, it should be noted that the resulting simulated spectrum is highly sensitive to this scaling factor. A systematic uncertainty 10 % can therefore be approximated (compare [BBL$^+$18]).

The comparison in Figure 5.2 between the scaled muon-induced spectrum produced by the MC simulation and the background spectrum measured without

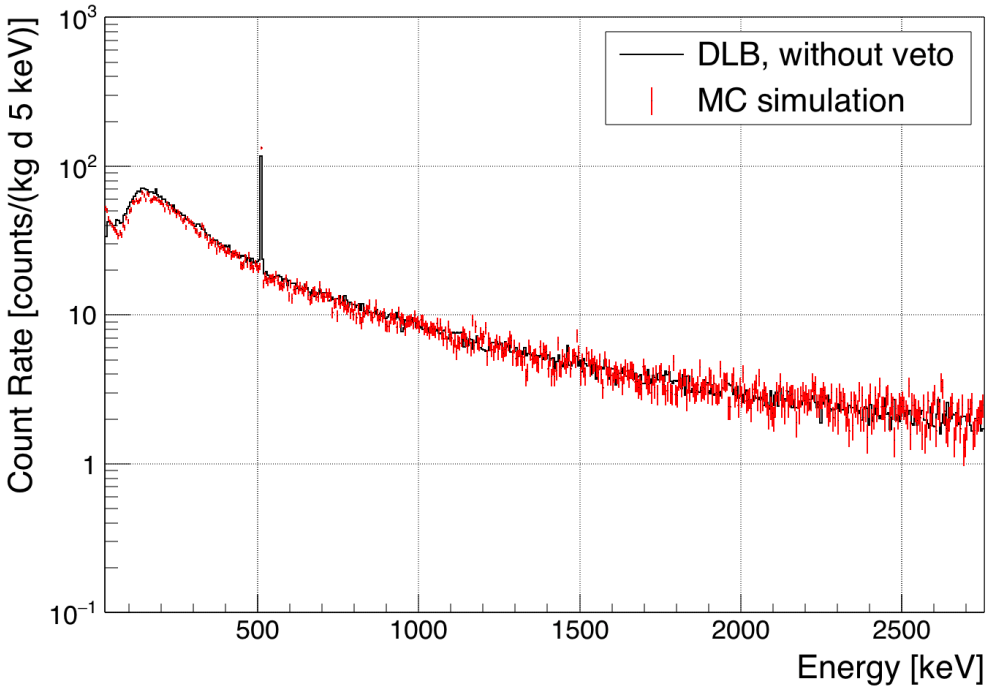

Figure 5.2.: Comparison between the MC simulation of the muon-induced spectrum and the measurement of the background spectrum without the muon veto.

the muon veto detector applied shows very good agreement. Small deviations can only be seen in the low energy part of the spectrum. This underestimation is most likely caused by the remaining background contributions from non-muonic sources inside the detector setup that are contained in the measurement but not in the simulated spectrum. The integral count rate of the simulated spectrum is calculated to 22.47(9) counts/(kg_{Ge}min) between 40 keV and 2700 keV, which accounts for 95.2 % of the measured count rate of 23.54(4) counts/(kg_{Ge}min) in the same energy interval. Contributions to the spectrum due to the intrinsic gamma ray background from the setup are consequently calculated to about 5 % or 1.07 counts/(kg_{Ge}min) of the integral count rate. This results in a muon veto efficiency of 96.5 %.

The aforementioned count rate strongly relies on the cosmic muon flux, that is used for the time-period scaling. In an alternative scaling method the MC spectrum is scaled onto the measured background spectrum in the energy region between 2650 and 2750 keV. In this region a negligible background contribution from non-muonic components is assumed, since naturally occurring gamma ray don't exceed energies of 2614.5 keV (see Section 3.1.1). Although the number of

events in this energy interval is limited and the systematic uncertainty therefore increased, a count rate of about 21 counts/(kg_{Ge}min) is obtained. Neglecting the uncertainties, the non-muonic background contribution can consequently be estimated with about 2.54 counts/(kg_{Ge}min). This is in contrast to the residual background level achieved with the improved muon veto detector. The measurement presented in Chapter 6 results in a background level of only 1.855(3) counts/(kg_{Ge}min). Additionally, the cosmic muon flux that results in this spectrum can be calculated to about 136.6/(m^2 s), which is, again, in contrast to measurements of the cosmic muon flux (compare Table 6.1 in Section 6.1 The lack of count rate in the ROI causes uncertainties too large, to obtain reliable results. However, the result may indicate a non-negligible contribution to the counts in the background spectrum above 2650 keV, that are non-muonic-induced.

If the muon veto detector, that is improved considerably within this work (compare Chapter 6), is applied to the gate-input of the detector's MCB, the cosmic muon induced events are rejected from the background spectrum to a large extend. However, it can be assumed that the energy depositions of any remaining muons result in the spectral shape. Therefore, the MC generated spectrum is scaled to the residual background spectrum with muon veto applied to estimate the background contribution from cosmic muons to the residual background spectrum. This is discussed in the context of the discussion of the composition of the residual background in Section 7.2.

6. Upgrade of the Cosmic Muon Veto Detector

In general, there is always an interest for increasing the sensitive of a detector system, especially in the field of low-level gamma ray spectrometry. As discussed in Chapter 3, the sensitivity (see Equation (2.13)) can be increased for example by increasing the detection efficiency of the germanium detector. But since this is usually not possible or feasible for an already existing detector system, the reduction of the background level is typically the only way of increasing the sensitivity.

The background of a given spectrometry system, such as the DLB, is always composed of different contributions, of which some are not practically reducible. For example contaminations of the detector itself or shielding material are usually not amendable with a justifiable investment after a system has been set up. Other contributions may decrease over time, such as cosmogenic nuclides that were produced during the production process or during storage time of the detector system's parts, without sufficient overburden to protect the material from activation from cosmic rays. After the installation in shallow or even deep underground laboratories, the activation is declining until an equilibrium state is reached, according to the remaining exposure to cosmic rays reaching the detector system. Cosmic rays itself can only be shielded marginally, especially for detector systems set up only with shallow overburdens of tens or a few hundreds of meters of water equivalent. Hence active veto systems have to be used to reduce this contribution and further improvement of these systems may have an impact on the remaining background level, which in turn increases the detection efficiency.

The MC simulation of the muon induced background component of the DLB (see Section 5.2) indicates that further improvement to the active veto system can decrease the background level considerably. For the completed muon veto detector, the normalised total integral count rate was $2.012(4)\,\mathrm{counts}/(\mathrm{kg_{Ge}min})$ between 40 keV and 2700 keV. The muonic component still represents ap-

proximately half of this residual background count rate. With the remaining other half being induced by other background sources, most likely by the detector's and the shielding's intrinsic contaminations [NGGK17]. Although this shows that the remaining background spectrum of the DLB is no longer dominated by muon-induced signals, the muonic component still can not be neglected. Additionally, the residual background spectrum does not show a steep decline for energies above the 2614 keV line from ^{208}Tl, which would be expected for a spectrum that is strongly dominated by gamma ray interactions.

The design of the muon veto detector of the DLB, that is described in Chapter 4, suffers from a few drawbacks such as the relatively thin plastic scintillators, which can not sufficiently discriminate between muonic and non-muonic energy depositions, thereby increasing the veto count rate unnecessarily. Although the two-layered setup with coincidence-readout overcomes most of this drawback, it also decreases the overall detection efficiency of the setup due to the coincidence condition between two scintillation detectors with non-perfect detection-efficiency each. Assuming a muon detection efficiency of 99 %(95 %) for a single scintillation detector, the efficiency for a coincidence setup of two of those scintillators is decreased to only 98 %(90 %).

Due to the mechanical design of the veto detector, other disadvantages occur, such as the scintillation detector's sensitive area not being used efficiently for the coincidence-readout. Those detectors are therefore adding a considerable amount of non-muonic signals to the overall count rate of the veto detector. The veto detectors signal-efficiency is about 74 % at a veto-induced dead time of 1.3 %. Additionally, the mechanical supporting structures require a lot of space close to the lead castle which is not contributing to the sensitive coverage of the solid angle.

The above mentioned effects motivate the upgrade of the cosmic-muon veto detector of the DLB to mitigate drawbacks and increase the detection efficiency as well as the effectiveness of the veto detector. Consequently, an improved veto detector decreases the remaining background level for the gamma ray spectrometry measurements with the HPGe detector, which in turn increases the sensitivity of the DLB. The top module and both lateral modules, alongside the rails for the lead castle's wagon, are replaced with new scintillators and new mechanical support structures.

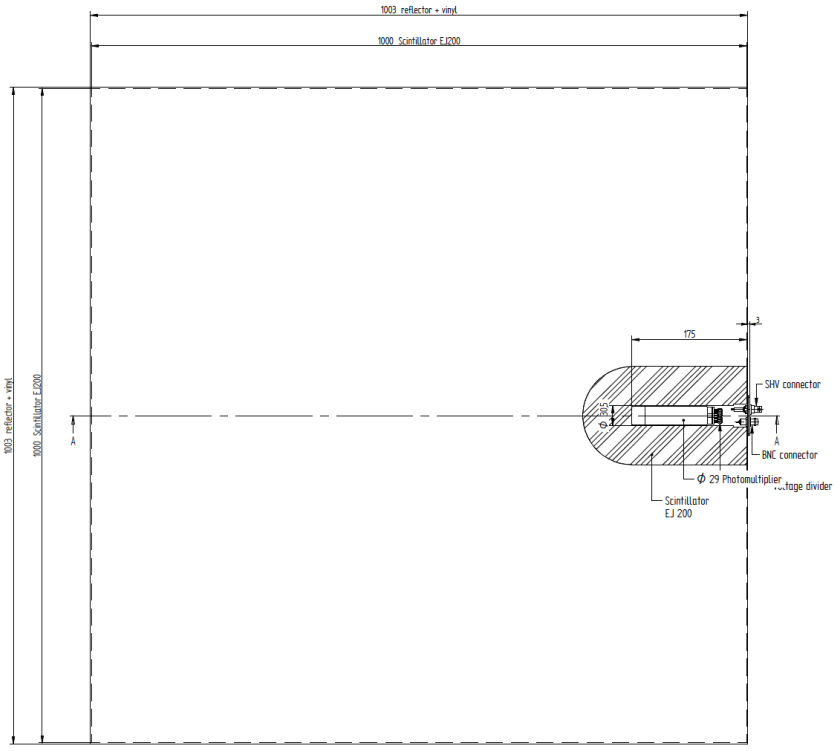

Figure 6.1.: Drawing of the $(1000 \times 1000 \times 50)$ mm^3 scintillator with embedded PMT on the right side [SCI].

6.1. Characterization of the scintillation detectors

Large area plastic scintillation detectors are commercially available. Three detectors are purchased from the manufacturer *SCIONIX HOLLAND BV* [SCI] to replace three modules of the previous muon veto. They have a sensitive area of 1000×1000 mm^2 and a thickness of 50 mm each. The new EJ-200 plastic scintillator from *ELJEN TECHNOLOGY* has a wavelength of maximum emission of 425 nm and a refraction index of 1.58 Its polymer base is polyvinyl-toluene with a density of 1.023 g/cm^3 [ELJ]. Its properties are comparable to the BC-408 that has been used for the DLB before and that is still used for the veto modules covering the remaining two sides around the lead castle. As it can be seen in the drawing in Figure 6.1, the PMT (ET 9900B by *ET Enterprises*) is embedded into the scintillating material with the high voltage connector and the signal output being mounted into an aluminium plate. The PMT provides an enhanced sidewall sensitivity to achieve wide angle light detection of 2π active area on the photo-cathode. Its outer radius is 28.2 mm [ET], which leaves about 10 mm of scintillating material alongside the tube.

The scintillation detector is covered in reflecting foil on the inside as well as black vinyl on the outside to ensure minimal light loss. By embedding the PMT, the setup provides better mechanical stability compared to designs with flanged PMTs on the front face of the scintillator. Although, the latter design is used in several laboratories, e.g. the International Atomic Energy Agency - Marine Environment Laboratory (IAEA-MEL) in Monaco, Monaco [PCLP04] or the Garching Underground Laboratory (GUL) near Munich, Germany [SHM+14]. A crucial parameter of the chosen design is a high light detection efficiency for the entire sensitive area of the detector. The general functionality as well as the detection efficiency of the scintillation detectors are tested and described in the following sections. Scintillators with embedded PMTs are used in other low-level laboratories such as the Institute of Reference Materials and Measurement (IRMM) of the Joint Research Center Geel (JRC-Geel) in Geel, Belgium [HMS+18] or the Low-level laboratory (LLL) at MPI-K in Heidelberg, Germany [HWH+15].

Functionality

Before the scintillation detectors can be integrated into the setup of the DLB, their characteristics are investigated in laboratory studies. Of interest is the general functionality of the scintillator and the PMT as well as the spectra of the background measured in different orientations under consideration of the muon-signal separation efficiency. In the following, the three scintillation detectors will be named *P1-542*, *P2-543* and *P3-544* respectively. All scintillator spectra are recorded using a spectroscopy amplifier and a MCB with 2048 channels. Since the actual energy spectrum is not essential for the usage of the scintillation detectors within the muon veto detector, no energy calibration of the MCB is performed. The spectra are recorded over the timespan of about 20 h each and subsequently scaled to counts/d.

In Figure 6.2 a background spectrum, measured with a single scintillation detector with 5 mm thickness is shown. A description of the instrumentation and measurement setup used for the characterisation of thin scintillation detectors is given by T. Neddermann [Ned09]. Using this detector, no clear separation between muon-induced signals and non-muonic signals is possible. The mean energy deposition of a minimal ionising cosmic muon in plastic scintillators of this thickness is about 1 MeV, which places the signal right into the gamma ray background of the surrounding laboratory which reaches up to about 3 MeV. Since all detectors used, with 5 mm or 50 mm thickness, are wrapped in reflecting foil and black vinyl, the gamma ray component of the environmental background

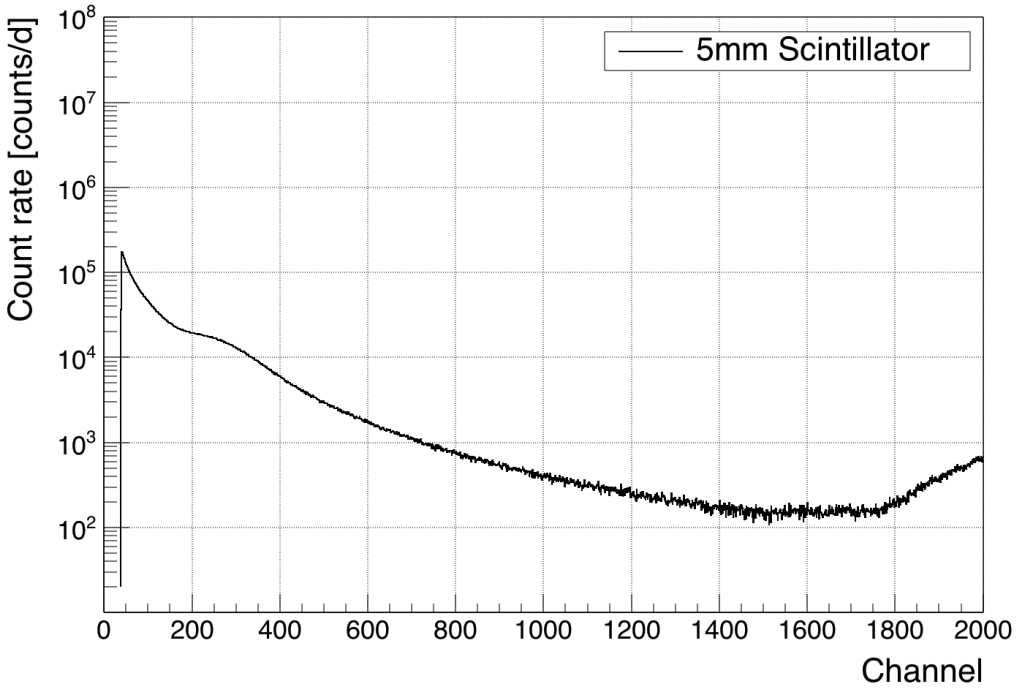

Figure 6.2.: Background spectrum, recorded with a scintillation detector of 5 mm thickness inside the laboratory. No clear seperation between gamma ray or muon-induced signals is visible. The rise of the spectrum above channel 1600 is due to multiple signals inside the scintillation detector piling up.

radiation is dominating.

Figure 6.3 shows a background spectrum recorded with the scintillation detector *P3-544*, which has a thickness of 50 mm and is positioned horizontally. The spectrum is recorded using the same amplifier-gain values as for the thinner scintillation detector discussed before. A clear separation between the mostly gamma-induced background on the left and the muon-induced signals on the right can be seen. The mean energy deposition of a cosmic muon in 50 mm is about 10 MeV, which is about three times more energy then a single gamma ray interaction would deposit.

The energy loss distribution of a cosmic muon penetrating a horizontally oriented detector can in general be described with a Landau distribution, provided the absorber is thin or gaseous [Leo94, Lan44]. This can be used for the 5 mm scintillators and has been shown before, e.g. by the author [Nit14] or T. Neddermann [Ned09].
On the other hand, for a thick absorber the energy loss distribution can be

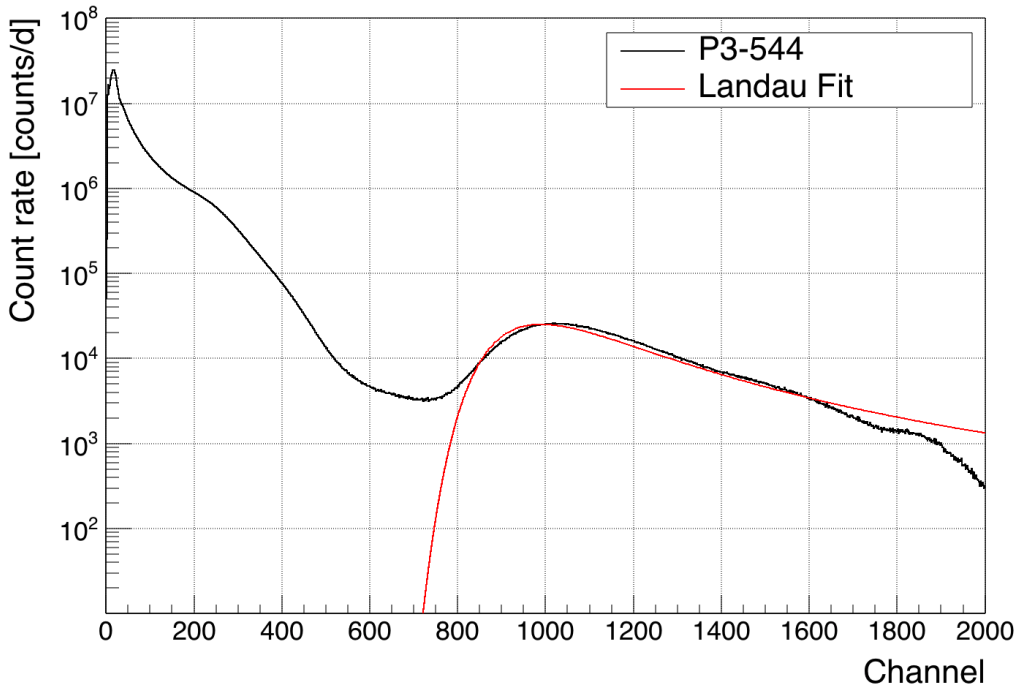

Figure 6.3.: Background spectrum recorded with *P3-544*. The red curve shows a Landau function that is fitted to the recorded spectrum to indicate the muonic energy deposition within the horizontal scintillator.

assumed to be Gaussian shaped, using the central limit theorem [Leo94]. While the 50 mm scintillator is rather thin if used in a horizontal position and the energy deposition can be estimated using a Landau function (see Figure 6.3), this model might not give sufficient results if the scintillator is used in a vertical orientation, where the path for cosmic muons with zenith angle close to $\theta = 0$ is about 1000 mm. However, these long paths are only possible in a rather small solid angle and most muons will penetrate the scintillator for a path length of 50 to 70 mm. Thus, a Landau distribution convoluted with a Gaussian function would provide a more accurate description.

For the horizontally positioned detector shown in Figure 6.3, a simple Landau function is fitted to the histogram and a threshold-channel for the discrimination between muonic and non-muonic signals is determined by the fitted function. For the given example of *P3-544* the threshold is in channel 751, which translates to an amplitude of 1.10 V at the PMT's signal output for the given high voltage that is applied to the PMT. A threshold determined with this technique is ensuring that $\geq 99\,\%$ of the interacting muons are registered by the detector due to

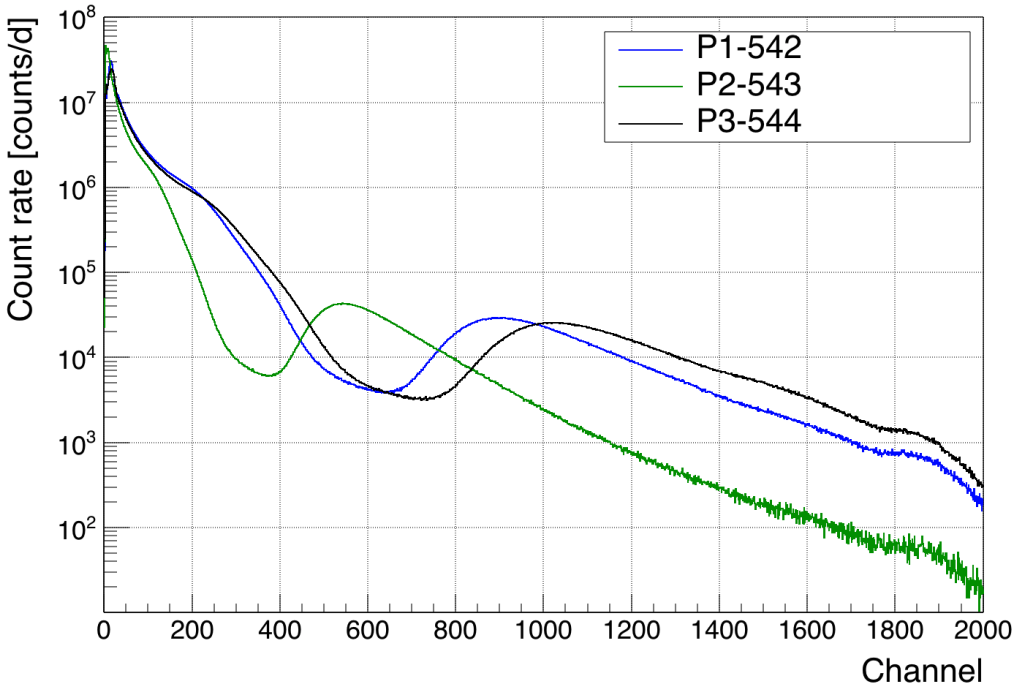

Figure 6.4.: Background spectra of *P1-542* (red), *P2-543* (blue) and *P3-544* (green) respectively. The spectra are recorded in horizontal geometry using the same operating values. All three detectors can be used to distinguish sufficiently between background and muonic energy depositions.

their energy deposition. The PMT output is converted to logical values in NIM standard using discriminator modules.

Analogous measurements with the same horizontal geometry and amplification values are performed for all three scintillation detectors. The spectra are scaled by the measurement time and shown in Figure 6.4. Although all three PMTs are the same model from the same manufacturer and driven with the same operating voltage, there are differences in the extension of the particular spectra which can be caused by different inherent gain factors for each PMT. However, in all three spectra a threshold can be determined to discriminate the background sufficiently. This can be seen in Table 6.1, which gives the individual count rates for the detection of cosmic muons by applying the determined thresholds to the measurements performed in the laboratory.

Since two of the three scintillators will be mounted vertically inside the DLB to cover the lateral sides of the inner shielding, their characteristics are investigated during vertical operation as well. Figure 6.5 shows the difference in the two recorded spectra using *P1-542*. Both measurements are performed successively in

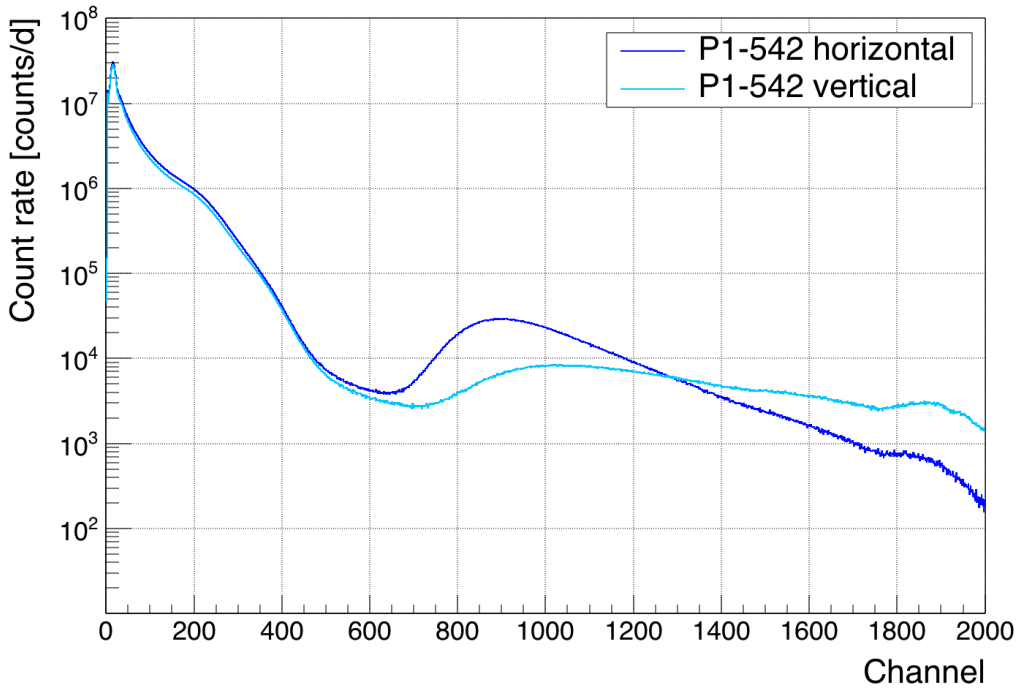

Figure 6.5.: Comparison between horizontal and vertical measurement using *P1-542*. Due to the change in the geometry the mean energy deposition of a cosmic muon is raised in a vertically operated detector.

the same location, resulting in the same non-muonic background component in both spectra, that can be seen up to the channel 500. But due to the change in geometry, the mean path length of the (mostly vertically traveling) cosmic muons within the scintillator is raised from about 50 mm to up to 1000 mm. Therefore, the mean energy deposition of the muons is raised as well and the most probable value of the Landau distribution is shifted to higher channels and higher energies respectively. Another effect of the altered geometry is a decrease of the overall measured muon flux due to the change in the projection of the sensitive area seen by the cosmic muons. The particle flux declines with about $\cos^2(\theta)$ in the zenith angle θ. This decrease in count rate is not observed in the environmental background component, since it is basically isotropically distributed in the laboratory used for the measurements. The decrease in the muon count rate is comparable to previous results using two 5 mm scintillation detectors in coincidence-readout [Ger14].

Table 6.1 gives an overview for the fluxes of cosmic muons measured with scintillation detectors with different thicknesses and orientations. The associated uncertainties are only based on the counting statistics. All measurements took

Table 6.1.: Cosmic muon fluxes for different measurements using scintillation detectors. The measured count rates are given by the integral above the determined threshold-channel, the uncertainty is given by the counting statistics. The uncertainty to the given muon flux incident on the horizontal detector is approximated to 10 %. The muon flux at 2 m.w.e. on a vertical detector is estimated.

	horizontal [counts/(s m^2)]	vertical [counts/(s m^2)]
muon flux (2 m.w.e.) [a]	139.66(1397)	∼70
2×5 mm	141.71(24)	68.26(50)
P1-542	140.34(5)	75.51(4)
P2-543	140.41(5)	74.72(4)
P3-544	140.53(5)	-

[a] Flux is calculated using Equation (3.4) and a muon flux at ground level without any overburden of 146/(m^2 s).

place in the laboratory, which is located on the third floor of the five-story building of the physics department at the TU Dortmund University. Since there are two more floors above the laboratory, the attenuation of the cosmic muon flux has to be considered for the comparison of the given values. The overburden is approximately 2 m.w.e. for zenith angles below 45° due to the concrete floorings of the top floors. This is enough to shield the soft component of the cosmic rays and reduce the nucleonic component considerably (compare Section 3.2.3). Therefore, only muons are considered for the cosmic particle flux inside the laboratory that is able to deposit large amounts of energy inside the plastic scintillators. The cosmic muon flux inside the laboratory is 139.7(140) muons/(m^2 s) crossing a horizontal detector from above. The calculated muon flux for a vertical detector is about 70 muons/(m^2 s) respectively. The uncertainty of the flux for muons incident on a horizontal detector is approximated to 10 %, considering the various influences discussed in Section 3.2.

All of the obtained values for the fluxes presented in Table 6.1, that are measured using a horizontal detection surface, are in agreement with the expected flux for cosmic muons inside the laboratory. If measured with a coincidence setup of two 5 mm scintillators, the measured values are slightly higher. This might be caused by random coincidences in both detectors due to the additional counts

caused by the environmental radiation and the lack of sufficient signal discrimination in contrast to a single scintillator. All three values obtained with 50 mm scintillators are in very good agreement with each other. Due to the improved discrimination capabilities, the non-muonic contribution is very small (well below 1 %), even in the non-shielded laboratory environment. When installed inside the DLB, this contribution becomes even less since the background radiation inside the outer shielding of the DLB is lowered compared to the laboratory's background-level.

The count rates for the vertical operation of the scintillation detector differ slightly more. The increase for the 50 mm scintillators is caused by the non-negligible thickness of the sensitive area, creating about $0.05\,\mathrm{m}^2$ of horizontal detector-surface, resulting in additionally about $7\,\mathrm{counts}/(\mathrm{m}^2\,\mathrm{s})$.

In Section 5.2 the newly implemented MC generator for cosmic muons is described that is mainly used for the estimation of the muonic background component in the background spectrum of the DLBs germanium detector [Ger16]. This generator is used for Geant4 based simulations of the muon induced spectrum in the plastic scintillators as well. Since the MC does not include the emission and transport of scintillation light, the simulation gives only rough estimations for the energy deposition of the cosmic muons inside the sensitive volume of the plastic scintillator.

General agreement between the spectral shapes of the simulated muonic energy deposition and that of the measured spectrum is observed. The overburden of about 2 m.w.e. for the laboratory is considered for the MC simulations, thus giving an estimation of the reduction in muon flux due to the overburden. A flux of $139.530(146)\ \mathrm{muons}/(\mathrm{m}^2\,\mathrm{s})$ is calculated from the integral count rate of the simulated spectrum, which is in good agreement with the values in Table 6.1. Similar results are obtained for vertically positioned scintillators.

Detection efficiency investigation

In contrast to the previously used thin scintillation detectors, the fluorescence light is not collimated and extracted through a light guide for the new 50 mm scintillation detectors. Instead, the sensitive area of the PMT is inserted directly into the scintillator material (see Figure 6.1). The tip of the entrance window for the photo-cathode with an enhanced 2π sensitivity is placed about 155 mm from the outer edge of the scintillator. Consequently, the detection efficiency could be compromised alongside the PMT's base due to an insufficient solid angle or due

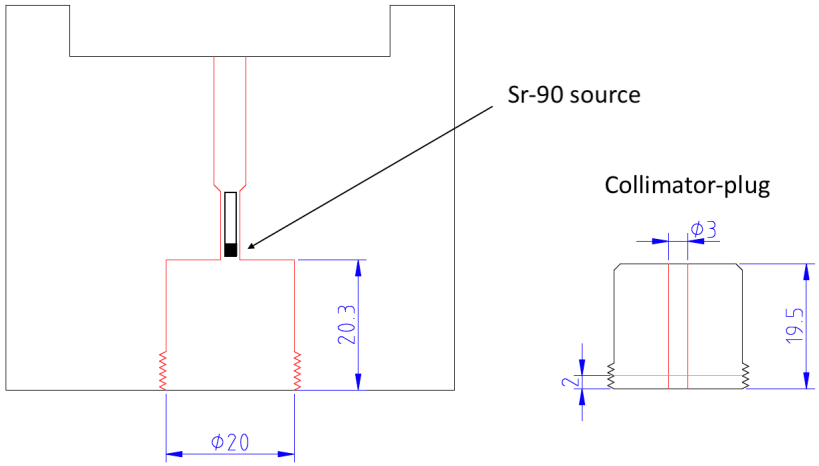

Figure 6.6.: Technical drawing of ^{90}Sr source holder/collimator. On the left is the complete source holder, where the source (10 mm stick with 1 mm ^{90}Sr at the tip) is inserted facing downwards. On the right is the plug with a collimator hole, that is screwed into the holder. All parts are manufactured from PMMA. The distance between source and plastic sctintillator is 20.3 mm when the collimator is placed directly onto the detector surface.

to the thinning of the scintillation material to about 10 mm on each side of the PMT. By mapping the entire area of the scintillation detector with a collimated high-energy beta source, the sensitive area of the detector is investigated for any inefficiencies or 'blind spots'.

For the efficiency-mapping, a strontium-90 (^{90}Sr) source with an activity of 22.3(56) MBq is used. ^{90}Sr decays with a half-life of 28.80(6) a and a Q-value of 545.9 keV via β^- decay into ^{90}Y which subsequently decays with a half-life of 2.67(1) d and a Q-value of 2278.7 keV via another β^- decay to the stable ^{90}Zr [NNDCN18]. Both decays have a probability of 100 % each and no noteworthy gamma rays are emitted during the processes. Due to the much larger half-life of the first decay, both decays are in secular equilibrium.

The point-like source with a diameter of 1 mm is mounted on a cylinder of 10×2 mm size. The cylinder is then installed in a larger PMMA cylinder with the dimensions shown in Figure 6.6. A borehole on the bottom is used to generate a collimated electron-beam. However, the emitted electrons are producing bremsstrahlung inside the PMMA that is surrounding the source. The bremsstrahlung is not collimated. Due to the high activity of the source, the environmental background contribution to the count rates, measured during the irradiation with the ^{90}Sr source, is only between 1.6 % and 4.3 % for the three

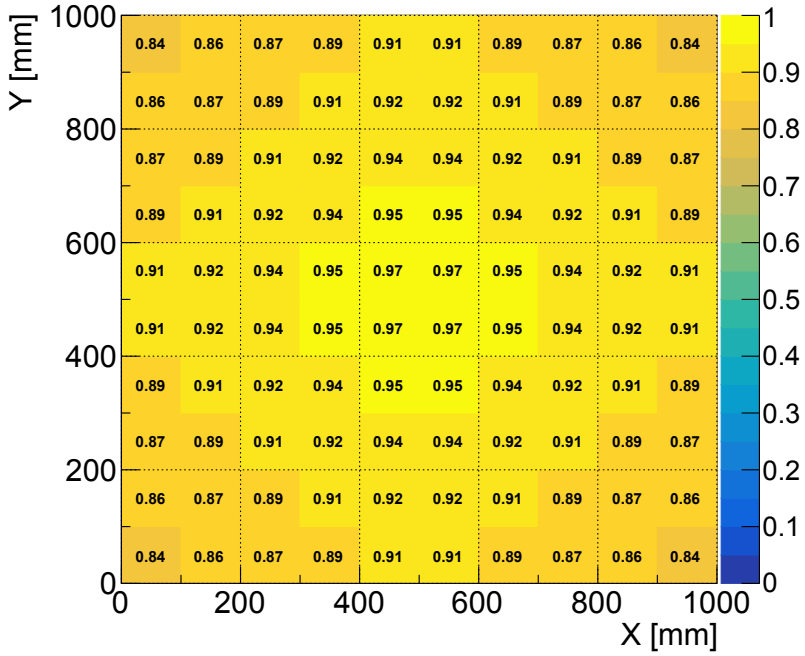

Figure 6.7.: Map of the relative effective solid angle covered by the strontium-90 source for a 1 m×1 m plastic scintillator.

scintillation detectors.

A 10 × 10 pattern of measurement positions is applied to each scintillation detector, beginning 50 mm from the edges. The count rate measured by the scintillation detector is dominated by the bremsstrahlung, which is produced inside the PMMA but not collimated by the source holder. Hence, the solid angle between the source and the plastic scintillator, given by the distance of about 20 mm (compare Figure 6.6) and the size of the sensitive area of the detector, has to be considered when comparing different measurement positions. Figure 6.7 shows a plot of the approximated relative solid angle compared to the hemispherical solid angle for each position.

Figure 6.8, Figure 6.9 and Figure 6.10 show the relative count rate of each measurement position compared to the mean count rate of all measurements for the particular scintillator. The count rates are also corrected for the covered solid angle, according to Figure 6.7. The measurement time per position is between 10 s and 30 s for the three detectors, but constant for each investigated scintillation detector individually.

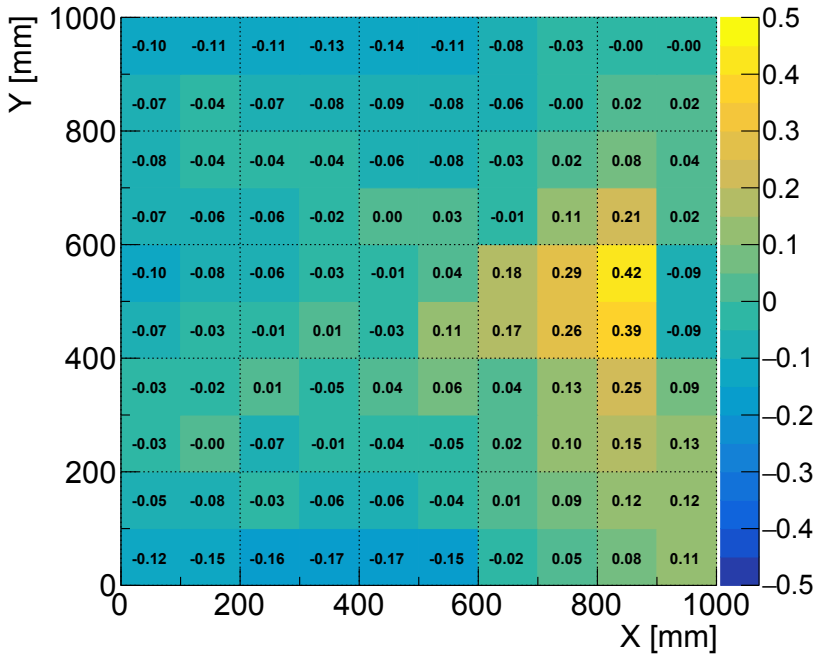

Figure 6.8.: Relative detection-efficiency map of *P1-542*. Shown is the relative deviation of the measured count rate from the mean count rate of the complete detector. The count rates are corrected for the solid angle between source and sensitive area.

The most prominent feature in all three detectors alike is the rise in count rate slightly right of the centre of each scintillator. This increase is caused by the radiation hitting the PMT's photo-cathode either directly or the scintillation material right in front of the entrance window of the PMT, resulting in a particularly high detection efficiency. An analogue behaviour is reported in [Web09] where similar plastic scintillation detectors with embedded PMTs are investigated with collimated gamma rays from a ^{60}Co source. Whereas the pattern is basically the same in the detectors *P1-542* and *P3-544*, where two cells, both about 150 mm from the edge, are showing higher count rates, the increased count rates in the detector *P2-543* is located more to the centre, about 350 mm from the edge.

Another feature that can be observed in all three detectors is the decrease of the relative count rate to the upper and lower edges of the scintillator left of the centre axis. This is most likely caused by geometric effects of the light reflexion on the reflector foil inside the scintillation material and the light collection at the

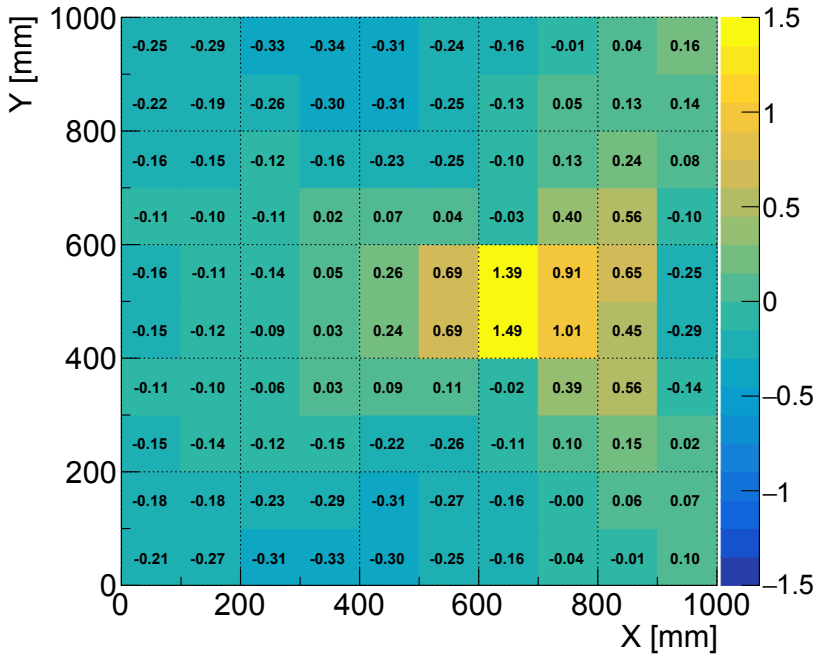

Figure 6.9.: Relative detection-efficiency map of *P2-543*. Shown is the relative deviation of the measured count rate from the mean count rate of the complete detector. The count rates are corrected for the solid angle between source and sensitive area. Note the different scaling on the colored axis.

PMT's photo cathode.

Noticeable is also the wide range in count rates of *P2-543* with $-34\,\%$ to $149\,\%$. The count rate for the other two detectors ranges only between $-17\,\%$ to $42\,\%$ and $-14\,\%$ to $37\,\%$ respectively. *P2-543* is the scintillation detector with the least signal amplification as seen in the background measurements in Figure 6.4. The reasoning for these differences in *P2-543* remain unclear, although a displacement of the PMT compared to the other detectors as well as an inherently different amplification are plausible explanations. However, the usage for the cosmic muon veto detector is not affected by these observations.

Overall, all three scintillation detectors prove to have a sufficiently homogeneous detection efficiency over the entire sensitive area. No 'blind spot' are observed and the detection efficiency is not excessively reduced when hitting the thinner scintillator material alongside the PMT base compared to the rest of the

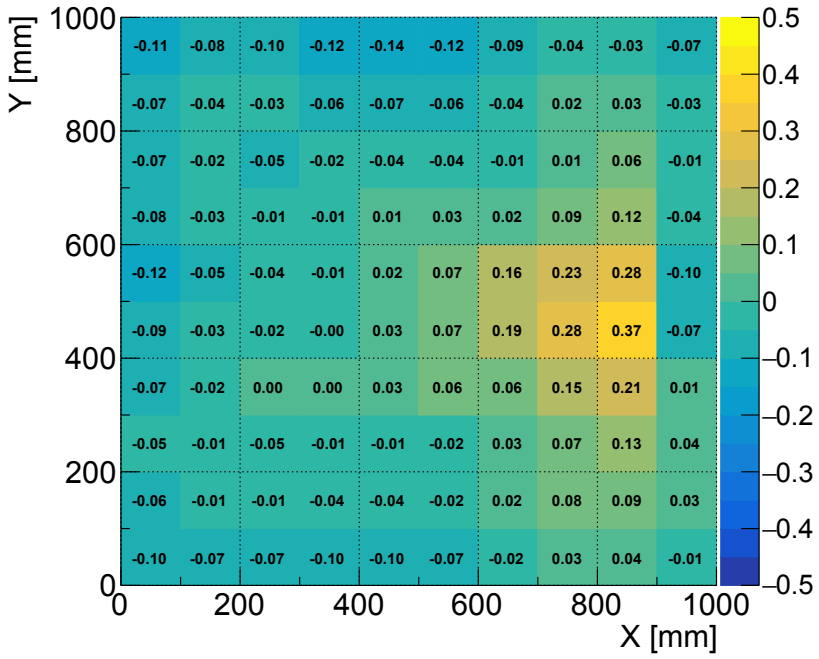

Figure 6.10.: Relative detection-efficiency map of *P3-544*. Shown is the relative deviation of the measured count rate from the mean count rate of the complete detector. The count rates are corrected for the solid angle between source and sensitive area.

sensitive area.

6.2. Integration and commissioning of the muon veto detector

Installation

The mechanical support structures for the integration of the new veto detector-modules are designed with the aim of maximising the covered solid angle for the germanium detector, while keeping the mobility of the lead castle's wagon unchanged. Figure 6.11 shows the three new modules of the muon veto detector after the installation, together with the backside module, that is remaining from the previous detector design. Since the frontside module is installed on the lead castle's wagon, it is not pictured in this photograph.

The top module of the veto detector is laying in a frame, which is hanging

Figure 6.11.: New scintillation detectors integrated into the muon veto detector of the DLB together with the backside that is still consisting of eight scintillators with 5 mm thickness in a interlaced two-layer setup.

from the cast-iron roof of the measuring tunnel above the measurement position of the lead castle. The frame is made from aluminium and mounted on four threaded bars, hanging down 295 mm from the ceiling, placing the underpart of the scintillation detector 1355 mm above the ground and only 10 mm above the lead castle's plug. While the effective area of the top module is basically kept the same during this replacement, the quadratic shape of the new scintillation detector is now matching the quadratic design of the lead castle. This results in a more symmetrical coverage of the solid angle.

Both lateral modules, left and right of the lead castle's rails, are installed on upright standing aluminium frameworks equipped with rolls for convenient handling. Compared to the height above the floor of the germanium detector of 800 mm the previous lateral modules covered an area beginning at about 500 mm. The new modules with a scintillator-height of 1000 mm are installed 350 mm above the floor, increasing the covered zenith angle of the germanium detector in these directions. Since the lead castle's wagon is only 700 mm wide, the side walls can be placed directly underneath the top side of the veto detector and as close as possible to the lead castle. When the lead castle is moved into the measuring position underneath the cast-iron roof, all four lateral modules of the muon veto detector are positioned underneath the top module, creating an overlap that is closing any potential gaps between the different modules of the muon veto detector. The same applies for the left and right-side modules, that are overlapping the frontside and backside modules.

In comparison to the previously installed muon veto detector, the instrumented area is in fact decreased from 3.89 m^2 to 3.71 m^2, or by 4.6 %. However, the sensitive area, which was given before by the area instrumented with two layers of thin scintillation detectors, is actually increased by 17.8 % from only 3.15 m^2 to the complete 3.71 m^2. The design of the previous veto detector was intended to create an partial overlapping of the sensitive area of the thin scintillation detectors [Qua12]. This resulted in areas, especially to the edges of the previous top and side modules, that were only covered by a single scintillation detector. Due to the absence of the coincidence-readout for these detectors, no clear separation between muon-interactions and the non-muonic component was possible and the overall count rate of the veto detector was increased unnecessarily.

For the upgraded muon veto detector, all modules are consisting of sufficiently thick scintillation material or they are instrumented by entirely superposed scin-

tillation detectors in coincidence-readout. A reduction of the overall count rate of the entire veto detector, while maintaining a high detection efficiency for cosmic muons, is increasing the signal efficiency of the veto detector. Thereby, the veto-induced dead time for the germanium detector during measurements with the active muon veto can be reduced considerably.

Figure 6.12 shows the completed muon veto detector with the lead castle at the standard measurement position. The inner shielding is now completely enclosed by the muon veto detector, whereas the top module and both lateral modules are overlapping the frontside and backside modules. Only the frontside module is not reaching to the bottom of the inner shielding, due to the preamplifier and the cooling finger of the liquid nitrogen reservoir (compare Figure 4.3).

Comissioning

The previously determined threshold values for the three scintillation detectors have to be re-determined once the detectors are installed inside the outer shielding of the DLB. Not only does the overburden attenuate the cosmic rays, i.e. cosmic muons and especially the nucleonic components, it also provides a decreased level of environmental radiation compared to the laboratory in which the previous measurements in Section 6.1 took place. The reduction in environmental background inside the DLB is mostly caused by the reduced concentration of airborne radon (see Section 3.1.2 and Section 4.2).

For the determination of a threshold level at the PMT's output signals, the integral count rate of the PMT is measured after a NIM discriminator module in dependence of the applied threshold voltage. When the threshold voltage is increased, the observed count rate drops considerably, which can be interpreted as the maximum energy deposition of the natural radiation which ends at about 2.6 MeV.

Both the obtained threshold voltages and the extracted energy spectra are in agreement with the measurements from the laboratory and show the same differences in amplification for the three PMTs. As indicated in Figure 4.4, the output signals of the PMTs are converted to logical signals in the NIM standard and combined for the gate input of the germanium detector's MCA. For this purpose the described method provides sufficient results and the obtained threshold voltages are applied during all the following gamma spectroscopic measurements with the DLB.

However, the energy spectra of the installed scintillation detectors are recorded

Figure 6.12.: The inner shielding of the DLB at the measuring position underneath the cast iron ceiling. The completely upgraded muon veto detector is installed. Black scintillation detectors are mounted in aluminium support structures. The blue wagon can move the inner shielding alongside the orange rails on the floor. In the foreground is the grey liquid nitrogen reservoir, the yellow inner shielding is not visible due to the coverage of the muon veto.

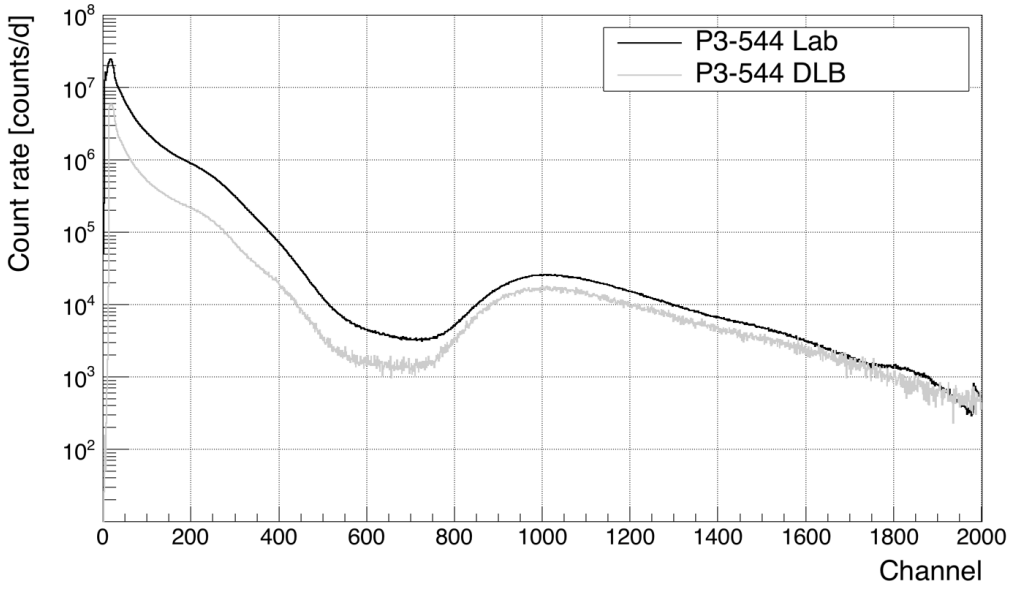

Figure 6.13.: Comparison of background spectra recorded with *P3-544* in the laboratory and inside the outer shielding of the DLB.

using the same readout system consisting of a spectroscopy amplifier and a MCB as in Section 6.1. The recorded spectra are used for qualitative comparison with the laboratory measurements in order to investigate the differences in the background spectra. Additionally, the flux of the cosmic muons inside the outer shielding of the DLB is extracted from the recorded spectra and compared with both laboratory measurements with less overburden as well as flux measurements using the previously determined threshold voltages.

The background spectra are recorded for the horizontally mounted *P3-544* as well as for the vertically mounted *P1-542* and *P2-543*. Figure 6.13 shows the two spectra recorded with the scintillation detector *P3-544*, one inside the laboratory and one inside the DLB's outer shielding. Both spectra are recorded in horizontal position using the same high voltage supplied to the PMT and readout electronics. It is clearly visible that the natural background radiation that is dominating the spectrum up to a channel of 600 is reduced for the spectrum recorded inside the DLB. The scaled integral count rates indicate a reduction factor for the natural background radiation of more than 5. This reduction is partly caused by the reduced radon concentration inside the DLB, that has been discussed before. Additionally, the absence of the soft and hadronic component of cosmic rays can be observed here, because these contributions are not stopped completely by the 2 m.w.e. overburden of the laboratory, but reach negligible

levels inside the DLB's outer shielding of 10 m.w.e..

The typical Landau-shaped peak in the energy spectrum due to muonic energy depositions can be seen above channel 700 for both measurements, with the most probable energy deposition around channel 1000, corresponding to about 10 MeV. Using this value for a rough energy calibration would place the above mentioned end point of the natural background radiation well above 2.6 MeV. This can be explained by multiple simultaneous energy depositions by gamma rays reaching sum energies well above the usual maximum for gamma ray induced background radiation. Considering the volume of 50 l and the large surface area for the used detector, multiple simultaneous energy depositions are very likely.

The cosmic muon flux can again be extracted from the spectra by integration over the Landau-shaped peaks beginning with a pre-determined threshold channel. A value of $140.53(5)\,\mathrm{counts}/(\mathrm{s\,m^2})$ is obtained for the spectrum measured inside the laboratory with 2 m.w.e. overburden and $82.92(52)\,\mathrm{counts}/(\mathrm{s\,m^2})$ for the spectrum measured inside the DLB with 10 m.w.e. overburden. The spectral shape of the muonic energy depositions has not changed, but the measured particle flux is reduced to 59.0 % due to the 8 m.w.e. difference in overburden. In comparison to the cosmic muon flux without overburden ($\sim 146\ \mathrm{muons}/(\mathrm{m^2\,s})$) this gives a reduction to 56.7 %. This is consistent with the reduction factors for cosmic muons from the Reyna/Bugaev approximation and in good agreement with a reduction of about 60 % as stated by Gilmore for this overburden [Gil08]. A comparison for the vertically mounted scintillation detectors gives analogues results for both the reduction of the background radiation and the reduced cosmic muon flux.

Table 6.2 gives an overview of the measured muon fluxes inside the DLB. The values for the flux of cosmic muons incident on the detectors is calculated using the Reyna/Bugaev approximation in Equation (3.4) with the energy-range-relation in Equation (3.6). The flux at ground level outside of the DLB is assumed as $146.3(146)\ \mathrm{muons}/(\mathrm{m^2\,s})$ for the calculations. The associated uncertainty is approximated to 10 % to consider the various influences to the flux of cosmic muons discussed in Section 3.2. MC simulations based on the newly developed cosmic muon generator discussed in Section 5.2 are likewise yielding a count rate of about $78(8)\,\mathrm{counts/s}$ for a $1\,\mathrm{m^2}$ detector in horizontal orientation inside the outer shielding of the DLB.

Table 6.2.: Cosmic muon fluxes for different measurements using scintillation detectors inside the DLB. The fluxes are calculated from the integral above the determined threshold-channel, the uncertainty is given by the counting statistics. The value for the flux of cosmic muons incident on a horizontal detector is calculated using the Reyna/Bugaev approximation in Equation (3.4), the associated uncertainty is approximated to 10 %. The muon flux on a vertical detector is only an estimation.

	horizontal [counts/(s m^2)]	vertical [counts/(s m^2)]
muon flux (10 m.w.e.)	76.1(76)	38
2×5 mm	82.22(38)	50.10(27)
P1-542	-	49.98(3)
P2-543	-	46.56(2)
P3-544	83.42(3)	-

The newly obtained measurement of the flux of cosmic muons inside the outer shielding of the DLB is in good agreement with previously measured values which are obtained with two 5 mm thick plastic scintillators read out in coincidence. However, both measurements yield values that are about 8 % higher than anticipated, although still within the approximated uncertainty. This could be caused by the non-negligible lateral surfaces of the 50 mm scintillators. The areas add up to about 0.2 m^2 that can be considered as a vertically operated detector. If the flux incident on this area is calculated, an additional 7.6 counts/(s m^2) have to be added to the expectation of the measurement, effectively explaining the excess in count rate. However, this does not apply for the measurement with 5 mm scintillators. Here the increase in count rate may be caused by insufficient signal discrimination. Overall, the measurements are in reasonable agreement with the expectations, especially considering the rather large uncertainties.

The expected cosmic muon flux for a vertical detector should only be considered as a rather rough estimation based on experimental experience [Ned09, Nit14]. Since the vertically mounted modules of the veto detector reach down from the cast iron-roof of the measuring tunnel (see Figure 6.11) the effective overburden is less than 10 m.w.e.. The overburden, seen from the position of the germanium detector inside the measuring tunnel, is only above 10 m.w.e. for zenith angles $\theta < 45$, it declines with larger zenith angles and is at least 5 m.w.e. for $\theta > 45$ (compare Figure 4.2). Additionally, the aforementioned effect of the

non-negligible lateral surface of the scintillator has to be considered: About 8 counts/(s m^2) are added to the measured count rate due to the additional surfaces of the scintillation detector. The flux measured with *P1-542* is about 7 % higher than for *P2-543* because *P1-542* is installed on the western side of the lead castle, where the overburden is slightly less massive then towards the eastern direction due to the arrangement of the barite concrete blocks forming the outer shielding of the DLB. This has been observed with the previously installed scintillation detector as well, and an increase of about 8 % is reported in [Nit14].

The values from Table 6.2 for the three new veto detector modules have been determined by recording the background and analysing the spectra. During the routine operation of the DLB, the overall veto signal for the entire muon veto detector is generated by NIM-discriminator units. Using the threshold values with the techniques mentioned above, the measured count rates after the discriminator units should be induced by cosmic muons alone. For all three 50 mm scintillation detectors, the obtained count rates are deviating less than 1 %.

Completion of the cosmic muon veto detector

All three new scintillation detectors are tested for sufficiency of their detection efficiency and integrated into the existing setup of the DLB. The previously obtained count rates for the flux of cosmic muons inside the outer shielding are confirmed, proving the sensitivity of the plastic scintillators. During the upgrade, the instrumented area of the total veto detector is decreased However, the sensitive areas are installed with a better geometric arrangement and are exclusively using either sufficiently thick detector materials or completely superposed coincidently operated scintillation detector. This decreases the overall count rate of the veto detector from about 275 counts/s to about 170 counts/s. Therefore, the veto-induced dead time, that is applied to the germanium detector during spectroscopic measurements where the active muon veto has to be applied, is decreased by about 40 % to only 0.76 % of the measurement time. The signal efficiency of the completed muon veto detector is increased from about 74 % to very close to 100 %. The impact of the upgraded cosmic muon veto detector to the background spectrum of the germanium detector is discussed in the following Section 6.3.

6.3. Background levels using different reduction techniques

Several background spectra with different shielding configurations are recorded with the DLB's germanium detector during the initial construction of the facility and after several upgrades of the system, especially the active muon suppression system. Figure 6.14 shows four of the background spectra that are marking the most important stages of the reduction of the background level.

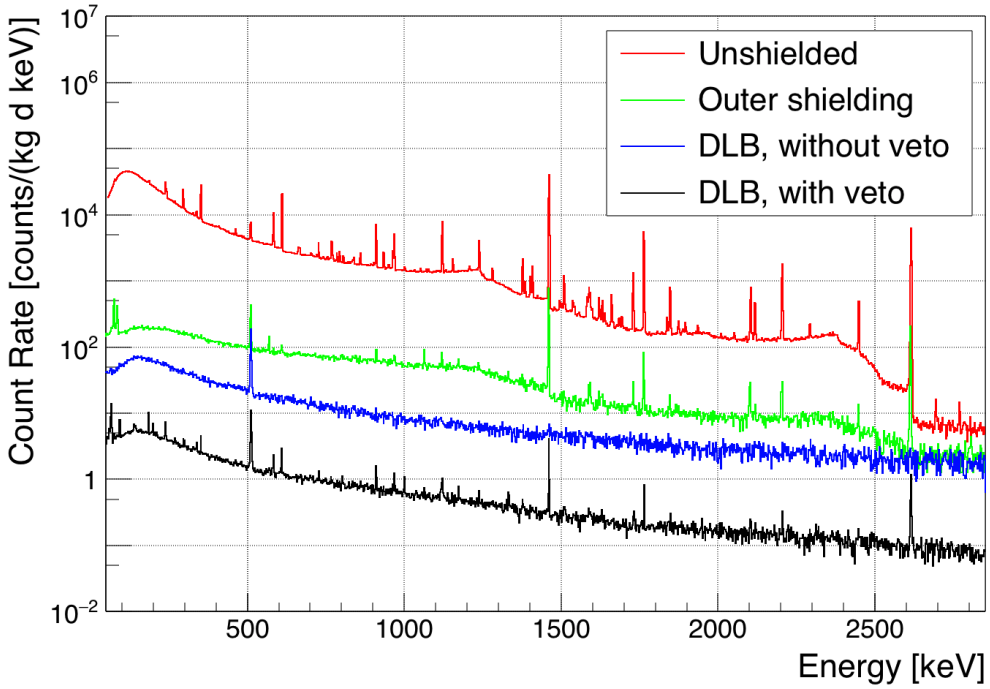

Figure 6.14.: Background spectra from 40 keV to 2850 keV for different shielding configurations of the DLB. Shown are the spectra for unshielded conditions (red line), with an overburden of 10 m.w.e. and a temporary lead shield of 50 mm thickness (green line), with completed passive shielding, but without any active background reduction (blue line) and the current passive shielding with active muon veto applied (black line).

The spectrum with the highest count rate (see Figure 6.14, red line) shows a measurement of the natural background radiation inside the laboratory. No shielding was placed around the detector for this measurement, which was performed before the set up of the DLB by H. Gastrich [Gas09]. Clearly visible are a large number of peaks corresponding to the decay chains of ^{238}U, ^{235}U and ^{232}Th and their respective daughters as well as ^{40}K, all originating from the natural background radiation inside the laboratory.

The second highest spectrum (see Figure 6.14, green line) was recorded by T. Neddermann during the construction of the DLB [Ned14]. It shows the background level of the germanium detector with the outer shielding installed, but only with a temporary lead shielding of 50 mm thickness surrounding the detector, where the inner shielding is constructed now. While the overall background is already suppressed by about two orders of magnitude, and many peaks are strongly reduced, some peaks, especially from ^{40}K and the ^{232}Th decay chain, remain visible in the spectrum. For the 1460.8 keV line of ^{40}K or the 2614.5 keV line of ^{208}Tl (^{232}Th decay chain), the Compton edges are still visible. The source for these contributions to the spectrum is probably the sand-lime brick used for the supporting walls of the cast iron block above the measuring tunnel (see Section 4.1). Assuming, that events with more than 2700 keV can only be caused by cosmic radiation, the impact of the outer shielding can already be seen in this energy region.

For the measurement of the third highest spectrum (see Figure 6.14, blue line), the final setup of the DLB was used, including the current outer shielding and inner shielding, i.e. the passive shielding techniques. Since the muon veto detector was not applied during the measurement, the spectrum is basically consisting of a continuum with a superposed 511 keV line. This indicates a domination of muon interactions and muon-induced showers of secondary particles, such as gamma-rays, electrons and positrons and neutrons (see Section 3.2.2). Due to the strong domination of the muon-induced events, the relatively short measurement time for this configuration and the choice of binning for the background spectrum presented here, no more clear peaks a observable. However, peaks are at the aforementioned energies of 1461 keV and 2615 keV. Additional peaks are found at about 66.7 keV due to the cosmogenic activation of the germanium crystal and at 93.6 keV from a summation of two emissions from ^{234}Th (^{238}U decay chain). The discussion of the MC simulation of the muon-induced background components in Section 5.2 already gives a hint at an additional non-muonic component of about 4 % in the background spectrum with this configuration. The origin and composition of the non-muonic component is discussed in Section 7.2.

The currently reached background level with the passive shielding techniques as well as the completed muon veto applied is shown in the fourth and lowest spectrum in Figure 6.14 (black line). During summer and fall of 2017, a dedicated measurement of the background was performed with a lifetime of 92.7 d. Applying the muon veto to the gate input of the MCB is considerably reducing the above-mentioned muon-induced events of the background spectrum. A re-

duction of the spectrum's continuum of more than one order of magnitude can be seen. This reduction is extending seamlessly to the energy region above 2700 keV, where only muons can be assumed to contribute the observed spectrum. The 511 keV line is suppressed with a factor of 20.5 By lowering the background level by more than one order of magnitude, many peaks become visible in the spectrum. Although these are caused by many of the same nuclides or decay chains that dominated the less-reduced background spectra, sources for these differ. Most of the lines are stemming from impurities of the setup itself, e.g. supporting structures in close proximity to the detector, shielding materials such as the innermost lead layers, the copper or the aluminium detector end cap, or even impurities of the germanium crystal itself. Additionally, lines emerge from the cosmogenic activation of the aforementioned parts of the setup (see Section 3.2.4).

Table 6.3.: Integral count rates between 40 keV and 2700 keV for background spectra recorded under different shielding configurations of the DLB. The count rates are normalised to the sensitive mass of the germanium crystal.

Stage	Integral count rate 40 keV to 2700 keV [counts/(kg min)]	Integral count rate 40 keV to 2700 keV [10^3counts/(kg d)]
Unshielded	7681.4(13)	11 061.2(17)
Outer shielding	101.95(18)	146.80(25)
DLB without veto	23.538(44)	33.895(63)
DLB with veto	1.8554(27)	2.6718(39)

The integral background count rates shown in Table 6.3 are corresponding to the background spectra shown in Figure 6.14. All reported count rates are calculated by integration of the measured background spectrum in the reference energy interval from 40 keV to 2700 keV. They are scaled with the lifetime of the measurement and normalised to the germanium detector's sensitive mass in order to enable the comparison of the numbers with other facilities which may use germanium crystals of other sizes.

The impact of the outer shielding can clearly be seen in the suppression by a factor of about 75, keeping in mind that an additional layer of 50 mm of lead was used for the measurement labeled 'Outer shielding'. Another factor of 4.3 in reduction is reached by utilising the multi-layered inner shielding (see Section 4.3), adding up to a factor of 326 for the background reduction of the passive shielding techniques. The background level with this con-

figuration is strongly dominated by direct and indirect events that are induced by cosmic muons penetrating the setup. A comparison of the integral background count rate of $23.54(4)\,\mathrm{counts}/(\mathrm{kg_{Ge}min})$ for the DLB can be made for example with $21.67(3)\,\mathrm{counts}/(\mathrm{kg_{Ge}min})$ obtained with the Germanium Inner Outer Veto (GIOVE) detector at the shallow underground (15 m.w.e.) laboratory of the Max-Planck-Institute für Kernphysik in Heidelberg, Germany [HWH+15]. The discrepancy of about $1.9\,\mathrm{counts}/(\mathrm{kg_{Ge}min})$ is supporting the aforementioned assumption of a non-muonic contribution to the background spectrum, that is also indicated by the MC simulations of the muonic background component, discussed in Section 5.2. Another comparable facility is the GUL with an overburden of 10 m.w.e.. The reported integral count rate for this system is $21.18\,\mathrm{counts}/(\mathrm{kg_{Ge}min})$, which compares under the same circumstances to the value of the DLB [SHM+14].

Adding the active muon veto to the background suppression systems reduces the background count rate by another factor of 12.7. This is in good agreement with the reduction factor of 15 for active suppression systems used in facilities with overburdens of 10 to 20 mwe as stated by Theodorsson [The96] and even higher than the factor of 4 to 10 that is achievable for above ground systems given by Gilmore [Gil08].

In comparison with other shallow underground facilities, similar factors have been reported for systems of the same generation as the DLB. The Corrado detector achieved a reduction factor of 10 [B+07], while inside the IAEA-MEL a background reduction factor of 8 was reported [PCLP04]. For systems of the newest generation, where screening measurements of the construction materials are conducted in order to minimise any contamination and thereby the non-muonic component of the background spectrum, even larger veto factors have been achieved. A factor of 17 is reported for the detector of the GUL [SHM+14] and an impressive factor of 89 has been achieved for the GIOVE spectrometer at the MPI-K in Heidelberg, Germany [HWH+15]. The impact of the muon veto for laboratories with more than 100 m.w.e. is decreasing but still useful [HMS+18]. An intercomparison with other facilities can be found at the end of this section in Table 6.5.

Finally, the overall reduction of the background level for the DLB can be stated with a factor of 4146. For a particular sample matrix and measurement time, the sensitivity of the system is given by Equation (2.13). Due to the lowered background level, the sensitivity of the spectrometer is increased by more than a factor of 60.

Upgrades of the cosmic muon veto detector

Table 6.4.: Integral background count rates between 40 keV and 2700 keV and net count rates of the 511 keV peak for different configurations of the active muon veto detector. The integral count rates are normalised to the sensitive mass of the germanium crystal.

Stage	Integral count rate from 40 keV to 2700 keV [counts/(kg min)]	Net count rate 511 keV peak [counts/d]
DLB 5 mm veto, initial setup [a]	4.0599(87)	107.4(220)
DLB 5 mm veto, full setup [b]	2.0120(40)	38.12(85)
DLB 50 mm veto	1.8554(27)	34.16(68)

[a] [Ned14]
[b] [NGGK17]

Several upgrades to the active muon veto detector of the DLB have been carried out over past years (see e.g. [Qua12, Nit14, Ger16]) since its initial installation in 2009 by T. Neddermann [Ned09, Ned14]. All of the upgrades involve the author directly or by supervision. Table 6.4 provides the most significant stages in upgrading the configuration of the muon veto detector. In addition to the integral background count rate, with similar calculation as before, the net counts of the peak at 511 keV are given in counts per day (counts/d).

Efficiency estimation for the cosmic muon veto detector

T. Neddermann predicts that upgrading the muon veto detector could lead to a reduction of the background count rate by a factor of two. The overall reduction excels this prediction with a factor of 2.2 between 4.059(9) counts/(kg_{Ge}min) and 1.855(3) counts/(kg_{Ge}min). Theodorsson gives a reduction factor of 20 for the 511 keV annihilation line with active suppression systems, which is achieved by a factor of 19.8 for the DLB [The96].

Based on the approximated veto-efficiency of 89 % for the initial setup of the muon veto detector given by T. Neddermann [Ned09], the potentially achievable background count rate for a veto detector with 100 % efficiency was extrapolated to a value of 1.608 counts/(kg_{Ge}min) [Nit14]. Using this estimation, the final state of the muon veto detector has an efficiency of about 98.9 %. This value probably overestimates the veto-efficiency, since a non-negligible remaining muon

contribution is evident. Since environmental gamma radiation is basically not present with energies higher than the 2614.5 keV line of ^{208}Tl (^{232}Th decay chain), the count rate should drop off above this peak towards higher energies in the background spectrum. This has been observed in ultra-low-background spectra recorded in deep underground facilities, where cosmic muons have negligible influence [HWH+15]. Since this drop off can not be observed, the muon-induced contributions to the spectrum are most likely more than 15 % and the veto-efficiency is less than stated above.

Alternatively, the veto-efficiency of the completed cosmic muon veto detector can be estimated based on the MC simulations of the muonic background component discussed in Section 5.2. The MC simulation results in a muon-induced background count rate of about 22.5 counts/(kg_{Ge}min), while the measured background count rate with no cosmic muon veto applied yields about 23.5 counts/(kg_{Ge}min). Thereby the veto-efficiency is calculated to 96.5 % for the currently remaining background count rate of 1.855(3) counts/(kg_{Ge}min). A remaining contribution of about 57.7 % due to muon-induced events is calculated consequently.

Another method based on the MC simulations can be used for the determination of the veto-efficiency. It is based on the assumption that entries in the background spectrum with energy depositions between 2650 keV to 2750 keV are only caused by direct or indirect muon interactions. Unsuppressed muon-induced energy depositions in the germanium detector will result in the same spectral shape as the simulated spectrum in Figure 5.2.
The MC generated spectrum is therefore scaled to the energy region of 50 keV around 2700 keV to estimate the underlying spectrum induced by cosmic muons. A count rate of 0.937(4) counts/(kg_{Ge}min) between 40 keV and 2700 keV is obtained, resulting in a contribution of about 50.5 % and a veto-efficiency of 95.8 %. This method gives general agreement with the MC-predictions for the background spectrum without applied muon veto, especially if the systematic uncertainties are considered, that are discussed in Section 5.2.

The current setup of the cosmic muon veto detector covers most of the solid angle for the upper hemisphere around the centre of the germanium detector. For three of the lateral detector modules, zenith angles are covered below the horizon. Both side modules cover zenith angles up to θ =139.5° while the backside module reaches up to θ =104.9°. Only the frontside module is not reaching down to the horizon, but up to θ =57.7°, due to the germanium detectors pre-amplifier and the detector arm that is connecting the end cap inside the inner shielding with the

nitrogen reservoir next to the lead castle. The coverage of the solid angle for the given veto module-geometry can be determined by integration of the flux of the cosmic muons inside the outer shielding of the DLB over the upper hemisphere. A solid angle coverage of 90.5 % can be calculated for the aforementioned zenith angles. However, this only gives a lower limit for the veto-efficiency, since this calculation does not take into account the possibility of a detection in one of the veto modules for the outgoing muon after the penetration of the inner shielding. Additionally, only the upper hemisphere is taken into account here and any cosmic muons penetrating the setup from angles below the horizon are neglected, even though those angles are in principle possible and secondary particles can enter the setup due to backscatter from below the setup.

Based on the calculations presented here, the veto-efficiency for the described setup of the cosmic muon veto detector is estimated with 96 %. Since this number leaves room for improvement, which was also indicated by the MC simulations of the muon-induced background component in the remaining background level, the potential for a final upgrade of the current setup is discussed here briefly.

Potential for further improvement of the cosmic muon veto detector

Especially important and most useful for a potential upgrade is the closure of the remaining solid angle of the upper hemisphere towards the frontside. Due to the detector arm, that is reaching inside the inner shielding, a complete closure of this opening is not possible. However, a minimisation of the uncovered area is possible with a custom made plastic scintillator that passes by the cooling finger, or even around it. A 'horseshoe' shaped scintillator, read out by two PMTs at the bottom end would be conceivable for example. Based on the background reduction achieved by the backside module (reduction of about 1.18 counts/($\mathrm{kg_{Ge}}$min)) in comparison with the so far accomplished reduction due to the frontside module (reduction of 0.52 counts/($\mathrm{kg_{Ge}}$min)), a potential reduction of up to 0.66 counts/($\mathrm{kg_{Ge}}$min) would be achievable. Although this estimation is plausible due to the geometric symmetry of the veto detector, a potential reduction of only 0.3 counts/($\mathrm{kg_{Ge}}$min) is probably more realistic due to the necessary opening for the cooling finger.

Additional potential for reduction seems to be possible with the addition of a sixth veto detector module underneath the lead castle. Even though practically no cosmic muons are penetrating the setup from zenith angles larger than $\theta = 90°$, backscatter of secondary particles may occur and lead to a contribution to

the background spectrum of the germanium detector. A reduction in background count rate of up to 1 % is estimated by Theodorsson for a low-level setup at the Max-Planck-Institute für Kernphysik in Heidelberg, Germany [The96]. For the background composition of the DLB this would translate to a reduction in background count rate of about 0.2 counts/(kg_{Ge}min). Since most of the cosmic muon veto detectors utilised in comparable low-background facilities are not employing these technique, there are no reliable documentations of the potential benefits of a veto detector module installed underneath the inner shielding. However, the newest low-level setup at the Max-Planck-Institute für Kernphysik in Heidelberg, (GIOVE [HWH+15]) does use a two-stage cosmic muon veto, where at least on stage is utilising a plastic scintillator that is integrated into the inner shielding and placed underneath the germanium detector.

Finally, the cosmic muon veto would benefit from the replacement of the remaining 5 mm plastic scintillators in parts of the veto detector. Since the geometry and angular coverage changed as well when the top module and both lateral side modules where replaced with 50 mm scintillators, the reduction in the background count rate of 8 % may not be entirely due to the replacement. However, the better signal discrimination does at least lead to a better signal efficiency of the veto detector, which in turn leads to a drastic decrease of the veto-induced dead time of the germanium detector during measurement.

Combining the aforementioned upgrade possibilities would enable a potential background reduction of probably more than 0.5 counts/(kg_{Ge}min), resulting in a background level of less then 1.35 counts/(kg_{Ge}min) for the germanium detector. This value is not in conflict with the MC based estimations for the non-muonic background component of between 0.92 counts/(kg_{Ge}min) and 1.07 counts/(kg_{Ge}min) discussed above, leaving the remaining part induced by muons due to the opening of the cooling finger. A reduction of the background level by another 25 % would, however, only increase the sensitivity of the detector system by about 13 % for a given sample-detector geometry and measurement time.

A reduction below this value is not possible without major changes to the setup, which is not economically reasonable. However, the components of this lower boundary for the background level given by the contaminations of the germanium detector and the shielding material are discussed in the following Section 7.1.

Laboratory intercomparison

The obtained results for the residual background levels and reduction factors due to the different techniques employed can be compared to other low-level gamma ray spectrometry laboratories. In Table 6.5 some key values for several low-level facilities with shallow overburden (<100 m.w.e.) are presented. Additionally, the table gives reference values for two underground laboratories with a overburden around 560 m.w.e. and two deep underground facilities that are currently marking the state-of-the-art in low-level gamma-ray spectrometry with 3800 and 4800 m.w.e. overburden respectively. The background index from 40 keV to 2700 keV for each detector system is normalised to the germanium detector's sensitive mass.

The background level reached with the DLB is comparable to other facilities with overburdens between 10 m.w.e. and 110 m.w.e.. Impressive results are achieved for the detectors of the IAEA-MEL and the GIOVE detector where construction material screening and active muon suppression techniques are combined to reach about an order of magnitude more background reduction. The Felsenkeller, that is covered by an overburden of 110 m.w.e., about one order of magnitude more than the DLB, is not using an active muon veto in its facility and reaches nearly the same background level. Another factor of 2 is estimated for the potential additional background reduction if active techniques would be applied [KDL+09].

Laboratories around 500 m.w.e. are reaching residual backgrounds about an order of magnitude lower than the DLB. Muon veto detectors are still useful at these depths, though the muon-induced activation processes of the detector and shielding material become less problematic here. Deep underground laboratories are even reaching background levels nearly two orders of magnitude lower than shallow underground facilities. Cosmic muons are negligible at these depths and accompanying activation processes are only problematic if detector or shielding components are exposed to cosmic rays prior to installation underground, e.g. during production of storage. Material screenings of detector and shielding material are mandatory to reach these sensitivity levels [Lau17, LBP+15].

Table 6.5.: Comparison of the integral background count rate in the range of 40 keV to 2700 keV for several gamma ray spectrometry laboratories in Europe. The count rate is normalized to the germanium crystal mass and minute.

Laboratory / Detector	Institute (Location)	Depth [m.w.e.]	Integral count rate 40 keV to 2700 keV [counts/(kg min)]	Veto factor	References
DLB	TU Dortmund (Dortmund, Germany)	10	1.855(3)	12.7	This work
GUL	TU Munich (Garching, Germany)	10 - 15	1.201(4)	17.6	[SHM+14]
CORRADO	MPI-K (Heidelberg, Germany)	15	2.542(8)	10	[B+07, HWH+15]
GIOVE	MPI-K (Heidelberg, Germany)	15	0.242(2)	88.6	[HWH+15]
USL16	PNNL (Washington, USA)	30	1.278	-	[GCB+17]
CAVE	IAEA-MEL (Monaco, Monaco)	35	0.58	8.3	[PCLP04]
Felsenkeller	VKTA (Dresden, Germany)	110	2.04	3 [a]	[KDL+09]
Ge-3 HADES	JRC-IRMM (Geel, Belgium)	500	0.174(1)	-	[HCK+00, HMS+18]
Ge-14 HADES	JRC-IRMM (Geel, Belgium)	500	0.162(2)	1.15	[HMS+18]
GeMSE	ALU Freiburg (Neuchatel, Switzerland)	620	0.0854(7)	1.20	[vSHRS16]
Gator	LNGS (Assergi, Italy)	3800	0.0714(4)	-	[BFA+11]
GeMPI	LNGS (Assergi, Italy)	3800	0.0458(7)	-	[HLN06, HWH+15]
Obelix	LSCE (Mondane, France)	4800	0.0507	-	[LBP+15]

[a] Estimation from [KDL+09]. There is no veto detector used in this facility so far.

7. Low-Background Performance

In this chapter the residual background spectrum is characterised. The net count rates and potential origins for the peaks visible in the background spectrum are discussed. Thereby, special attention is on the peaks induced by radionuclides that are produced by cosmogenic activation from the residual cosmic radiation inside the DLB. Additionally, MC simulations are employed for the estimation of the components, that are resulting in the residual background. Finally, examples are given for radiopurity screening measurements performed with the DLB, that are enabled by the low-background environment achieved by the passive and active reduction techniques discussed in Chapter 4.

7.1. Background spectrum characteristics

Figure 7.1 shows the residual background spectrum of the DLB. The spectrum was recorded over a time period of four month during summer and early fall of 2017, resulting in a lifetime of 2224.3 h.

The remarkably low-background level is achieved when the currently installed active muon veto is applied to the measurement, reducing the background by another factor of 12.7. This reduction of the muonic component lets more peaks become visible in the spectrum again, compared to the background achieved only with passive shielding techniques. Most of these peaks are induced by the gamma rays of remaining intrinsic contaminations in the detector materials and shielding components or caused by cosmogenic activation of the same.

Due to the massive inner shielding (compare Figure 4.3), external environmental radiation is reduced to negligible levels. Even high energetic gamma rays of 2.6 MeV, where the attenuation is weaker, are reduced by about a factor 1×10^5. H. Rullkötter obtains similar results by using a simplified model of the DLB shielding design for MC studies of the shielding capabilities for different components [Rul18].

The spectrum's underlying continuum, that is peaking at around 150 keV,

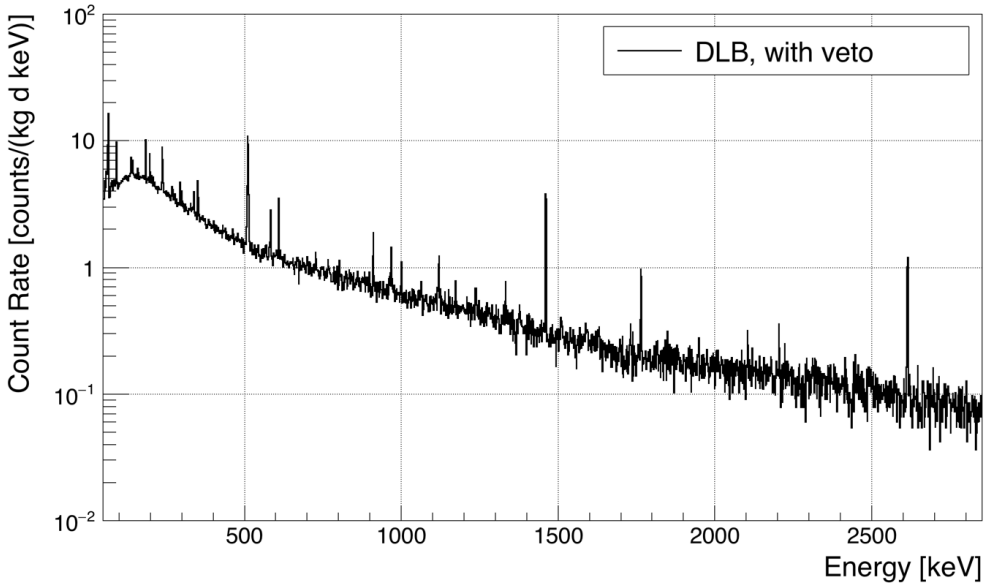

Figure 7.1.: Background spectrum of the DLB with active muon veto detector. Measurement performed in 2017 with an effective lifetime of 2224.3 h. The count rate is scaled to the sensitive detector mass of 1.247 kg.

is caused by Compton scattering of these gamma rays as well as residual muon-induced events. The count rate drops below 1 counts/(kg keV) above approximately 700 keV and becomes less then 0.1 counts/(kg keV) (or 1 counts/(kg keV) in ten days) above 2600 keV.

By far the most intense peak in the spectrum is the 511 keV annihilation peak with about 35 counts/d net count rate. This line is caused by photons produced by annihilating positrons, which can originate from the decay of decelerated cosmic muons, or beta plus decaying radionuclides. Other prominent lines are caused by cosmogenic activation (66.7 keV (^{73m}Ge)) or by naturally occurring radionuclides (92.6 keV (^{234}Th), 238.2 keV (^{212}Pb), 1460.8 keV (^{40}K)).

In addition to those peaks clearly visible in the background spectrum, several gamma ray energies are investigated due to the literature reporting about commonly found gamma lines in low-level gamma spectrometry experiments [Bos05, Ned14, Gil08, Heu93]. A list containing the investigated peaks in the spectrum can be found in Table B.1 in Appendix B. Upper limits with 95 % confidence level are calculated, in case no counts exceeding the DT are found (see Section 2.2.4). Otherwise, a net count rate is given in counts per day, calculated according to the DIN ISO 11929:2011 analysis-standard using the `GeAna` software (see Section 4.7).

7.1.1. Shielding contaminations and radioimpurities

It was already discussed in Section 6.3 that cosmic muons probably contribute about 50 to 58 % of the residual background spectrum, mostly by inducing to the broad continuum and the 511 keV annihilation line. Additionally, radioimpurities and contaminations within the shielding and construction materials in the close vicinity of the detector are contributing largely to the detector background. These contributions are especially crucial for spectrometer, that are covered by a considerable overburden or operated deep underground, where cosmic background contributions are usually negligible. Therefore knowledge about the origin of these peaks is always helpful.

Table 7.1 gives an overview of several peaks found in the residual background spectrum that are associated with radioimpurities of the detector system. The table only gives the most intense lines, a more extensive list of all peaks is given in Appendix B.

The majority of peaks, belonging to ^{222}Rn and ^{220}Rn and their decay products in the ^{238}U and ^{232}Th decay chains, respectively, yield net count rates exceeding the DTs. While ^{40}K can clearly be identified due to its 1460.8 keV gamma ray, for most of the lines coming from the ^{235}U decay chain, only upper limits can be determined for the net count rates.

Since the germanium crystal is fairly radiopure [Gil08], these radioactive contaminations have to be located in the shielding material or detector support structures. This underlines the importance of selecting radiopure materials and conducting screening campaigns of construction materials to minimise their background contributions. To some extend, it is possible to estimated potential locations and distances from the detector crystal based on the measured count rates. Low-energetic gamma rays are relatively short-ranged and can therefore point to locations very close to the germanium crystal. When count rates of peaks from the same decay series are compared, the energy-dependent FEP detection efficiency has to be considered as well as the emission probability of the particular gamma ray.

Table 7.1.: Primordial and antrophogenic radioimpurities found in the residual background spectrum. Measurement of 2224.3 h background recorded with the DLB in 2017. Upper Limits given with 95 % CL.

Decay chain	Nuclide	Peak energy [keV]	Intensity [%]	Net count rate [counts/d]
^{238}U	^{234}Th	92.59[a]	4.33	16.05(64)
	^{234m}Pa	1001.03	0.84	1.58(24)
	^{226}Ra	186.21	3.59	15.64(63)
	^{214}Pb	351.93	37.6	5.84(42)
	^{214}Pb	295.22	19.3	2.86(39)
	^{214}Bi	609.31	46.1	5.46(36)
	^{214}Bi	1764.49	15.4	2.84(29)
	^{214}Bi	1120.29	15.1	2.25(26)
	^{210}Pb	46.54	4.25	8.28(49)
^{235}U	^{235}U	163.36	5.1	<1.2
	^{235}U	205.32	5.0	1.20(38)
	^{231}Pa	283.69	1.7	<0.55
	^{227}Th	235.97	7.0	0.98(39)
	^{223}Ra	323.87	3.9	<0.68
	^{219}Rn	401.81	6.4	0.51(25)
	^{211}Pb	404.75	3.8	<0.52
^{232}Th	^{228}Ac	911.20	25.8	3.70(29)
	^{228}Ac	968.97	15.8	1.59(26)
	^{228}Ac	338.32	11.3	2.42(33)
	^{212}Pb	238.63	43.3	12.16(75)
	^{212}Bi	727.33	6.6	1.26(22)
	^{212}Bi	1620.50	1.5	<0.297
	^{208}Tl	583.19	84.5	3.56(34)
	^{208}Tl	860.56	12.4	0.39(18)
	^{208}Tl	2614.53	99.16	4.58(25)
	^{40}K	1460.82	10.5	12.83(41)
	^{60}Co	1173.23	99.8	0.97(21)
	^{60}Co	1332.49	99.9	1.15(21)
	^{137}Cs	661.6	85.0	<0.61

[a] Sum peak of 92.38 keV (2.18 %) and 92.8 keV (2.15 %), both from ^{234}Th

The upper part of the ^{238}U is identified in the background spectrum by the peaks from ^{234}Th and ^{234m}Pa, with net count rates indicating an activity 10 to 20 times higher than the radon-progenies from the same decay series. This can for example be caused by the evaporation of gaseous radon from the contaminated materials or chemical contaminations, where only parts of the decay series are abundant in the material. M. Hult et al. present results of radiopurity screening measurements with factors of 16 or 0.02 found for the activities of the upper and lower part of the ^{238}U decay series in capacitor units and high voltage contact samples [HMS$^+$18].

The low energetic lines from ^{234}Th (92.4 keV and 92.8 keV) as well as ^{210}Pb (46.5 keV) are strongly evident in the background spectrum. Due to the week penetration power of these gamma rays, their sources have to be located in the very close vicinity of the germanium crystal. While the end cap and dead layer attenuate the intensity of these gamma rays by factor of four, the inner-most shielding layer of copper is stopping them practically completely.
The aluminium used for the end cap is quoted by the manufacturer to be of 'low background', with purity specifications (compare Section 4.5), that can be translated into a maximum contamination with ^{238}U of 12.3 mBq/kg. MC simulations based on this contamination level however, result only in a net count-rate-contribution of less than 0.2 % of the measurand in the 92.6 keV peak area. A potential source of this contamination is the field effect transistor (FET), that is situated directly below the detector, since FETs are known to be often contaminated with uranium and thorium [Pov18]. Another probable location are the high-voltage contacts of the germanium crystal. Contacts from the same manufacturer are reported to contain 19(9) Bq/kg of 238U contaminations [HMS$^+$18]. However, due to the lack of detailed knowledge about the exact locations inside the detector end cap or the purity of the used materials, no further investigations are conducted.
Since the 46.5 keV line of ^{210}Pb is even higher than expected only from decays within the ^{238}U series, an additional contribution has to be very close to the detector as well. Soldering lead at the detector contacts could be the origin of this contribution [Ned14].

Several peaks in the background spectrum can be assigned to ^{228}Ac, ^{212}Pb, ^{212}Bi and ^{208}Tl, which are all part of the ^{232}Th decay series. In contrast to the aforementioned ^{238}U decay chain, the discrepancies between the upper and lower part of the decay chain are smaller here. However, when evaluating this

decay chain, interferences as well as intrinsic branching ratios for the progenies have to be considered. The estimation of the location for these impurities is also more complex, due to the higher energies of the gamma rays involved.
Again, the aluminium end cap is considered to be a contributor with a maximum activity of 4.1 mBq/kg of ^{232}Th contained, based on the provided purity specifications [Can08], but MC simulations only support contributions of less then 0.1 % to the measured main gamma lines. The 2614.5 keV line of ^{208}Tl is suffering a minor contribution from the thermal neutron capture reaction $^{207}\mathrm{Pb}(\mathrm{n},\gamma)^{208}\mathrm{Pb}$, that can be estimated with about 0.01 counts/d using MC simulations for the detection efficiency, the cross section of 0.712 b [NNDCN18] and the thermal neutron flux from [ŠAK+92].

The most prominent line above the 511 keV annihilation peak is observable at 1460.8 keV and associated with the primordial radionuclide ^{40}K. Due to the relatively high energy of these gamma rays, a large number of possible sources has to be considered for the origin of this radionuclide.

The lead shielding of 150 mm is attenuating gamma rays with this energy by more than four orders of magnitude [BHS+10]. The radiopurity screening of the sand lime bricks supporting the cast iron ceiling for example yield a contamination of 145.0(47) Bq/kg. A MC simulation with 75×10^9 events is used to simulate the decays inside the 6000 kg walls. No energy depositions inside the FEP are observed, supporting the unlikelihood of the sand lime bricks being the main origin for the 1460.8 keV gamma rays seen by the germanium detector. Similar results are obtained for the barite concrete that contains 16.4(6) Bq/kg of ^{40}K. Although the total mass of the barite concrete inside the outer shielding is large, the small solid angle and self-absorption effects inside the massive walls reduce the detection efficiency drastically.

Polyethylene (PE) can be contaminated with ^{40}K. Using a MC simulation to determine the activity in the 54.5 kg of BPE inside the DLB's inner shielding (see Section 4.3), results in a specific activity of 181.7(58) mBq/kg. A similar analysis was performed with the background spectrum recorded in 2009 and resulted in a specific activity of 180.0(22) mBq/kg of ^{40}K [Ned14]. But since screening measurements of the used BPE resulted in an upper limit of 64 mBq/kg (95 %CL) [Ned14], only about one third of the net count rate in the 1460.8 keV line can be associated with the BPE layer of the inner shielding. Additional, potentially contaminated, materials are located closer to the germanium crystal, inside the detector end cap. The o-ring, that is sealing the end cap, for example, has

been reported to contain some Bq/kg of ^{40}K as well as other radioimpurities [BEH^{+}17]. Since no radiopurity screening data is available for any of the parts inside the germanium detector's end cap as well as exact locations are unknown this investigation is not pursuit further.

Anthropogenic ^{137}Cs is not present in the spectrum since no detection is made at 661.6 keV. ^{60}Co on the oder hand is detected with the intensities of both gamma rays at 1173.2 keV and 1332.5 keV being in good agreement. The origins are probably a contamination of the stainless steel used for the detector arm as well as cosmogenic activation inside the copper shielding. MC simulations are performed to determine the detection efficiency for the stainless steel parts and the inner-most copper layer of the shielding layout. Based on the net count rates in Table 7.1, a specific activity of 121(24) mBq/kg is determined for ^{60}Co in the detector arm. The same analysis performed for the copper shielding-layer results in a specific activity of 224(44) µBq/kg.
Since no radiopurity screening data is available for the used materials, the results can only be compared with data from the literature. While M. Köhler et al. report 250 mBq/kg found for ^{60}Co in a German steel sample [K^{+}04], the origin and quality of the stainless steel used inside the DLB's detector is unknown. The manufacturer states to be selecting steel with low ^{60}Co content [Can08].
L. Baudis et al. report on the cosmogenic activation of copper [BKPS15]. The specific saturation activity at sea level is stated with 340 µBq/kg, but since the inner shielding of the DLB is continuously covered by an overburden of 10 m.w.e. for the last eight years, it can be expected that the activity levels are lower inside the DLB shielding. The peaks are most likely caused by a mixture of unknown composition from both materials. ^{60}Co produced inside the germanium crystal due to cosmogenic activation is negligible, since the activation levels in natural germanium are about a factor of 1×10^3 to small to cause considerable contributions [WMZ17].

7.1.2. Cosmogenic activation products

Some of the most prominent peaks observable in gamma ray spectrometry background spectra, especially in shallow depth laboratories, are induced by the cosmogenic activation of detector and shielding components. In Sections 3.2.3 and 3.2.4 the production processes for these activation-nuclides are discussed in more detail. The majority of these peaks is induced by the interaction of thermal and

fast neutrons with germanium. Due to the involved half-lives of the decaying activation and spallation products, their contribution to the residual background can decrease significantly during the operation of a detector system, especially when operated deep underground.

Shielding components

While shielding parts outside of the neutron moderator are only subject to smaller thermal neutron fluxes, neutron-capture reactions are more likely in the inner-most layers of the shielding, due to the neutron-moderating BPE. Most of the activated radionuclides found in the background spectrum are produced in copper, whose majority is located in the 8 mm thick inner-most shielding layer (including the removable plug, see Figure 4.3). Since the mass of the detector end cap is relatively small compared to the copper ($< 1\,\%$), aluminium-activation products are less crucial. Iron-activation products are also less prominent, since most of the detector arm is shielded from the germanium crystal due to the ULB version of the detector.

Table 7.2.: Analysis of cosmogenic activation products on the copper shielding layer. Specific activity determined as weighted mean of several peaks (see Table B.1 for all peaks) or upper limit (95 %CL.). Half-lives taken from [NNDCN18]. Literature values for the saturation activity of copper activation products taken from [BKPS15] are given for sea level and no overburden.

Nuclide	Half-life [d]	Peak [keV]	Net count rate [counts/d]	Spec. Activity [µBq/kg]	$A_{\text{Sat.}}$[BKPS15] [µBq/kg]
^{54}Mn	312.19	834.85	0.40(18)	64.2(289)	154
^{56}Co	77.24	846.77	<0.225	<41.3	108
^{57}Co	271.81	122.06	<0.98	<185	519
^{58}Co	70.85	810.76	<0.33	<53.6	798
^{59}Fe	44.49	1099.25	<0.215	<90.8	47

Table 7.2 lists several peaks that are induced by radionuclides, which are produced by activation of copper in (n, γ)reactions. Cosmic muon-induced neutrons are captured after their thermalisation in the neutron moderating BPE layer of the shielding. Using FEP detection efficiencies determined in MC simulations, the measured peak intensities can either be directly converted into specific activities or upper limits can be derived. The table also includes the saturation activities

for the activation of copper during unshielded exposure to cosmic rays at sea level [BKPS15]. Below 10 m.w.e. of overburden, the production rates of the individual activation products are lowered accordingly. Since the inner shielding is continuously kept under the overburden of the outer shielding for more than eight years and the half-lives of the involved radionuclides are all well below one year, it can be assumed that saturation activity is reached for all the investigated activation products. Consequently, the saturated activities are hardly detectable under the present background conditions, even though the presented extensive measurement of the background spectrum was performed.

Only for ^{54}Mn a net count rate exceeding the DT is found and converted into a specific activity for the copper shielding layer of only 64.2(289) µBq/kg. All other investigated radionuclides result in upper limits between 40 and 185 µBq/kg. The measured saturation activities reported by Baudis [BKPS15] can be used for a comparison, keeping in mind that they are scaled to sea level production rates without overburden. The activation took place at the High Altitude Research Station Jungfraujoch at 3470 m above sea level [BKPS15].

Besides copper, other detector components are subject to cosmic ray-induced radionuclides that result in the emission of gamma rays as well. In addition to neutron capture reactions, excited nuclides are created in neutron scatter reactions $(n, n'\gamma)$on shielding components. These peaks were not detectable in previous background measurements [Ned14]. Table B.1 in Appendix B includes the peaks caused by the de-excitation of nuclei after neutron-scatter reactions, that are observed in the presented background spectrum.

For the $^{207}\mathrm{Pb}(n, n'\gamma)^{207*}\mathrm{Pb}$ reactions for example, a weighted mean of 7.3(37) de-excitations per d and kg of lead is determined. Here, only the mass of the ultra low activity layer of lead is considered, since gamma rays from the outer layers are attenuated by at least a factor of 100 and therefore negligible. The inner-most lead layer however, is separated from the germanium crystal only by the copper layer of the shielding and the aluminum end cap.

The detector's end cap is subject to a neutron scatter reaction as well. But only an upper limit for the de-excitations of ^{27*}Al can be obtained with $<$48.4 de-excitations per d and kg of aluminum, $<$8.4 de-excitations per d inside the end cap, respectively.

For ^{63*}Cu, that is produced in neutron scatter reactions in copper, a weighted mean of 26(11) de-excitations per d and kg of copper is obtained. 14.2(77) de-excitations per d and kg are determined for ^{65*}Cu. The difference represents the

natural abundance of both isotopes in copper (compare Table 3.3).

Germanium crystal

Table 7.3.: Peaks of cosmogenic activation products in natural germanium. BE denotes the binding energy, that is detected in addition to the gamma ray energy. Specific activities are determined as weighted means of several peaks, if more than one peak exceeds the DT (peaks listed in Table B.1). Otherwise na upper limit (95 %CL.) is reported.

Nuclide	Peak energy [keV]	Gamma ray + BE [%]	Net count rate [counts/d]
^{54}Mn	840.84	834.85 + 5.99 (BE Cr)	<0.45
^{57}Co	143.59	136.47 + 7.11 (BE Fe)	2.70(47)
^{58}Co	817.9	810.77 + 7.11 (BE Fe)	<258
^{65}Zn	1124.53	1115.55 + 8.98 (BE Cu)	<42
^{68}Ge	1077.34	-	<0.327

Although the same radionuclides can be produced in germanium and copper, they can be separated in the resulting spectrum. Intrinsically decaying radionuclides are visible with a peak at higher energy, since the binding energy (BE) of the daughter nuclide is also deposited in the detector crystal [Ned14]. The resulting peak energies for the four activation products in germanium ^{57}Co, ^{58}Co, ^{54}Mn and ^{65}Zn are listed in Table 7.3. Their half-lives range from 70 d to 313 d. Additionally, ^{68}Ge is created when germanium (natural abundance see Table 3.3) is exposed to cosmic radiation. The radionuclide decays into ^{68}Ga via electron-capture without the emission of gamma rays and a half-life of 270.95 d [NNDCN18]. Subsequently, ^{68}Ga undergoes a beta plus decay or electron-capture with a half-life of only 67.8 min. This second decay is accompanied by gamma-rays of low intensity. The most prominent gamma ray has an energy of 1077.3 keV and is emitted with only 3.2 % emission probability. Due to the difference in their half-lives, both radionuclides are usually in equilibrium and the activity determined by the detection of the ^{68}Ga gamma ray can be assumed for ^{68}Ge as well.

After determining the FEP detection efficiency via MC simulations, the specific activities are calculated and shown in Table 7.4. The peak at 143.7 keV, caused by ^{57}Co, contains an unkown contribution of ^{235}U (143.76 keV, 10.96 %) and the

calculated activity is therefore overestimated. From the other detected ^{235}U-peak-energies (163.36 keV and 205.32 keV) it can only be estimated that about half of the peak's intensity is caused by ^{235}U decays. However, there are discrepancies concerning the peaks in the background spectrum associated with ^{235}U, which are discussed extensively in [Ned14]. Consequently, the result for ^{57}Co in Table 7.4 is not corrected for any external contributions.

The saturation of a given radionuclide is reached once the production rate and the decay of the nuclide are equal. In general, this is the case after six half-lives, when more then 99 % of the final activity is reached. The HPGe detector of the DLB is kept inside the inner shielding continuously for the last eight years. Additionally, the entire inner shielding is only moved away from the measurement position, where the coverage is maximised, for the re-filling of liquid nitrogen or sample exchanges. Due to these constant conditions and the half-lives of the above mentioned activation products (see Table 7.4), it can be assumed that all nuclides have reached their saturation activity. In principle, it is possible to calculate these activities using information about the relative nuclide-production rates and time windows of different shielding conditions. But the time windows are unknown for the DLB's detector, especially for the time of storage between production and delivery. M. Hult shows in [HMS$^+$18] that the intrinsic background of a detector system may decrease by about 30 % after several years of shielded operation, mainly due to the decay of cosmogenic activation products.

Table 7.4 also includes saturation activities for the production of cosmogenic radionuclides in natural germanium. These values can be used to compare the obtained results. S. Cebrian provides an extensive discussion about the activation of different materials when exposed to cosmic rays at sea level [Ceb17]. The table contains the mean values for the production rates listed by Cebrian, which are then converted into saturation activities. Certainly, the activities obtained without overburden are larger than all upper limits calculated from the background spectrum.

Wei et al. discuss calculations based on the MC codes Geant4 and ACTIVIA, which are performed for a cylinder of natural germanium shielded by iron. The iron-overburden corresponds to about 6.7 m.w.e.. This results in conditions, comparable to the DLB (compare Figure 3.3) and gives saturation activities that can be compared more directly to the DLB results. While the values for ^{54}Mn, ^{58}Co and ^{68}Ge are in agreement, the reported activity from Wei for ^{57}Co reveals the above mentioned contribution from ^{235}U to the peak area at 143.6 keV. For ^{65}Zn however, the upper limit obtained from the background spectrum is about three

Table 7.4.: Activities of activation products in the germanium detector derived from the background spectra acquired in 2009, 2014, 2015 and 2017. Efficiencies determined by MC simulations for the energies given in Table 7.3. Upper limits are given at 95 % C.L.. Saturation activities taken from the given references, converted into activities if production rates are presented.

Nuclide	DLB 2009 715.9 h [µBq/kg]	DLB 2014 965.9 h [µBq/kg]	DLB 2015 715.9 h [µBq/kg]	DLB 2017 2224 h [µBq/kg]
^{54}Mn	<50	<40	<52	<26.9
^{57}Co	79(16)	27(13)	38(12)	36.1(61)
^{58}Co	<46	<48	<47	<19.2
^{65}Zn	370(140)	<70	<134	<63
^{68}Ge	<3030	<1910	<1640	<1060
	Half-life [d]	$A_{\text{Sat.}}$ [Ceb17] no shield [µBq/kg]	$A_{\text{Sat.}}$[WMZ17] ∼6.7 m.w.e. [µBq/kg]	$A_{\text{Sat.}}$ [vSHRS16] 620 m.w.e. [µBq/kg]
^{54}Mn	312.19	43.9	3.6	<23
^{57}Co	271.82	79.9	11.9	11(2)
^{58}Co	70.85	95.1	10.4	<3.5
^{65}Zn	244.01	618	206	77(14)
^{68}Ge	270.95	490	583	313(20)

times lower than the activity reported in [WMZ17]. It should be noted, that the results for the unshielded case, which are obtained by Wei et al. using three different MC codes, differ by a factor for four. For the shielded case however, only one result is reported and no statement about the accuracy is made [WMZ17].

Finally, the saturation activities for a HPGe detector located in a deep underground facility are given for comparison as well. Due to 620 m.w.e. of overburden, this detector is considerably better protected against cosmic rays and the reported activities are generally all below the upper limits obtained for the DLB [vSHRS16].

The values for the production rates of cosmogenics differ considerably within the literature, where the majority of values is obtained by calculations and MC simulations. Additional measurements are therefore necessary to improve the results and increase the accuracy of these predictions.

7.1.3. Neutron-induced gamma lines

Not all peaks in the residual background spectrum are caused by the decays of natural occurring radionuclides and cosmogenic activation products. Several of the remaining peaks are, in fact, caused by thermal neutron capture reactions ($^{A}\mathrm{X}(\mathrm{n},\gamma)^{A+1}\mathrm{X}$) or inelastic neutron scatter reactions ($^{A}\mathrm{X}(\mathrm{n},\mathrm{n}'\gamma)^{A}\mathrm{X}$) with the germanium crystal itself. Up to energies of 11 MeV, these mechanisms are dominating the energy depositions of neutrons, with elastic scatter ractions giving the largest contribution to the interaction probability for germanium up to neutron energies of 50 keV [BVP18].

Different metastable nuclides or excited states of isotopes can be produced (compare Table 3.3). Table 7.5 lists the most prominent peaks caused by tertiary neutrons interacting with the germanium detector.

In case of short-lived excited states or metastable nuclides, the corresponding gamma ray's energy deposition can be rejected from the spectrum by applying a rejection time of after each muon veto detector event, e.g. 50 µs. For example, the 174.9 keV gamma ray of ^{71m}Ge is suppressed effectively by the muon veto due to the half-life of only 79 ns. Peaks, originating from de-excitation, with half-lives longer than the applied rejection time, can not be reduced effectively by this active reduction technique. The intensity of these peaks, however, is influenced by the effectiveness of the neutron moderator and absorber that is incorporated in the shielding.

The de-excitation of the 66.7 keV metastable state of ^{73}Ge is accompanied by

Table 7.5.: Peaks in the residual background spectrum caused by neutron capture reactions and neutron scatter ractions in natural germanium.

Reaction	Peak energy [keV]	Net count rate [counts/d]
$^{70}\mathrm{Ge}(\mathrm{n},\gamma)^{71m}\mathrm{Ge}$	174.95	<1.11
$^{70}\mathrm{Ge}(\mathrm{n},\gamma)^{71m}\mathrm{Ge}$	198.4	6.89(54)
$^{72}\mathrm{Ge}(\mathrm{n},\gamma)^{73m}\mathrm{Ge}$	53.44	2.31(36)
$^{72}\mathrm{Ge}(\mathrm{n},\gamma)^{73m}\mathrm{Ge}$	66.72	22.39(86)
$^{72}\mathrm{Ge}(\mathrm{n},\mathrm{n}'\gamma)^{72}\mathrm{Ge}$	689.6	<0.56
$^{72}\mathrm{Ge}(\mathrm{n},\mathrm{n}'\gamma)^{72}\mathrm{Ge}$	691.4	<0.26
$^{73}\mathrm{Ge}(\mathrm{n},\mathrm{n}'\gamma)^{73*}\mathrm{Ge}$	68.75	<0.105
$^{74}\mathrm{Ge}(\mathrm{n},\gamma)^{75m}\mathrm{Ge}$	139.68	5.46(51)
$^{74}\mathrm{Ge}(\mathrm{n},\mathrm{n}'\gamma)^{74*}\mathrm{Ge}$	595.85	<0.40
$^{76}\mathrm{Ge}(\mathrm{n},\gamma)^{77m}\mathrm{Ge}$	159.70	1.12(40)
$^{76}\mathrm{Ge}(\mathrm{n},\gamma)^{77}\mathrm{Ge}$	264.44	<0.301
$^{76}\mathrm{Ge}(\mathrm{n},\mathrm{n}'\gamma)^{76}\mathrm{Ge}$	545.51	<0.35
$^{76}\mathrm{Ge}(\mathrm{n},\mathrm{n}'\gamma)^{76}\mathrm{Ge}$	562.93	<0.46

the sequential emission of two gamma rays with 53.4 keV and 13.3 keV, respectively. Since the 13.3 keV level has a half-life of 2.95 µs [NNDCN18], it is likely that this second transition occurs during the shaping time of the main amplifier of 6 µs. Therefore, the peak at 66.7 keV, representing the sum of both gamma rays, is much higher than the 53.4 keV line. It is the by far most intense line in the background spectrum below 500 keV.

The flux of thermal neutrons within the shielding can be estimated by analysing the $^{74}\mathrm{Ge}(n,\gamma)^{75m}\mathrm{Ge}$ reaction, that causes the emission of 139.7 keV gamma rays [ŠAK+92]. The flux can be calculated with

$$\Phi_{\mathrm{th}}\left(\frac{\mathrm{n}}{\mathrm{m}^2\,\mathrm{s}}\right) = \frac{R_{\mathrm{n},\,139.7\,\mathrm{keV}}}{N(^{74}\mathrm{Ge})\,\sigma(^{75}\mathrm{Ge})\,\frac{\varepsilon_{139.7\,\mathrm{keV}}+\alpha_{\mathrm{tot}}}{1+\alpha_{\mathrm{tot}}}} \quad , \tag{7.1}$$

where $R_{\mathrm{n},139.7\,\mathrm{keV}}$ is the net count rate of the 139.7 keV peak. $N(^{74}\mathrm{Ge})$ is the number of ^{74}Ge isotopes in the detector, which can be calculated from the sensitive detector mass and the natural abundance of from Table 3.3. $\varepsilon_{139.7\,\mathrm{keV}}$ is the FEP detection efficiency for the emitted gamma ray, which is determined by MC simulations ($\varepsilon_{139.7\,\mathrm{keV}} = 0.779 \pm 0.039$). Alternatively to the emission of a gamma ray, the de-excitation of ^{75m}Ge can occur by internal conversion. Then, the energy

of the excited nucleus is transferred to an electron from a lower shell, which is then emitted from the atom. This effect is taken into account by adding the total conversion coefficient $\alpha_{\text{tot}} = 1.524$ [NS13]. $\sigma(^{74}\text{Ge})$ is the partial neutron capture cross section for the process: $\sigma\left(^{74}\text{Ge}\right) = 0.14(1)\,\text{b}$ [Mug18].
Using these data, the thermal neutron flux at the location of the HPGe detector is determined with $1.3(2)\,\text{n}/(\text{m}^2\,\text{s})$.

In comparison to $30\,\text{n}/(\text{m}^2\,\text{s})$, which has been measured for a conventional shielding without neutron moderator, this proves the effectiveness of the neutron shielding of the DLB [ŠAK+92]. A similar analysis of the thermal neutron flux has been performed for the GIOVE detector at the MPI-K in Heidelberg, Germany, where a neutron flux of $4.8\,\text{n}/(\text{m}^2\,\text{s})$ is measured. Additional MC simulations predict a flux of about $2.2\,\text{n}/(\text{m}^2\,\text{s})$ [HMH16]. The difference between both detector systems can be explained by the size of GIOVE lead shielding, which is nearly three times the mass of the DLB lead shield. Hence, more tertiary neutrons are produced when cosmic muons are interacting with the high-Z material of the shielding.

Fast tertiary neutrons are causing the inelastic scatter reaction $^{72}\text{Ge}(n, n'\gamma)^{72}\text{Ge}$, which is inducing an asymmetric peak at 691.4 keV. Based on the net count rate of this peak, the flux of fast neutrons can be estimated with the empirical formula [ŠAK+92]:

$$\Phi_{\text{fast}}\left(\frac{\text{n}}{\text{m}^2\,\text{s}}\right) = k\frac{R_{\text{n,691.4 keV}}}{V}. \tag{7.2}$$

Here, R_{n} denotes the net count rate of the 691.4 keV peak. V is the sensitive volume of the detector ($234\,\text{cm}^3$) and k an empirical factor of k =900 [ŠAK+92]. Since only an upper limit is obtained for the peak's intensity (see Table 7.5), the fast neutron flux can only be estimated with $< 0.116\,\text{n}/(\text{m}^2\,\text{s})$.

This value is more than three orders of magnitude smaller than the value of $170\,\text{n}/(\text{m}^2\,\text{s})$ for a conventional system without integrated neutron shielding [ŠAK+92]. R. Lindstrom et al. estimate the flux of fast neutrons inside a 150 mm lead shield, that is situated above ground, from the above mentioned reaction and the $^{74}\text{Ge}(\text{n}, \text{n}'\gamma)^{74*}\text{Ge}$ reaction where 595.8 keV gamma rays are induced. The flux for neutrons above 1 MeV is then estimated with $200\,\text{n}/(\text{m}^2\,\text{s})$ [LLSL90]. S. Niese reports about neutron flux measurements performed in the Felsenkeller laboratory in Dresden, Germany, which is covered by 47 m of hornblende monzonite-rock, corresponding to 125 m.w.e. of overburden. While above ground a flux of

$28\,\mathrm{n}/(\mathrm{m}^2\,\mathrm{s})$ was measured, under the rock overburden only $2.6\,\mathrm{n}/(\mathrm{m}^2\,\mathrm{s})$ was determined. Using 50 mm of lead shielding the flux measured in another rock environment increased from $0.26\,\mathrm{n}/(\mathrm{m}^2\,\mathrm{s})$ to $3.9\,\mathrm{n}/(\mathrm{m}^2\,\mathrm{s})$, proving the production of tertiary neutrons by cosmic muons in high-Z materials. Note that [KDL+09] gives on overburden of only 110 m.w.e. for the same laboratory. Wordel et. al give an upper limit of $2\,\mathrm{n}/(\mathrm{m}^2\,\mathrm{s})$ for a detector system with 500 m.w.e. of overburden [WMA+96]. This demonstrates the neutron-reduction capability of the inner shielding design used in the DLB.

At the LNGS, below 3800 m.w.e. the cosmic muon flux is reduced to negligible levels. Neutrons at these depths are dominantly produced in fission processes and (α, n)-reactions. Measurements result in fluxes of $0.02\,\mathrm{n}/(\mathrm{m}^2\,\mathrm{s})$ for thermal neutrons and $0.026\,\mathrm{n}/(\mathrm{m}^2\,\mathrm{s})$ for fast neutrons [RCLM88].

BPE is used for the moderation and absorption of neutrons within the inner shielding of the DLB. The $^{10}\mathrm{B}\,(n,\alpha)\,^{7}\mathrm{Li}$ reaction is used for the capture of thermalised neutrons. However, a gamma ray of 477.6 keV is emitted by the excited ^{7}Li with an intensity of 93.7 % [NNDCN18]. Due to the improved background level, these gamma rays are now detectable in the background spectrum with $0.42(22)\,\mathrm{counts/d}$. Converted into a specific activity, this results in $9.4(49)\,\mathrm{mBq/kg}$ of BPE. With an formula similar to Equation (7.1) and a capture cross section of $\sigma = 3571\,\mathrm{b}$ [NNDCN18], the neutron flux causing the line's intensity can be estimated with $87.8(45)\,\mathrm{n}/(\mathrm{m}^2\,\mathrm{s})$.

When interpreting this result several factors have to be considered. The secondary neutron flux due to the cosmic radiation of about $64\ \mathrm{n}/(\mathrm{m}^2\,\mathrm{s})$ is decreased by the DLB's shielding to about $0.1\,\mathrm{n}/(\mathrm{m}^2\,\mathrm{s})$. However, additional tertiary neutrons are produced by cosmic muons in lead, giving rise to the neutron flux for the inward layers.

7.2. Composition of the residual background

The residual background of the DLB consists of different components. It was already discussed above, that cosmic muons, which are not detected by the muon veto detector, are contributing about half of the remaining background counts. Other contributions are induced by natural occurring radionuclides that are located inside detector components and shielding materials as contaminations and radioimpurities. Additionally, activation products are created due to the expose to cosmic rays inside the outer shielding of the DLB, which is reduced,

but not negligible. Within this section, an estimation of the contingents of the different components is made using MC simulations. The input for these simulations is based on the peak analysis from the Section 7.1 and data from the literature (e.g. [BFA+11, Ceb17, WMZ17]).

The 511 keV annihilation line is prominently visible in the background spectrum. Although it's majority is induced by cosmic muons, other contributions have to be considered here as well. When the muon veto detector is not applied during the measurement, the net count rate normalised to the sensitive germanium mass is $560.5(88)\,\mathrm{counts}/(\mathrm{d\,kg})$. For the GIOVE detector, which is situated under 15 m.w.e. of overburden, a net count rate of $614.9(94)\,\mathrm{counts}/(\mathrm{d\,kg})$ is obtained [HWH+15]. Due to a larger lead shielding, more positive muons are stopped inside the shielding, subsequently inducing additional 511 keV photons during their annihilation process.

When the DLB's background is actively reduced by the muon veto detector, the remaining net count rate in the peak are is $34.16(110)\,\mathrm{counts}/\mathrm{d}$, which gives a reduction factor of 20.5 The GIOVE detector achieves a normalised net count rate of $10.7\,\mathrm{counts}/(\mathrm{d\,kg})$, corresponding to a reduction factor of 58 [HWH+15]. Comparable count rates are reported for the detector system in the GUL with $9.8\,\mathrm{counts}/(\mathrm{d\,kg})$.

This comparison indicates an additional contribution to the 511 keV peak, that is not caused by cosmic muons, but by intrinsic contaminations of the detector system. Consequently, a further reduction of muonic contributions would decrease the peak's intensity considerably, but still result in a larger count rate than achieved in comparable detector systems.

A background spectrum is simulated based on the known activity levels of the different shielding materials and the cosmogenic activation of copper and germanium. Most of the simulated activities are based on upper limits, which are determined, for example, from purity specifications given by the different manufacturers or during the analysis of the residual background spectrum. Since not all materials have been screened for radioimpurities prior to their installation, the information that can be used as input is limited. The resulting simulated spectra are shown in Figures 7.2 and 7.3.

While Figure 7.2 shows the different contributing components as well as the resulting sum spectrum (red curve), Figure 7.3 compares this sum spectrum with the measurement of the background with muon veto (black curve). The

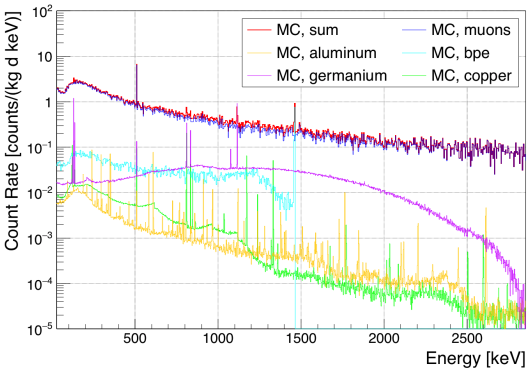

Figure 7.2.: MC simlulated background spectrum based on known activities inside detector and shielding components.

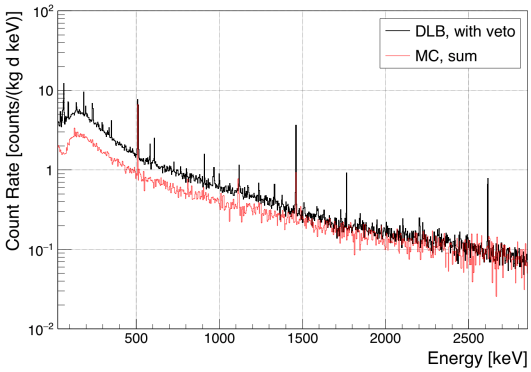

Figure 7.3.: Comparison between MC simulated background spectrum (red curve) and measurement (black curve).

limited information is evident in the MC generated spectrum, since too little contribution is simulated. Only 55.2 % of the integral count rate between 40 keV and 2700 keV are reproduced by the MC simulations. Thereof 91.4 % of the counts are muonic contributions. The copper shielding and detector end cap are contributing only small amounts to the overall integral count rate with 0.3 % and 0.2 %, respectively. 1.9 % are induced by the BPE impurities and 2.3 % are due to the activation of the germanium crystal, although the use of upper limits within this scenario should be noted here. Several gamma lines due to the primordial radionuclides and decay chains are not reproduced accordingly within the simulation.

A second MC is generated with naturally occurring radionuclides placed inside the aluminum of the detector end cap. Their relative amounts are scaled to the measurement to reproduce the net count rates of their most prominent gamma lines. Thereby, their relative contribution to the background spectrum can be estimated. In Figure 7.4 the different contributions and their sum spectrum are shown. A comparison between the sum spectrum and the measurement is shown in Figure 7.5.

The majority of counts is still induced by cosmic muons with about 50.5 %. Natural decay chains contribute 12.4 % from ^{238}U, 12.1 % from ^{232}Th and 6.7 % from ^{235}U. ^{40}K contributes 3.9 % and ^{60}Co introduces 0.9 %, respectively. The cosmogenic activation of the copper shielding is still negligible. About 2.2 % of the counts are induced by activation products produced in germanium, mainly due to of ^{68}Ge.

In comparison to the aforementioned simulation of the known radioimpurities, this demonstrates the lack of knowledge about material-contamination, especially with primordial decay chains, which are introducing at least 30 % of the residual background spectrum.

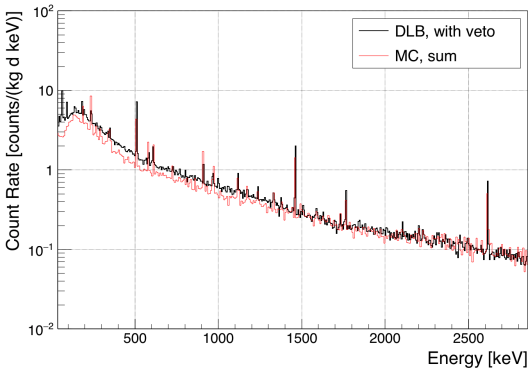

Figure 7.4.: Comparison of the MC simulated background spectrum with the measurement.

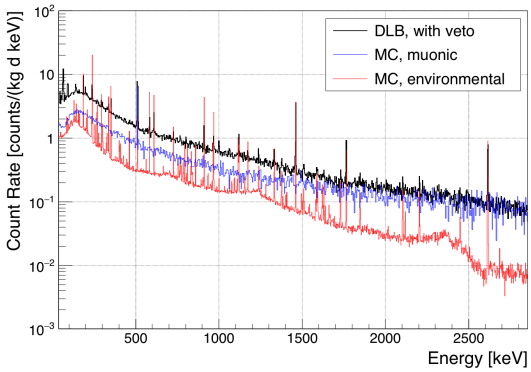

Figure 7.5.: Comparison of muonic (blue) and non-muonic (red) contributions to the measured background spectrum (black).

Although 88.7 % of the integral count rate between 40 keV and 2700 keV are reproduced by the MC generated spectrum, crucial parts of the spectrum are still not well described. Especially in the low-energy region counts, the count rate is underestimated. This supports the above mentioned assumption of a contamination located very close below the detector, where the low-energetic gamma rays are less attenuated since they do net have to penetrate the dead layer of the germanium crystal. In this case, the beta decay of the ^{210}Pb progeny ^{210}Bi (Q-value: 1162.2 keV [NNDCN18]) would contribute as well, which would raise the low-energetic continuum of the spectrum. Depending on the exact location of the contamination, even the alpha particles emitted by the ^{210}Bi-daughter ^{210}Po would be detectable. The continuous-slowing-down-approximation range of these 5.3 MeV alpha particles in germanium is about 1.4 mm [NNDCN18, MBC17]. However, these close-proximity contaminations are not considered in the MC model for the simulation results presented here, where only the aluminum end cap is assumed with contaminations.

Generally similar results are reported for MC simulations of the background characteristics of HPGe detectors situated deep underground [BBL$^+$18, BLP17]. Major contributions from natural radioactivity in detector and shielding components are found during these studies, while cosmic muons are of course negligible at these depths. However, an underestimation of the low-energy part of the

spectrum is reported, when uniformly distributed sources around the detector are assumed [BLP17].

The situation is very complex due to several potential locations with different amounts of contaminations, which are all contributing to the overall background seen by the germanium detector. This results in clearly visible peaks at higher energies, above 2 MeV, and low energies lines below 150 keV (compare Figure 7.1). While high-energetic gamma rays can, in principle, even be introduced from outside of the inner shielding, low-energetic must be originate from inside the detector end cap. MC simulations could be employed to evaluate if an additional layer of 50 mm of lead would be beneficial in terms of high-energy-background reduction from external sources.

This is the first attempt to quantitatively describe the residual background spectrum of the DLB, which is situated at a shallow depth of 10 m.w.e.. The understanding of the different components is crucial to evaluate possibilities to further decrease the background level of the spectrometer.

Muonic contributions are reduced for the most part, due to the improvements to the muon veto detector conducted over the past year. However, there is still a considerable amount of cosmic muon-induced events in the background spectrum. These parts may be minimised by the arrangements discussed in Section 6.3. So far, the muonic contribution is only estimated by scaling the MC generated spectrum to the residual background spectrum. The integration of the muon veto detector into the GDML model and the MC simulation could improve this estimation. This would also enable an improved understanding of the veto detector's efficiency as well as identify weak spots in the angular coverage of the veto detector.

The other major contributors to the background are several sources of naturally occurring radionuclides within the shielding and detector components. Different peak intensities for different gamma ray energies indicate multiple locations throughout the detector system, that are adding up to the overall contribution. Practically no radiopurity screening data is available for the used materials, which increases the complexity of an investigation at this point. An analysis of the background spectrum in the energy range up to about 8 MeV, which covers the energies of alpha particles emitted by the alpha decaying radionuclides within the natural decay chains, could bring evidence for close-proximity contaminations below the detector crystal. However, although possible, the removal of any of these parts is linked with considerable efforts and risks, once a detector

system is installed and operational like the DLB.

Another component, that is not included within the MC simulations of the residual background, are neutrons inside the inner shielding. The simulation of neutron-capture reactions could help to verify the above mentioned results for cosmogenic activation products. Thereby, the uncertainty of the fraction of the background contribution due to these components can be improved. Geant4 based MC simulations of muon-induced neutrons penetrating a low-background spectrometer are reported in the literature [HMH16]. The inclusion of neutron-scatter-induced gamma rays into the simulated background spectrum would enable the reproduction of the gamma lines from Table 7.5.

7.3. Radioassay measurements

Different radiopurity screening measurements have been performed utilising the low-background environment and the HPGe detector. These include the participation in several proficiency tests organised by the International Atomic Energy Agency (IAEA) as well as different sample-screenings for the COBRA experiment and medical physics applications Chapter 8. A short list of measurements, that are enabled by the remarkably low-background environment of the DLB is discussed here.

It should be noted, that the DLB-background spectra shown in this section may vary from the lowest background spectrum shown in Figure 7.1, since the different measurements are performed between 2015 and 2018.

IAEA reference sample

Within the scope of the IAEA-TEL-2017-03 proficiency test, a water sample is measured. The sample is spiked with radionuclides of known activities, which enables the comparison between the measurement and reference values. Contained inside the water are the relatively low amounts of about 20 Bq/kg per radionuclide.

Table 7.6 shows the results obtained during a 24 h measurement performed with the DLB, which are in very good agreement with the reference values provided by the IAEA. Although the active muon veto detector would not have been necessary for these activity levels, the decrease of background contributions is reducing the measurement time considerably (compare Equation (2.13)). The standard uncertainties for the DLB results are dominated by the systematic uncer-

Table 7.6.: Spectrometric results of spiked water.

Nuclide	Specific Activity IAEA value [Bq/kg]	Specific Activity DLB result [Bq/kg]
^{60}Co	17.6(2)	17.91(43)
^{133}Ba	23.0(2)	22.87(38)
^{152}Eu	23.3(3)	23.37(56)

tainty of the MC based determination of the FEP detection efficiency.

COBRA detector coating

Regularly, screening measurement are performed on samples of construction materials intended for the use inside the COBRA experiment. The low-background demonstrator setup at the LNGS is set up to investigate the ULB operation of CdZnTe semiconductor detectors for the search for neutrino-less double beta decays.

The measurement shown here is performed on a 129.6 g sample of epoxy varnish, that is used for the detector coating. A measurement time of 500 h resulted in the spectrum presented in Figure 7.6, where it is shown in comparison with the residual background of the DLB. Clearly visible are numerous peaks due to both uranium decay chains as well as ^{232}Th and its daughter nuclides, which make the epoxy unsuitable for the use in the scope of a low-background experiment.

The measurement results in activities of 5.7(11) Bq/kg ^{238}U, with no signs of a disequilibrium within the decay series. ^{235}U is not detected with a DT of 109 mBq/kg, however, if the natural abundance-ratio is applied, an activity of about 40 mBq/kg can be expected. The ^{232}Th decay chain is measured with a specific activity of 1.14(26) Bq/kg and ^{40}K with 229(71) mBq/kg. All standard uncertainties are dominated by the systematic uncertainty of the MC model for the FEP detection efficiency determination. The uncertainty is increased to 20 % for this measurement, since the exact chemical composition of the epoxy is unknown and only estimated based on comparable commercially available epoxies.

In addition to the spectrum of the epoxy and the residual background spectrum, another background spectrum is included in Figure 7.6. The green curve shows the background that was recorded within the outer shielding of the DLB but only with a conventional 50 mm lead shielding. This illustrates the necessity

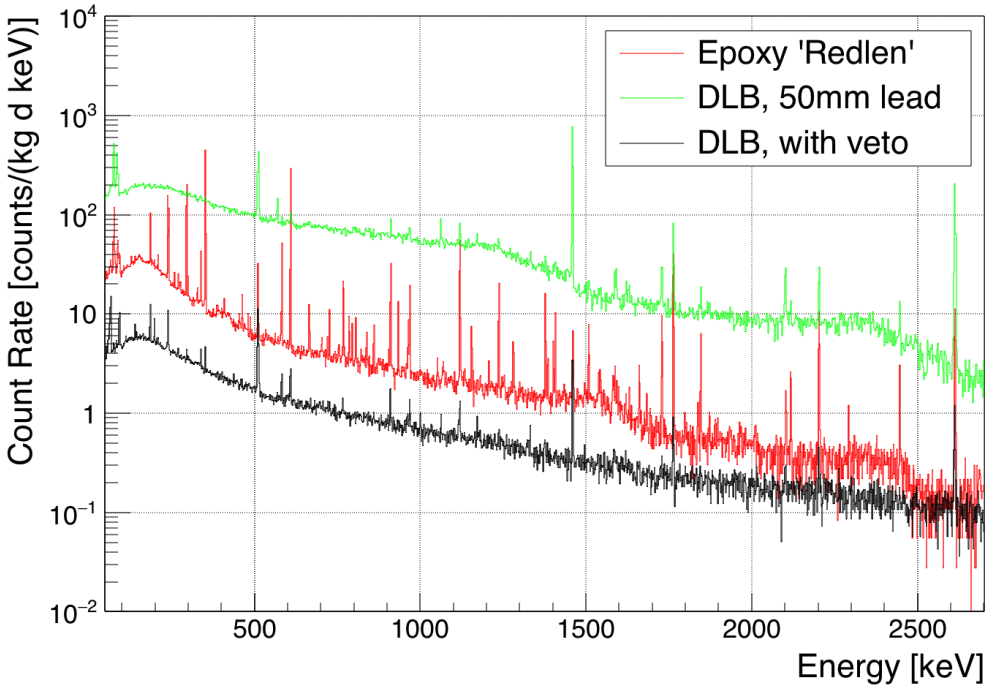

Figure 7.6.: Radiopurity screening of an epoxy varnish intended for the coating of CdZnTe detectors of the COBRA experiment. The sample measurement (red) is shown in comparison to the residual background spectrum of the DLB (black). Additionally, the background level achieved only by a conventional shielding of 50 mm of lead is shown (green).

of the DLB's extensive inner shielding and the application of active cosmic muon reduction techniques to achieve the residual background, which is about 50 times lower. With a conventional shield this detection would not have been possible within the same measurement time.

Since the above mentioned epoxy varnish is unsuitable for the application within COBRA, an alternative epoxy was screened with the DLB for radioimpurities. A relatively brief measurement of 65 h resulted only in upper limits in the range of tens of mBq/kg for the primordial radionuclides. The 244 g sample was then send to a deep underground facility and screened again with the gamma ray spectrometer OBELIX [BEH+17]. This spectrometer utilises a residual background that is 35 times lower than the DLB's background. Due to the pre-screening measurements obtained with the DLB, about 900 h of measurement time were invested to obtain results for radionuclides of the ^{238}U and ^{232}Th decay chains between 1 mBq/kg and 8 mBq/kg. To achieve the sensitivity for these

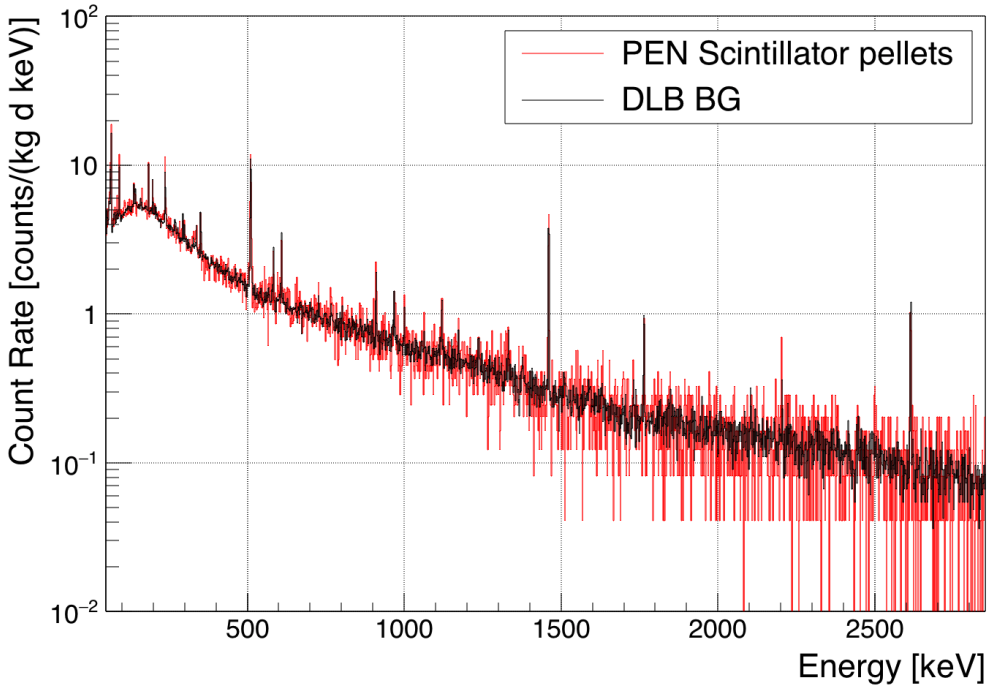

Figure 7.7.: Radiopurity screening of PEN scintillator pellets. The sample measurement (red) is shown in comparison to the residual background spectrum of the DLB (black).

detections, the DLB would have needed about 2000 h of measurement time (compare Equation (2.13)).

PEN scintillator pellets

In Chapter 2 it was already mentioned, that PEN is a scintillating plastic with beneficial characteristics compared to conventional plastic scintillators. For the usage in low-background environments the radiopurity of the material is crucial. B. Majorovits et al. present the results of radiopurity measurements, that include a contamination of ^{40}K of 1.6(4) Bq/kg and 1.0(4) Bq/kg for two samples [MEF+18]. A potential origin of this contamination might by the catalyst that is used during the PEN synthesis [MEF+18].

A sample of 276.9 g of PEN pellets is measured with the DLB for about 300 h. The resulting spectrum together the the residual background spectrum is shown in Figure 7.7.

Since all peaks investigated in the measurement are compatible with the background spectrum, only upper limits for all radionuclides can be reported. With a DT of 80 mBq/kg no detection is made for ^{40}K. The measurement results in an upper limit of 134 mBq/kg (95 % C.L.) for the specific activity of ^{40}K. A con-

tamination as mentioned above would have been detected. However, it would be beneficial to lower the limits for all potential contaminating radionuclides, in case no detection can be made. More measurement time with the DLB detector or another screening measurement, performed with a deep underground ULB spectrometer, are therefor necessary.

Radiopharmaceutical ^{99m}Tc

The radiopharmaceutical ^{99m}Tc is widely used in diagnostic nuclear medical imaging, for example to display the blood flow to the heart muscle or map the spread of cancer cells to the bones [Con10]. A sample, containing a high activity of medical technetium, was measured with the DLB spectrometer during a bachelor's thesis in 2015 [Lin15]. In general, a low-background HPGe detector is not suitable for the measurement of very high activities. However, a measurement is possible after a few days due to the radionuclide's half-life of 6.01 h [NNDCN18]. Depending on the measurement time, the decay during the measurement has to be corrected according to Section 2.2.3.

C. Linker reports an activity for ^{99m}Tc of 6.96(41) MBq for the 2 g sample [Lin15]. The spectrum after 161 h of measurement time is shown in Figure 7.8, where the very prominent peak due to the de-excitation gamma rays can be seen at 140.38 keV. In addition, several other peaks are visible in the measured spectrum, that are not stemming from the residual background of the DLB that is shown for comparison as well. The peaks at 181.46 keV, 739.45 keV and 777.18 keV can be identified as ^{99}Mo-lines. This contribution is plausible, since ^{99m}Tc is usually extracted from a source of ^{99}Mo using a so-called 'Technetium-99m generator'. The activity of 0.42(1) Bq found in the sample is well below the limit for the ^{99}Mo/^{99m}Tc ratio [Lin15].

^{99}Mo is produced during the capture of thermal neutrons in ^{235}U, which induces a spallation of the uranium nucleus via the reaction:

$$^{235}\mathrm{U} + n \rightarrow {}^{236}\mathrm{U} \rightarrow {}^{99}\mathrm{Mo} + {}^{134}\mathrm{Sn} + 3n. \tag{7.3}$$

Since only 6.1 % of all fission products are ^{99}Mo, complex radiochemical separation and purification steps are used to achieve the required high purity requirements [Con10]. The detected ^{238}U decay chain activities are probably remnants of this production process. Several peaks are related to the ^{232}Th decay chain, that may be introduced to the sample by the alpha decay of ^{236}U. An activity of

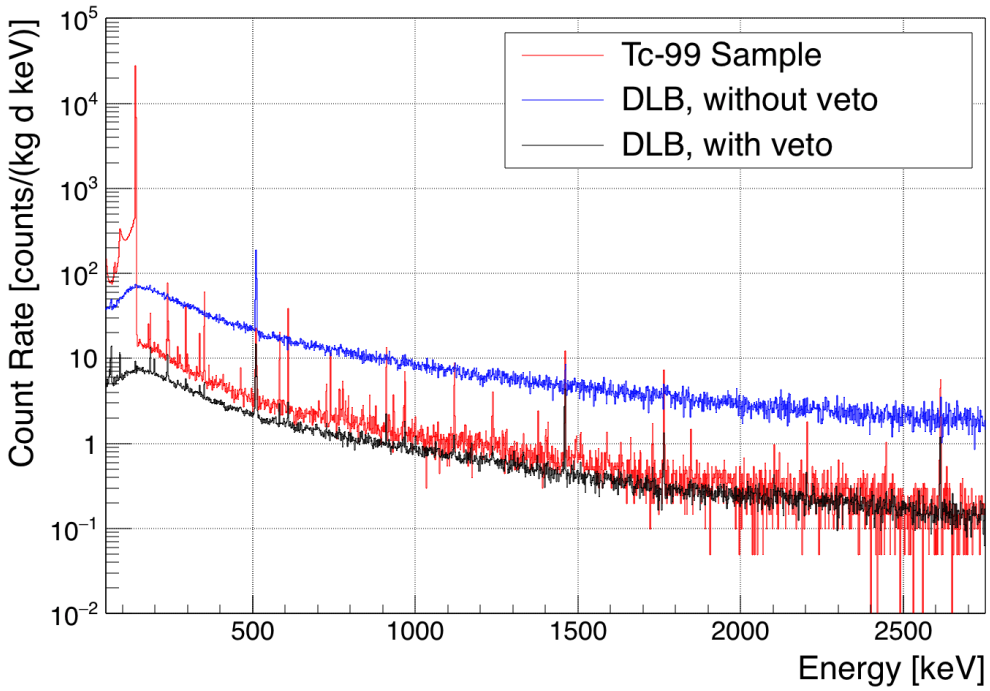

Figure 7.8.: Spectrometric measurement of a medical ^{99m}Tc sample. The measurement of the sample (red) is shown in comparison to the residual background spectrum of the DLB (black). Additionally, the background level achieved without the muon veto detector applied during the measurement is shown as well (blue).

12.8(29) Bq/kg is determined for the ^{238}U decay chain, without signs for a disequilibrium.

Figure 7.8 illustrates that the detection of the additional contaminations due to uranium and thorium is only possible since the DLB provides a low-background environment for the measurement. With a conventional shielding this detection would not have been possible. The muon veto detector of the DLB reduces the necessary measurement time drastically.

8. Proton Activation Analysis

Brass apertures are used in proton beam therapy to form the lateral shape of the beam. These patient-specific devices are subject to radioactivation during the exposure to high energetic protons. In this chapter, the results of gamma spectrometric measurements performed on activated samples are presented. A brief overview of proton beam therapy in general is given before the WPE is briefly introduced. The measurements of different monitor reaction cross sections are presented, which are subject of a current publication, co-authored by the author of this work [BBG+19]. This is followed by the spectrometric analysis of a brass samples irradiated with 226 MeV and 100 MeV protons.

8.1. Proton beam therapy

W. Newhauser et al. provide an extensive review of the recent developments in the field of proton beam therapy [NZ15].

Proton beam therapy (sometimes just 'proton therapy') is increasingly used for the treatment of tumour patients, especially if the sparing of normal healthy tissue is of utmost importance. The use of accelerator-produced proton beams for the treatment of deep-seated tumours was first proposed in 1946 within a published paper of R. Wilson, in which the biophysical rationale for proton therapy as well as the key engineering techniques of the beam delivery were presented [Wil46]. In 1954, first patients were treated with proton beam therapy at the Lawrence Berkeley Laboratory in Berkeley, USA. Commercial proton beam delivery system became available in 2001 [NZ15].

The ability to deliver a highly conformal and uniform dose distribution to a tumour region in the patient is the central motivation for proton beam therapy and its potential superiority over conventional photon therapy. The energy loss of high-energetic protons traveling through matter, that is described by the Bethe-Bloch formula, is mainly due to ionisation of the target material's atoms and leads

to a characteristic rise of the deposited dose with a peak immediately before the particles come to rest. This is commonly illustrated in percentage depth dose curves, which are called Bragg curves, with a prominent Bragg peak at the maximum range of the protons. The shape of this curve is caused by the energy loss' dependency of the inverse square of the proton velocity, the range is given by the beam energy.

If the target volume is more spacious, the originally mono-energetic proton beam can be modulated and the range of the particle-energy can be widened using attenuators of variable thicknesses, like wedges. Proton beams of different energies, and therefore different Bragg peak depths, can be superimposed to treat the entire volume. The resulting dose deposition is called Spread-Out-Bragg-Peak. Although this techniques still minimises the dose deposition in tissue situated behind the tumour, it increases the exposure of normal tissue in front of the target volume, that is penetrated by the proton beam.

In photon therapy, techniques such as intensity-modulated photon therapy and volumetric arc therapies are used to overcome the disadvantages in comparison to proton beam therapy. However, the advantages of proton therapy in sparing normal tissues never have been more apparent or important [NZ15]. Clinical studies are currently performed to provide evidence for the benefits of proton beam therapy [BAH$^+$17].

The Particle Therapy Cooperative Group (PTCOG) reports that about 150 000 patients were treated by proton beam therapy by the end of 2016 in 71 therapy centres worldwide. As of October 2018, additional 69 facilities are either under construction (44) or in their planning stage (25) [Par18]. These numbers do not include facilities and treatments centres that are using havier ions, such as carbon ions. In Germany, six particle therapy centres are currently operated.

Typical proton beam energies used for clinical applications range from 70 to 250 MeV. The acceleration is mostly done by an isochronous cyclotron, since these machines are considered simple to operate, reliable and can be made compact.

The dose output of a clinical particle therapy machine is determined in monitor unit (MU), which are measured by ionisation chambers, so-called monitor chambers, inside the treatment head of the therapy machine. 100^- are equal to a dose of 1 Gy (= 100 rad), that is delivered with to a water-equivalent phantom that is positioned in the isocentre of the beam. The field size is normalised to 100 mm $\times$ 100 mm. In general, the number of MU are influenced by the beam current and

the particle energy [Ver17].

The range is modulated by a step-wedge profile on a rotating wheel, that is creating a spread out Bragg peak in the target volume[BGK$^+$17]. Other techniques for the longitudinal spread of the deposited dose rely on patient-specific range compensators, made out of low-Z material. The lateral spread on the other hand, is generally realised with two different methods that rely either on physical scattering or electromagnetic scanning [TNB$^+$14].

During **uniform scanning (US)** and **double scattering (DS)** modes, the proton beam is laterally widened by fixed scatterers in the beam paths and the range is modified using a range compensator. The fixed scatterers consist for example of tantalum and Lexan foils, which can be inserted individually into the beam path [BGK$^+$17]. Alternatively, acrylic or brass filters can be used [TNB$^+$14]. Additional dipole magnets can be used to further enlarge the beam field, if necessary. The beam field is then narrowed down to the shape of the target volume by blocking primary protons and secondary particles with variable apertures. These patient-specific apertures (also referred to as collimators) can have thicknesses of about 30 to 60 mm, depending on the beam energy, and are commonly made out of brass. They are added to the nozzle and can have a maximum diameter of about 200 mm.

For the **pencil beam scanning (PBS)** mode, a narrow, Gaussian shaped particle beam is steered across the target field magnetically. A pair of dipole magnets, switching on a time scale of milliseconds, steers the proton beam to the required lateral position, while the longitudinal dose distribution is controlled by the proton beam energy, which is set at the accelerator level [BBG$^+$19, BAH$^+$17]. Spot sizes during PBS are of the size of some mm, depending on the beam energy [PBE$^+$18]. Additionally, the spot weights can be modified during clinical therapies, ranging from 0.04 MU to a few MU [PBE$^+$18]. The step-and-shoot PBS delivery mode is also known as spot scanning mode. Dowdell et al. suggest, that patient-specific apertures may also be beneficial in PBS modes [DCD$^+$].

The high-energetic protons inside the proton beam interact with an atom or nucleus via Coulomb interactions, either with the atomic electrons or the atomic nucleus itself. Alternatively, non-elastic nuclear reactions are possible as well. Although Bremsstrahlung is theoretically possible, it is usually negligible for the proton beam energies used in clinical applications [NZ15]. The Coulomb interactions are causing an almost continuous loss of the kinetic energy for the proton beam, while most of the protons travel in a practically straight line. Although less frequent in general, non-elastic nuclear reactions of protons with atomic nu-

clei have a very crucial impact. By entering the target nucleus, the high-energetic proton can induce the emission of secondary particles from the nucleus, such as protons, deuterons or heavier ions or one or more neutrons [NZ15].

8.1.1. Proton-induced nuclear reactions

During non-elastic nuclear reactions of protons the target nucleus is transformed and secondary particles are produced. Since the primary proton is removed from the beam during this interaction, the therapeutic dose inside the target volume is decreased. This decrease however, is only small and compensated by the additional dose, that is deposited by the newly produced secondary particles. These secondary particles are mostly neutrons, which can have considerable energies depending on the proton beam energy. Secondary protons have a smaller impact on the distribution of the deposited dose and the position of the Bragg peak in a patient [WCR04, NZ15]. The formation and subsequent decay of radioactive nuclei produced during non-elastic nuclear reactions inside a patient are contributing an additional dose of less than 1 % both to the Bragg peak region and the normal tissue outside of the target region [KCQ09].

The nuclear reactions inside a patient may also be used to monitor the dose distribution inside the target volume as well as other beam and patient properties. Both the detection of gamma rays, that are directly emitted during proton-induced reactions or neutron capture reactions, as well as the measurement of annihilation photons, emitted during positron annihilation, are investigated for this purpose [SRP+12, KAC12, MZW+13]. Alternatively, implantable markers can be used for proton range verifications. Depending on the material of the marker, much stronger signal intensities can be obtained during positron-emission tomography (PET) measurements of the patient after proton beam treatment [CIG+13]. The feasibility of gold marker implants, for example, is investigated [Wil04].

If a high-energy proton beam is incident on the beam delivery equipment, the production of secondary neutrons can create significant radiation protection hazards. Additionally, the proton and neutron induced activation of beam line components has to be considered and the exposure of personnel and patients has to be limited. The activation can take place in permanent as well as consumable components, which may then pose a potential radiation safety issue. Within per-

manent components of the facility considerable amounts of radioactivity can be accumulated during years of continuous operation [Num07, Pel11, WWL+16]. Prominent examples of consumable materials in proton therapy centres are the patient specific range compensators and apertures.

In range compensators, which are made out of low-Z material (i.e. hydrogen, carbon and oxygen), the amount of long-lived radionuclides that can be produced is limited. Radionuclides such as ^{11}C and ^{15}O have half-lives of 20.3 min and 2.04 min, respectively. Additionally, the cross sections for the production of these radionuclides are relatively small.

Patient specific apertures, that are used during scattered and US modes, are commonly made from brass, which is generally composed of the high-Z elements copper, zinc and lead. While brass is used due to its efficient stopping power and benefits during mechanical handling, the contained elements enable a large number of possible activation products Since the involved radionuclides are potentially having long half-lives, these devises are generally considered a radiation hazard and have to be stored until the disposal is safe. At the Indiana University Health Proton Therapy Center (IUHPTC) for example, about 2000 patient specific devises are used per year and stored for at least four month after the end of the patient's treatment [WEDJ14]. About 25 % of the apertures require storage of six months or more before disposal.

B. Thomadsen et al. provide an extensive review about the potential hazards due to radioactivity that is induced during radiotherapy, covering not only proton beam therapy but also photon therapy and neutron facilities [TNB+14].

8.1.2. West German Proton Therapy Centre Essen

The West German Proton Therapy Centre Essen (WPE) uses a *IBA ProteusPlus* facility (IBA PT, Louvain-la-Neuve, Belgium). Protons are accelerated with an isochronous cyclotron and and guided into one of four treatment rooms, equipped with nozzles either for PBS or US [BGK+17] The three gantry rooms (GTR) and one fixed-beam treatment room (FBTR) are used for the treatment of about 500 patients per year. Figures 8.1 and 8.2 show exemplary pictures of a treatment room and a treatment head with nozzle within a *IBA ProteusPlus* facility.

At the output of the cyclotron, the proton energy is at the maximum of about 228 MeV [BBG+19]. With a wheel-mounted wedge, the kinetic energy of the protons can be reduced again until the desired value is reached. This so-called en-

Figure 8.1.: Exemplary treatment room for the IBA ProteusPlus facility [Ion].

Figure 8.2.: Close up of the treatment head inside the IBA ProteusPlus facility [Ion].

ergetic selection system (ESS) can reduce the proton energy down to 100 MeV [PBE+18] The wedge is followed by analysing magnets and energy slits as well as monitor chambers which are located at the nozzle entrance to check the beam-centring. An additional pair of monitor chambers is located close to the nozzle exit for the measurement of the beam spot position and width. The nozzle is evacuated up to a distance of 500 mm from the isocentre to limit the broadening of the beam through scattering [BBG+19]. A universal nozzle treatment head can be used to deliver fields in single scattering (SS), DS or US mode, which is realised by a fixed scatterer, a fast spinning range modulator wheel, and a contoured scatterer.

8.1.3. Monitor reaction cross sections

The fluence and dose distribution of a proton beam field can be monitored using secondary radiation induced in monitoring foils. The production of ^{11}C in carbon containing materials for example, is used to reconstruct the proton fluence [Nic]. Alternatively, the formation of ^{22}Na and ^{24}Na on aluminium foils can be used as monitor reactions. Both materials, ^{nat}C as well as ^{nat}Al, are therefore regarded as reference materials for proton beam facilities [BBG+19].

Hence, accurate values of the involved cross sections for the formation of the above mentioned radionuclides are required. Existing monitor reaction cross section measurements are either relatively inaccurate or not performed for the beam energies employed for proton therapy [BBG+19]. The short distance of about 40 km, between the clinical proton therapy facility WPE and the low-background high-resolution gamma ray spectrometer of the DLB, is enabling accurate measurements of the relatively short-lived radionuclides involved. A

publication, co-authored by the author of this work, is currently submitted for publication. Therein, the initial motivation, the methodology and the results of these measurements are discussed in more detail [BBG+19]. The following paragraphs are presenting a brief overview of this work.

Graphite and aluminum sheets with physical thicknesses of 1 and 2 mm are used as target materials. The materials are of very high purity, since impurities can negatively influence both the irradiation and the subsequent gamma spectrometric measurement and produce inaccurate results. A uniform, quasi-monoenergetic proton field with lateral dimensions of F_f =100 mm × 100 mm is applied in PBS mode. The field dimensions are chosen larger than the lateral sizes of the target sheets to ensure the uniform activation of the targets. Irradiation times range between 60 and 120 s for the different fields, that are applied with beam energies of 100.1 MeV and 180.6 MeV, respectively.

Directly after the irradiation the samples are transported to the DLB and measured for different time periods to obtain the specific activities of the radionuclides under investigation. The analysis is performed using the standard software tools discussed in Section 4.7. Decay corrections are included according to Equation (2.2) and Equation (2.4) to correct for the decay between irradiation and spectrometric measurement as well as during the measurement. Subsequently, the integral production cross sections are determined with:

$$\sigma = \frac{A_0 \, F_f \, M_i}{\lambda \, N_A \, m \, N_P \, k_{us}}. \tag{8.1}$$

A_0 denotes the activity at the reference time ($t = 0$), which is set to the middle of the irradiation time interval. The size of the proton field is given by F_f, the molar mass of the target material by M_i. λ denotes the decay constant of the radionuclide under investigation with $\lambda = \frac{\ln 2}{T_{1/2}}$ and N_A the Avogadro constant. The mass of the target is given by m, the number of incident protons is given by N_P and k_{us} denotes a correction factor for upstream scattered particles, that influence the number of primary protons [BBG+19].

The resulting values for different monitor reaction cross sections are presented in Table 8.1. Also included are the mean cross sections obtained from the EXFOR data base, which is a library for the exchange of experimental nuclear reaction data coordinated by the IAEA Nuclear Data Section [SOM+17]. Since the available data points are scattered, the minimum and maximum values are listed in the table.

Table 8.1.: Experimental results of the activation cross sections on carbon and aluminum targets. E_P refers to the proton beam energy in the laboratory frame. The standard uncertainties (k = 1) are given with systematic (u_σ(sys.)) and statistical (u_σ(stat.)) uncertainties. The literature cross sections, extracted from the EXFOR [SOM+17] database, are given as mean with minimum/maximum values [SOM+17, ZP18]. (Table adapted from [BBG+19].)

Reaction	E_P [MeV]	σ [mb]	u_σ(sys.) [mb]	u_σ(stat.) [mb]	σ_{EXFOR} (min/max) [mb]
$^{nat}\text{C}(p,\text{x})^{11}\text{C}$	100.1	70.2	1.0	0.2	65.0 (61.3/70.2)
$^{nat}\text{C}(p,\text{x})^{7}\text{Be}$	100.1	15.9	0.3	0.6	14.3 (11.6/17.5)
$^{27}\text{Al}(p,\text{x})^{22}\text{Na}$	100.1	19.9	0.3	0.3	20.6 (18.3/26.9)
$^{27}\text{Al}(p,\text{x})^{24}\text{Na}$	100.1	11.48	0.15	0.03	11.1 (10.0/11.9)
$^{27}\text{Al}(p,\text{x})^{7}\text{Be}$	100.1	1.13	0.02	0.04	1.05 (0.86/0.99)
$^{27}\text{Al}(p,\text{x})^{22}\text{Na}$	180.6	16.77	0.22	0.24	16.2 (16.1/16.4)
$^{27}\text{Al}(p,\text{x})^{24}\text{Na}$	180.6	11.6	0.27	0.03	9.8 (-)
$^{27}\text{Al}(p,\text{x})^{7}\text{Be}$	180.6	1.45	0.02	0.04	1.46 (-)

Overall agreement is achieved between the obtained results and the values reported in the literature. While the cross section for the $^{nat}\text{C}(p,\text{x})^{11}\text{C}$, for example, is comparable to the upper end of the scattered data from the literature, other reaction, e.g. $^{27}\text{Al}(p,\text{x})^{22}\text{Na}$, are lower than the mean cross section found in the EXFOR data base. This disfavours any systematical errors during the experiments [BBG+19]. Reactions into ^{7}Be, although not used for beam monitoring, provide an inherent crosscheck for both samples.

8.2. Analysis of the radionulices induced in brass apertures

Patient-specific apertures, that are subject to irradiation with high-energetic proton beams, become radioactive due to non-elastic proton interactions (see Section 8.1.1). Subsequently, these apertures pose a radiation protection risk to personnel or patients when exposed to them. Additionally, the activity levels have to be monitored during storage, long after the end of the irradiation treatment, until the radioactivity is decayed to negligible levels and the safe disposal is possible. However, the available data on quantitative values for the

activation products in bulk material is limited.

M. Faßbender et al. and J. Sisterson, for example, measured the activity induced in thin brass plates after irradiations. Both focussed on long-lived radionuclides and used the obtained results to calculate activation cross sections for several activation products [Sis02, FSLQ97].

A. Cesana et al. used MC simulations to estimate the radioactivity induced in collimators made from bronze. As input for the MC model, a complete treatment plan, consisting of multiple irradiations, was used to obtain the resulting activity levels at the end of the plan. Measurements were performed on a sample about 300 d after the end of the irradiation to validate the MC results for the long-lived radionuclides produced inside the bronze material [CMS10].

The overall activity induced in stacked brass plates as well as 12 mm thick brass samples, was measured using Geiger-Müller counter during the studies of H. Lee [LCY+12].

In addition to aperture materials, other components such as monitoring detectors and phantom materials are subject to proton-induced activation as well. T. Hanusova et al. investigated the residual activity of several materials used for commissioning and quality assurance during clinical proton beams [HJN+18].

H. Chen et al. reported on the potential usage of hybrid brass/stainless-steel apertures as an alternative to conventional brass apertures. While featuring similar energy loss properties, the hybrid material would be more cost efficient. It was found, that neutron doses as well as material activation doses are comparable for both materials [CMF+14].

No direct measurements of activation products in brass apertures are reported. HPGe detectors enable gamma spectrometric measurements with superior energy resolution to identify radionuclides based on their emission of characteristic gamma rays. The low-background environment of the DLB enables the direct measurement of short-lived radionuclides with relatively short half-lives. Due to the transport distance between the WPE and the DLB, the measurement procedure is sensitive for radionuclides with half-lives down to a few minutes.

FLUKA MC code

The FLUKA code (Version 2011.2c-4) is used for the simulation of the irradiation with high energetic protons [FSFR05, BCC+14]. A prediction for the activation

products inside the sample as well as an estimation for the ambient dose distribution and its change over time are obtained from these simulations.

FLUKA is developed by the Italian National Institute for Nuclear Physics (INFN) in cooperation with CERN, and designed for the modelling of hadronic interactions. Therefore, FLUKA is used routinely for the design of new beam facilities, the estimation of radiation damage and shielding activation, the prediction of residual dose rates and planing of waste disposal [BCC+14]. This range of applications is enabled by the calculation of the particle interactions and the tracking of their propagation through complex geometries, which are handled by FLUKA's Combinatorial Geometry (CG) package.

FLUKA's capabilities in predicting the production of radioactive nuclei are regularly benchmarked with proton and ion accelerator experiments [CMS10, BCC+14]. The code is also used, for example, for the calculation of the dose distribution induced in patients and in facility components of clinical proton beam facilities [WWL+16].

During this work, the sample geometries and compositions are implemented as well as the beam parameters, i.e. the beam current, the particle energy and the irradiation time, according to the conditions during the irradiation procedures. Finally, virtual detector volumes are set, in order to obtain the radionuclides produced including their relative activities and the ambient dose at pre-defined points in time.

Analysis procedure

Acquired gamma ray spectra of irradiated brass samples are analysed according to the DLB standard procedure described in Section 2.2.4. Radionuclides are identified due to their characteristic gamma ray energies and subsequently evaluated to obtain average net count rates and specific activities. However, due to the large number of active nuclei, that is produced during the irradiation, the risk of interfering peaks from different radionuclides has to be considered. Because of the relatively high activity of the samples at the beginning of the measurement, RCS effects have to be taken into account and analysis time windows have to be adapted for certain radionuclides. In addition to the identification based on the characteristic gamma ray energy, all of the investigated peaks are also analysed with regards to their decay over time. Thereby, the half-life of a peak can be used as a second indicator of the corresponding radionuclide and peak interferences can be avoided. For all of the identified radionuclides, the decay during the measurement is corrected based on Equation (2.4).

8.2.1. Irradiation with 226 MeV proton beam

A brass sample is provided by the workshop of the WPE and made of an alloy composed of copper (58 %), zinc (39 %) and lead (3 %). Comparable compositions are reported for apertures, which are used in other proton therapy facilities [TNB+14]. The cylindrically shaped sample is 25.1(1) mm in height and 71.0(1) mm in diameter and has a mass of 833.5(5) g, which is corresponding to a density of 8.39(5) g/cm^3. This geometry is chosen to represent the bulk material of aperture plates used during proton therapy, while also efficiently utilising the space inside the DLB's sample chamber to maximise the detection efficiency.

226.7 MeV protons are used to irradiate the sample, which is placed at the isocentre of a 102.5 mm $\times$ 102.5 mm field. The PBS mode is used to irradiate the sample with a quasi-monochromatic ('pristine') proton field, that consists of 41 $\times$ 41 individual beam spots. During the irradiation time of 11 s, 67.2 MU are applied, which correspond to a number of 3.88×10^9 protons incident on the sample. The correlation between MUs and fluence was investigated by N. Verbeek [Ver17]. Since the irradiation time is relatively short, compared to the half-lives of the radionuclides under investigation, it will be neglected during the following analysis. The reference time t_0 is given by the end of the irradiation and all activities A_0 are calculated according to this reference time.

Shortly after the irradiation, the activated sample is placed inside a securable container and transported to Dortmund for the gamma spectrometric measurement in the DLB. Dose rate meters are used to measure the ambient dose rate of the sample and ensure safe transport conditions. While the transport via car takes about 30 min, the time between the end of irradiation and start of the DLB measurement is 42.95 min.

The sample is continuously measured for about 635 h. Individual run times during this time are adjusted from 300 s to 900 s and finally to 3600 s, according to the changes in the count rate.

In Figure 8.3, three spectra of the activated brass sample are presented, that are acquired during the measurement with the DLB. It can clearly be seen, that the overall count rate, thus the sample's activity, is decreasing considerably over the different parts of the measurement. The different half-lives of the involved radionuclides cause the rapid decay of certain peaks (e.g. between 500 keV and 800 keV), while other gamma lines become visible at later times of the measurement when the continuum is decreased and more counts are

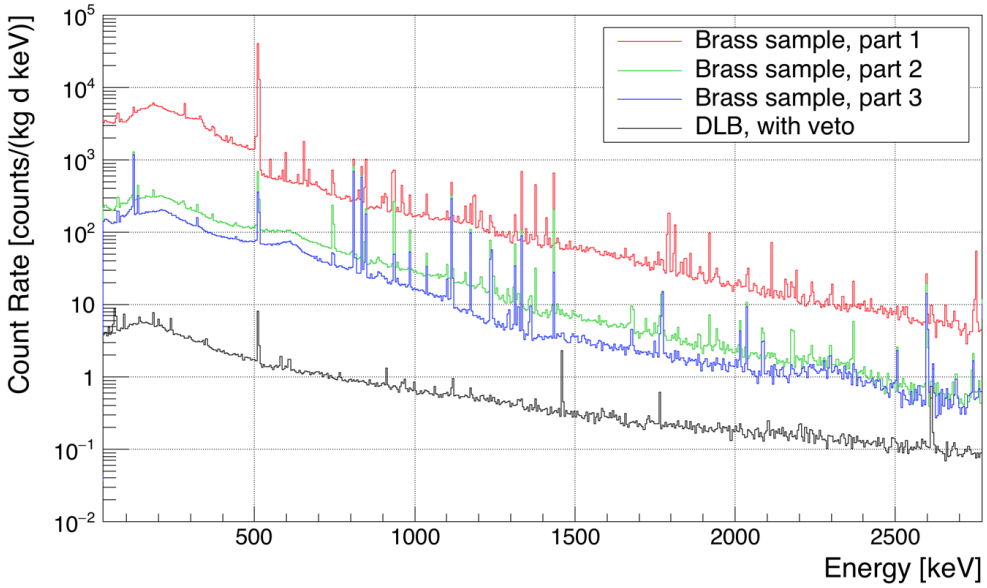

Figure 8.3.: Weekly spectra of the brass sample activated due to the irradiation with 226 MeV protons. Shown is the average count rate per day during the first 82 h ('part 1', red curve), during the next 176 h ('part 2', green curve) and during the last 377 h ('part 3', blue curve). The residual background spectrum of the DLB is shown for comparison in the black curve. The counts are normalised to the germanium crystal mass of 1.247 kg.

accumulated during the measurement time. Prominent example for the latter effect is ^{60}Co with gamma lines becoming visible at 1173 keV and 1332 keV and the summation peak at 2505 keV. Although all spectra contain count rates well above the background spectrum, which is also shown for comparison in Figure 8.3, PBC is performed to consider any counts originally stemming from the detector's background.

Table 8.2 lists the results of the analysis of the brass sample. Overall, about 75 nuclides are investigated, of which about on third results in upper limits for the specific activities, i.e. no evidence for a peak was found with 95 % C.L. (see analysis standards in Section 2.2.4). Listed here are the most active radionuclides, as well as the most long-lived radionuclides, that dominate the overall activity after a few days of decay. The activity levels that are determined for the reference time, i.e. the end of the irradiation, are denoted with A_0. Additionally, the table lists the activity levels at the time of the beginning of the measurement with the DLB. The decay of certain short-lived radionuclides can clearly be seen, while long-lived radionuclides remain practically at the same activity. The shortest lived radionuclide yielding a net count rate above the DT is ^{61}Cu, which has a half live

Table 8.2.: Resulting specific activities for the brass sample after irradiation with a 226 MeV proton beam at WPE. Listed are the most active radionuclides that yield count rates above the DT. Additionally, some prominent long-lived radionuclides are listed, that dominante the overall activity after a few days of decay. The specific activity at the end of irradiation is denoted with A_0, the activity at the time of arrival at the DLB is denoted with A_{dlb}.

Nuclide	Half-life [s]	A_0 [Bq/kg]	A_{dlb} [Bq/kg]
^{63}Zn	2300	4425(232)	2147(112)
^{60}Cu	1422	2976(130)	923.6(405)
^{61}Cu	12 100	1291(136)	1125(118)
^{64}Cu	45 721	284.9(208)	274.7(201)
^{49}Cr	2538	182.1(251)	94.56(1305)
^{196}Pb	2220	127.1(206)	60.08(976)
^{56}Mn	9280	117.0(25)	97.84(207)
^{199}Pb	5400	91.56(1081)	67.28(794)
^{62}Zn	33 094	87.44(473)	83.15(450)
^{198}Pb	8640	71.06(365)	58.61(301)
^{58}Co	6.12×10^6	4.79(15)	4.79(15)
^{65}Zn	21.1×10^6	3.70(19)	3.70(19)
^{54}Mn	26.9×10^6	3.16(10)	3.16(10)
^{203}Hg	4.03×10^6	1.60(7)	1.60(7)
^{60}Co	166×10^6	0.66(3)	0.66(3)

of only 1422 s. This time elapsed nearly twice during the transport of the sample [NNDCN18].

Comparison with FLUKA simulations

The results, that are determined with the DLB, can now be compared with predictions that are given by FLUKA simulations. 1×10^9 protons are simulated to obtain results with small statistical uncertainties for the produced radionuclides. According to FLUKA, about 500 nuclides are produced inside the brass sample, when only activities of more than 1 Bq are considered. Most of these radionuclides are very short-lived and therefore not measurable after the transport time.

Table 8.3.: Most active radionuclides predicted by the FLUKA simulation in comparison to the results obtained from the DLB measurement. All activities are given for the reference time. The uncertainties for the fluka results (A_{FLUKA}) are all well below 1 % and not included here. DLB results (A_0) are given with standard uncertainty (k=1) or as upper limit with 95 %C.L..

Nuclide	$T_{1/2}$ [s]	A_{FLUKA} [Bq]	A_0 [Bq]
^{62}Cu	580	51 865	<107 994
^{59}Cu	82	5422	-
^{58}Cu	3.2	5062	-
^{63}Zn	2300	3757	3625(193)
^{66}Cu	307	3349	-
^{61}Zn	147	2614	-
^{60}Cu	1422	2474	2480(108)
^{64}Ga	158	2459	-
^{57}Mn	85	2006	-
^{63}Ga	32	1628	-
^{63}Co	94	1426	-
^{61}Cu	12 120	1162	1077(113)
^{53}Fe	511	1003	<2037

The most active radionuclides according to the FLUKA simulation are listed in Table 8.3. Although most of the predicted radionuclides are not detectable due to the elapsed time after their production, the three results obtained show good agreement with the predictions. Two additional radionuclides, among them the most active radionuclide, are identified in the spectra but only yield upper limits due to a insufficient counts. However, these upper limits are not in contrast to the predictions.

Table 8.4 contains the FLUKA results for the most active radionuclides at the time of arrival at the DLB. The results obtained from the measurement are shown in comparison. Discrepancies can only be observed for ^{196}Pb and ^{64}Cu, where in both cases the measured activity is lower than the prediction.

The table also includes the longest lived radionuclides contained in the sample. In comparison with the DLB results, larger discrepancies occur for these radionuclides. Although all of the predicted radionuclides are present can be evaluated,

Table 8.4.: Comparison between the results of the measurement and FLUKAs predicted radionuclides for the irradiation with 226 MeV protons. All activities are given for the reference time. The uncertainties for the fluka results (A_{FLUKA}) are all well below 1 % and not included here. DLB results (A_0) are given with standard uncertainty (k=1) or as upper limit with 95 %C.L..

Nuclide	$T_{1/2}$ [s]	A_{FLUKA} [Bq]	A_0 [Bq]
^{63}Zn	2300	3757	3625(193)
^{60}Cu	1422	2474	2480(108)
^{61}Cu	12 100	1162	1077(113)
^{53}Fe	511	1003	<2037
^{197}Pb	486	817	<2005
^{194}Pb	642	483	<228
^{196}Pb	2220	356	106(17)
^{64}Cu	45 721	310	237(18)
^{60}Co	166×10^6	0.008	0.550(25)
^{54}Mn	26.9×10^6	0.20	2.63(8)
^{57}Co	23.5×10^6	0.78	6.45(15)
^{65}Zn	21.1×10^6	0.34	3.08(16)
^{46}Sc	7.24×10^6	0.005	0.051(5)
^{56}Co	6.67×10^6	1.0	1.28(2)
^{58}Co	6.12×10^6	1.3	3.99(12)
^{59}Fe	3.84×10^6	0.05	0.134(7)

the determined activities are larger than the predictions by factors between 1.3 and 68. The discrepancies seem to be correlated with the nuclides half-lives. Several measurements in the past however, have shown that the DLB is very well suited for the detection of activity levels relevant here [Ned14, Nit14].

8.2.2. Irradiation with 100 MeV proton beam

A second brass sample is prepared by the workshop of the WPE, consisting of the same brass alloy. The sample has dimensions of 32.9(1) mm in height and 69.8(1) mm in diameter and is cylindrically shaped. The mass of 1061.9(5) g corresponds to a density of 8.43(4) g/cm^3.

The sample is irradiated at the WPE with a 100 MeV proton beam under the

same field conditions as above. 67.2 MU are applied during an irradiation time of 11 s. This corresponds to a number of 1.97×10^9 protons incident on the sample [Ver17].

The measurement of the sample with the DLB is started 45.1 min after the end of the irradiation. Overall, the samples is measured for about 237 h, with run times of 300 s each at the beginning of the measurement and 3600 s at the end.

100 MeV protons have a range of about 77 mm in water, compared to a range of 317 mm in water for 226 MeV protons [MBC17]. The CSDA of 100 MeV protons in copper is $11.85\,\mathrm{g/cm^2}$, which can be transformed to a range of 13.3 mm (Note that copper is used as substitute here.) [MBC17]. Geant4 simulations yield a maximum penetration depth of $16.5(33)$ mm for 100 MeV protons in brass.

The radionuclides inside the sample of 33 mm thickness can therefore not be assumed to be uniformly distributed. Instead, the activation products are concentrated within the first half (in beam direction) of the sample. They are approximated as uniformly distributed within this section of the sample, although the actual production rates of individual radionuclides depend on the energy-dependent cross sections for the (p, x)reactions, while the energy of the proton beam changes with depth, according to the Bragg peak curve.

It should be noted that the radionuclides in the first sample, activated with 226 MeV protons, are assumed to be uniformly distributed, following the constant energy deposition of the protons within the sample. MC simulations based on FLUKA and Geant4 confirmed this.

Similar radionuclides are found in the spectrum of the second sample and subsequently evaluated. Table 8.5 shows the results in direct comparison with FLUKA predictions, which are obtained from the simulation of 1×10^9 protons. Overall, good agreement between the measurement and the FLUKA simulation is achieved. The fact, that generally less activity is produced inside the second sample is simply given by the smaller volume, when only half of the sample is considered. Otherwise, the amount of active nuclei produced depends on the individual cross section.

In contrast to the previous measurement, it is possible to obtain a net count rate exceeding the DT for ^{62}Cu. The uncertainty however, is large due to the limited number of counts detected. Nevertheless, the result matches the simulation very well. This detection is remarkable, since, due to the half-life of ^{62}Cu of only 580.4 s, the activity is already decreased by a factor of 25, when the sample

arrives at the DLB and the measurement is started. Without the low-background conditions provided by the DLB's shielding and muon veto, this detection would not been possible.

Table 8.5.: Comparison between the results of the measurement and FLUKAs predicted radionuclides for the irradiation with 100 MeV protons. All activities are given for the reference time. The uncertainties for the fluka results (A_{FLUKA}) are all well below 1 % and not included here. DLB results (A_0) are given with standard uncertainty (k=1) or as upper limit with 95 %C.L..

Nuclide	$T_{1/2}$ [s]	A_{FLUKA} [Bq]	A_0 [Bq]
^{62}Cu	580.4	26 143	24 618(10683)
^{63}Zn	2300	2512	2725(140)
^{60}Cu	1422	1154	1262(58)
^{61}Cu	12 100	644	673(68)
^{65}Ga	912	433	283(69)
^{53}Fe	511	49.4	<197
^{64}Cu	45 721	126	108(9)
^{62}Zn	33 070	54.9	58.1(58)
^{202}Bi	6156	31.2	30.6(18)
^{61}Co	5936	27.2	30.7(88)
^{60}Co	166×10^6	0.002	0.008(1)
^{54}Mn	26.9×10^6	0.015	0.022(2)
^{57}Co	23.5×10^6	0.194	0.180(7)
^{65}Zn	21.1×10^6	0.217	0.253(10)
^{56}Co	6.67×10^6	0.173	0.144(4)
^{58}Co	6.12×10^6	0.379	0.784(25)
^{59}Fe	3.84×10^6	0.006	0.024(2)

Table 8.5 also lists the long-lived radionuclides produced in the second sample due to the irradiation with 100 MeV protons. In contrast to the first sample, the deviations between measurement and simulation are smaller here. In fact, no systematic error is visible. It remains unclear why the long-lived radionuclides within the first sample showed these large discrepancies.

8.2.3. Estimation of the ambient dose

Patient-specific apertures are handled by the personnel of the proton beam facility shortly after the end of irradiation, since the apertures are changed depending on the beam direction or when the treatment of one patient is completed and preparations for the next patient are done. The exposure to this radioactivity is a critical issue for radiation protection and one of the reasons for the personal dose monitoring of the facility's staff.

The measurements and MC simulations, which are discussed above, can be used to estimate the ambient dose emitted by the irradiated samples.

The absorbed dose D is given by the energy E that is absorbed by a mass m. It is measured in units of 1 Gy=1 J/kg. For the equivalent dose H, the effects on the human body are considered by taking the biological effectiveness of the radiation as well as its type and energy into account. The radiation weighting factor W_i is therefore introduced, that depends of the type of radiation i. It ranges between 1 for gamma rays, x-rays and beta particles and 20 for alpha radiation. Protons are considered with a weighting factor of 2. The equivalent dose is given in units of [Sv] and calculated via

$$H = \sum_i D_i W_i. \tag{8.2}$$

Due to the elemental composition of brass, most of the radionuclides produced are beta decaying nuclides. These decays are then often accompanied by the emission of gamma rays. Due to the strong self-absorption inside the brass sample, the ambient dose is mainly induced by these gamma rays.

In Figures 8.4 and 8.5 the FLUKA results for the ambient dose distribution for the first sample after the irradiation with 226 MeV protons are shown. Both figures feature visualisations of the xy-plane in beam direction. The activation of the ambient air can clearly be seen, as Figure 8.4 shows the dose distribution 1 s after the end of the irradiation. This dose however, decays quickly, since most of the produced radionuclides are short-lived, such as ^{15}O, which has a half-life of 122.2 s [NNDCN18]. In Figure 8.5, the dose is mainly induced by the brass aperture itself, since 43 min have elapsed since the end of the irradiation. The sample's surface activity has decreased considerably from about 100 µSv/h to about 2 µSv/h. This is consistent with previously performed measurements of the activity of irradiated brass at the WPE, that are reporting a relative decline of

the activity to about 1.2 % 60 min after the irradiation [Muk12].

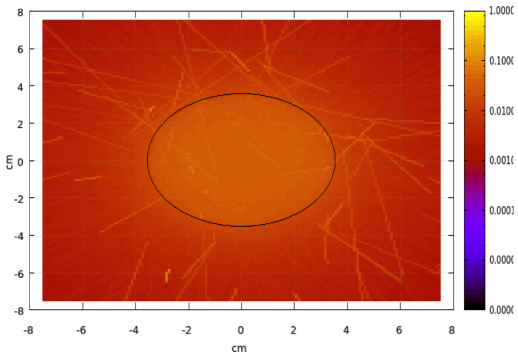

Figure 8.4.: FLUKA output for the ambient dose distribution 1 s after the end of irradiation. Residal activation of the air around the cylindrical sample can be seen. Shown is the side of the sample that faced the proton beam during irradiation.

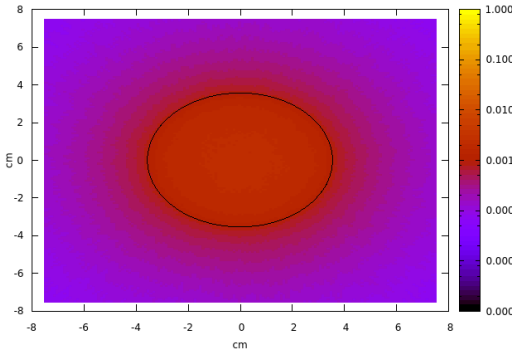

Figure 8.5.: FLUKA output for the ambient dose distribution 43 min after the end of irradiation, at the start time of the measurement in the DLB. The short-lived radionuclides of the ambient air have decayed.

The results obtained from the measurement of the first activated brass sample (compare Table 8.2) are used as input for additional MC simulations of the ambient dose distribution. Geant4 is used to determine the absorbed dose D, that is emitted by the sample. This can be converted into a equivalent dose rate using Equation (8.2). At the end of the irradiation an estimation of the surface dose rate of 38.9 µSv/h is obtained. Since not all produced radionuclides are detected during the DLB measurement, this result is at least a factor of two lower than the FLUKA predictions.

43 min after the irradiation, the Geant4 simulations yield a surface dose rate of 2.4 µSv/h, which is in agreement with the aforementioned value. Dose rate meter measurements at the DLB resulted in a dose rate of about 0.28 µSv/h. However, the limited solid angle, that is covered by the measuring device, has to be considered. Modelling of the measurement conditions in both MC codes yields dose rates of $<$0.5 µSv/h (FLUKA) and 0.33 µSv/h (Geant4), respectively. Both values are in relatively good agreement with the measurement, considering the involved uncertainties.

After a decay time of 24 h, the dose rate is decreased to about 0.032 µSv/h, less than 1 % of the initial dose rate. A comparable reduction in dose rate is reported

for previous activity measurements on activated brass at the WPE, with 0.7 % after 24 h [Muk12].

B. Thomadsen et al. report on short-term dose rate measurements on a 'typical' brass aperture irradiated with 208 MeV protons. Immediately after the irradiation, a surface dose rate of 1.8 mSv/h was obtained. It decreased to 0.8 mSv/h after 15 min and further to 0.17 mSv/h after 60 min [TNB$^+$14]. Although the absolute values are about an order of magnitude larger, the relative decrease is comparable to the measurements in this work. The size of the activated aperture used by Thomadsen et al. is unknown. However, based on common brass apertures sizes (compare Section 8.1), a factor of 10 to 15 between both measurements is plausible.

During routine operations in proton beam therapy facilities, patient-specific apertures are re-used several times over the course of a patient's treatment plan. Typical treatment plans consist of 5 irradiations per week for a time span of 5 to 6 weeks [TNB$^+$14, CMS10]. The accumulation of activity, especially for the long-lived radionuclides, has to be considered. Thomadsen at al. project an annual equivalent dose of about 100 µSv/h for deep body and 1.5 mSv/h for extremities for personnel. This is consistent with the monthly reporting of personnel monitory (10 µSv) for a proton beam therapy facility at the Indiana University Health Proton Therapy Center [TNB$^+$14].

9. Summary

The DLB is a highly sensitive gamma ray spectrometer within a low-background environment, that enables the measurement of traces of radioactivity with high precision. An outer shielding provides an overburden of 10 m.w.e. and houses the inner shielding, which is featuring a neutron absorber inside a massive lead shielding. Due to the employment of a muon veto detector, an enormous reduction of background radiation is achieved for the HPGe detector. Sensitivities well below 1 Bq/kg are possible. Depending on the sample geometry and measurement time, detection limits below 1 mBq/kg have been achieved.

During this work, the muon veto detector is upgraded with plastic scintillators of 50 mm thickness and thereby completed. Before their installation, the scintillation detectors are characterised with regards to their cosmic muon detection capabilities and signal detection efficiency.

An extensive measurement of the background results in a residual background count rate of $1.855(3)\,\mathrm{counts}/(\mathrm{kg_{Ge}min})$ between 40 keV and 2700 keV. This marks the lowest background level achieved for the DLB since the design and commissioning of the facility in 2009. It is comparable to the background level of other facilities, which are situated at depths of 30 or 110 m.w.e. (compare Table 6.5).

The residual background spectrum is evaluated in great detail. Peaks are identified and contaminations inside the detector system are estimated based on the detected count rates. Particular attention is paid to the cosmic-muon induced background components. The directly muon-induced component is evaluated based on MC simulations, which are performed using a newly implemented cosmic muon particle generator. These simulations are based on the work of M. Gerhardt [Ger16]. Contributions from contaminated and activated detector components and shielding materials are used for a preliminary model of the residual background. The information obtained by these studies can be used to further improve the DLB by the selective elimination of these contributions. Otherwise the data can help during the construction of new detector systems.

In cooperation with the WPE several metal samples are irradiation with a high energetic proton beam, that is usually used for clinical proton beam therapy. Monitor reaction cross sections are determined with high accuracy, which will improve the routine beam monitoring in proton beam facilities.

The activation of brass apertures poses a radiation protection risk for personnel and patients. During this work, two samples are irradiated and analysed. The results provide the first direct and quantitative measurement of short-lived radionuclides, which are produced in brass. The remarkable low background environment of the DLB enables the measurement of radionuclides with half-lives of less then 10 min. Good overall agreement is achieved between the results and FLUKA simulations, especially for the highly active, but short-lived radionuclides. However, the measurement procedure can be expanded to more energies and sample sizes to provide better data availability. Additional measurements, long after the irradiation, are advised to check for the discrepancies between the measurement and FLUKA simulations.

The ambient dose rate caused by an activated brass sample is estimated using different MC codes and instruments. Based on the very detailed data, obtained from the measurements, calculations can now be performed, which consider a complete treatment plan, i.e. the re-usage of brass apertures which results in the accumulation of radioactivity.

A. Vertical intensity of cosmic muons

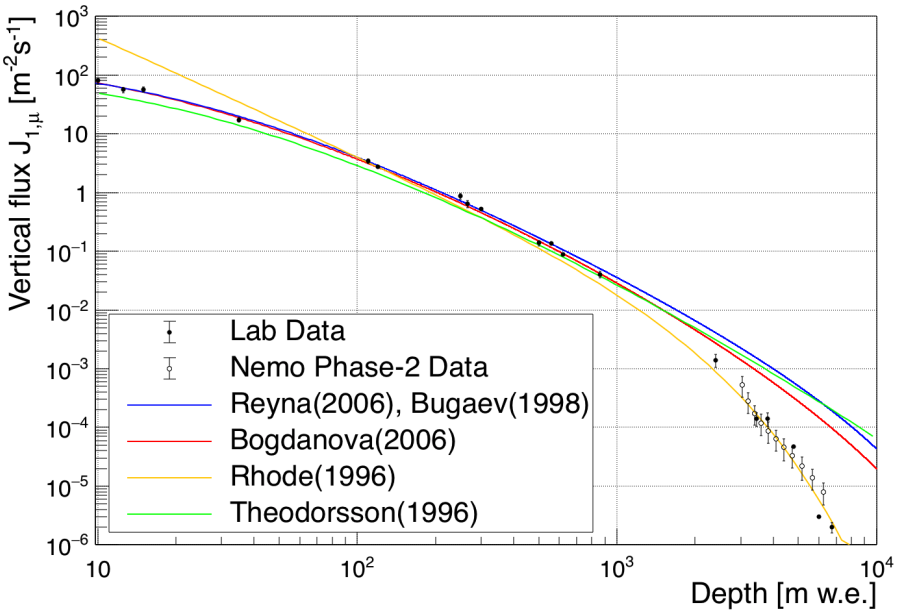

Figure A.1.: Depth intensity relation for cosmic muons between 1 m.w.e. and 10 km.w.e.. For references of the displayed experimental data of different underground laboratories see Table 6.5 and [AAdA$^+$17, ABB$^+$] as well as [W$^+$13, AAA$^+$09]. Additional experimental data is taken from Nemo Phase 2 [AAA$^+$15]. The parameterisation of the vertical flux of cosmic muons by Rhode et al. is shown with parameters that are obtained with Fréjus data between depths of 4 km.w.e. to 12 km.w.e. [R$^+$96]. Neutrino induced muons become dominant below depths of 13 km.w.e. and muon fluxes of about 10^{-9} muons/m^2/s.

B. Peaks in the background spectrum

Table B.1.: Peaks found in the residual background spectrum of the DLB. Net count rates, including their standard uncertainties ($k = 1$), are given in counts per day (counts/d) if the decision threshold is exceeded. Otherwise, upper limits are given with 95 % coverage probability 'BE' denotes binding energy. Energy and emission probability data is taken from [NNDCN18]. 'contam.' denotes the contamination fo detector or shielding material. Radionuclides produced by cosmogenic activation are labelled with 'activ.' n scatter ('scat.') or capture ('capt.') reactions are labelled accordingly.

Energy [keV]	Net count rate [counts/d]	Nuclide (Chain) / Reaction	Intensity / Half-life	Remarks
46.54	8.28(49)	^{210}Pb (^{238}U)	$p = 4.25\,\%$	Pb impurity
50.13	<0.41	^{227}Th (^{235}U)	$p = 8.2\,\%$	contam.
53.44	2.31(36)	^{72}Ge(n, γ)^{73m}Ge	$T_{1/2} = 499\,\mathrm{ms}$	n capt. on Ge
59.3	2.68(42)	unidentified		
63.30	4.40(60)	^{234}Th (^{238}U)	$p = 3.75\,\%$	contam.
66.72	22.39(86)	^{72}Ge(n, γ)^{73m}Ge	$T_{1/2} = 0.499\,\mathrm{s}$	n capt. on Ge
68.75	<0.105	^{73}Ge(n, n'γ)^{73*}Ge	$T_{1/2} = 1.74\,\mathrm{ns}$	n scat. on Ge, asym.
72.81	<0.72	Pb $K_{\alpha 2}$		X-ray
74.82	1.78(35)	Bi $K_{\alpha 2}$		X-ray
74.97		Pb $K_{\alpha 1}$		X-ray
77.11	1.64(037)	Bi $K_{\alpha 1}$		X-ray
84.95	<0.75	Pb $K_{\beta 1}$		X-ray
87.35	<1.16	Bi $K_{\beta 1}$		X-ray
87.58		Pb $K_{\beta 2}$		X-ray
92.38	16.05(64)	^{234}Th (^{238}U)	$p = 2.18\,\%$	contam.
92.80		^{234}Th (^{238}U)	$p = 2.15\,\%$	contam.
112.1	<1.01	^{234}Th (^{238}U)	$p = 0.21\,\%$	contam.
122.06	<0.98	^{57}Co	$p = 85.5\,\%$	Cu activ.
129.06	<0.305	^{228}Ac (^{232}Th)	$p = 2.5\,\%$	contam.

Continued on next page.

Table B.1.: (Continued.)

Energy [keV]	Net count rate [counts/d]	Nuclide (Chain) / Reaction	Intensity / Half-life	Remarks
136.47	<0.84	^{57}Co	$p = 10.7\,\%$	Cu activ.
136.47		^{56}Fe(n, γ)^{57}Fe	$T_{1/2} = 8.7\,$ns	n capt. on Fe
139.68	5.46(51)	^{74}Ge(n, γ)^{75m}Ge	$T_{1/2} = 47.7\,$s	n capt. on Ge
143.59	2.70(47)	^{57}Co + Fe BE		Ge activ.
143.77		^{235}U (^{235}U)	$p = 10.9\,\%$	contam.
159.70	1.12(40)	^{76}Ge(n, γ)^{77m}Ge	$T_{1/2} = 52.9\,$s	n capt. on Ge
163.36	<1.20	^{235}U (^{235}U)	$p = 5.08\,\%$	contam.
174.95	<1.11	^{70}Ge(n, γ)^{71m}Ge	$T_{1/2} = 79\,$ns	n capt. on Ge
185.72	15.6(63)	^{235}U (^{235}U)	$p = 57.0\,\%$	contam.
186.01		^{65}Cu(n, γ)^{66}Cu		n capt. on Cu
186.21		^{226}Ra (^{238}U)	$p = 3.56\,\%$	contam.
198.4	6.89(54)	^{70}Ge(n, γ)^{71m}Ge	$T_{1/2} = 20.4\,$ms	n capt. on Ge
205.32	1.20(38)	^{235}U (^{235}U)	$p = 5.02\,\%$	contam.
235.97	0.98(39)	^{227}Th (^{235}U)	$p = 12.6\,\%$	contam.
237.82	12.16(75)	^{65}Cu(n, γ)^{66}Cu	$T_{1/2} = 5.12\,$min	n capt. on Cu
238.63		^{212}Pb (^{232}Th)	$p = 43.6\,\%$	contam.
241.99	1.85(51)	^{214}Pb (^{238}U)	$p = 7.27\,\%$	contam.
256.3	<0.83	^{227}Th (^{235}U)	$p = 6.8\,\%$	contam.
264.44	<0.301	^{76}Ge(n, γ)^{77}Ge	$T_{1/2} = 52.9\,$s	n capt. on Ge
264.66		^{74}Ge(n, γ)^{75}Ge	$T_{1/2} = 82.8\,$min	n capt. on Ge
269.4	1.48(35)	^{223}Ra (^{235}U)	$p = 14.2\,\%$	contam.
270.3		^{228}Ac (^{232}Th)	$p = 3.55\,\%$	contam.
271.2		^{219}Rn (^{235}U)	$p = 11.1\,\%$	contam.
277.37	0.73(32)	^{208}Tl (^{232}Th)	$p = 6.6\,\%$	contam.
278.24		^{63}Cu(n, γ)^{64}Cu	$T_{1/2} = <9\,$ps	n capt. on Cu
283.69	<0.55	^{231}Pa (^{235}U)	$p = 1.65\,\%$	contam.
295.22	2.86(39)	^{214}Pb (^{238}U)	$p = 18.4\,\%$	contam.
323.87	<0.68	^{223}Ra (^{235}U)	$p = 4.06\,\%$	contam.
328.01	0.57(28)	^{228}Ac (^{232}Th)	$p = 3.04\,\%$	contam.
338.32	2.42(33)	^{228}Ac (^{232}Th)	$p = 11.4\,\%$	contam.
351.93	5.84(42)	^{214}Pb (^{238}U)	$p = 35.6\,\%$	contam.
351.93		^{211}Bi (^{235}U)	$p = 13.0\,\%$	contam.
401.7	0.51(25)	^{219}Rn (^{235}U)	$p = 6.75\,\%$	contam.
404.75	<0.52	^{211}Pb (^{235}U)	$p = 3.83\,\%$	contam.

Continued on next page.

Table B.1.: (Continued.)

Energy [keV]	Net count rate [counts/d]	Nuclide (Chain) / Reaction	Intensity / Half-life	Remarks
416.33	<0.65	^{76}Ge(n, γ)^{77}Ge	$T_{1/2} = 11.2$ h	Ge activ.
463.00	0.65(25)	^{228}Ac (^{232}Th)	$p = 4.45$ %	contam.
477.60	0.42(22)	^{10}B(n, α)^{7}Li	$T_{1/2} = 0.07$ ps	n capt. on B
510.74	34.16(72)	^{208}Tl (^{232}Th)	$p = 22.5$ %	contam.
511		annihilation		muonic & contam.
545.51	<0.35	^{76}Ge(n, n$'\gamma$)^{76}Ge	$T_{1/2} = 8.0$ ps	n scat. on Ge, asym.
558.02	<0.276	^{76}Ge(n, γ)^{77}Ge	$T_{1/2} = 11.3$ h	n capt. on Ge
562.93	<0.46	^{76}Ge(n, n$'\gamma$)^{76}Ge	$T_{1/2} = 18.2$ ps	n scat. on Ge, asym.
569.70	<0.70	^{207}Pb(n, n$'\gamma$)^{207}Pb	$T_{1/2} = 130$ ps	n scat. on Pb
583.19	3.56(34)	^{208}Tl (^{232}Th)	$p = 85.0$ %	contam.
595.85	<0.40	^{74}Ge(n, n$'\gamma$)^{74}Ge	$T_{1/2} = 12.4$ ps	n capt. on Ge, asym.
608.35	5.46(34)	^{74}Ge(n, n$'\gamma$)^{74}Ge	$T_{1/2} = 5.4$ ps	n scat. on Ge, asym.
609.31		^{214}Bi (^{238}U)	$p = 45.5$ %	contam.
631.82	<0.33	^{76}Ge(n, γ)^{77}Ge	$T_{1/2} = 11.2$ h	Ge activ.
661.6	<0.61	^{137}Cs	$p = 84.9$ %	contam.
669.62	0.44(20)	^{63}Cu(n, n$'\gamma$)^{63}Cu	$T_{1/2} = 0.2$ ps	n scat. on Cu
691.4	<0.26	^{72}Ge(n, n$'\gamma$)^{72}Ge	$T_{1/2} = 444$ ns	n scat. on Ge, asym.
727.33	1.26(22)	^{212}Bi (^{232}Th)	$p = 6.65$ %	contam.
768.36	0.36(18)	^{214}Bi (^{238}U)	$p = 4.89$ %	contam.
770.66	<0.56	^{65}Cu(n, n$'\gamma$)^{65}Cu	$T_{1/2} = 0.1$ ps	n scat. on Cu
794.94	0.49(19)	^{228}Ac (^{232}Th)	$p = 4.31$ %	contam.
803.10	0.96(21)	^{206}Pb(n, n$'\gamma$)^{206}Pb	$T_{1/2} = 8.3$ ps	n scat. on Pb
810.76	<0.33	^{58}Co	$p = 99.4$ %	Cu activ.
817.87	<0.26	^{58}Co + Fe BE		Ge activ.
834.01	0.40(18)	^{72}Ge(n, n$'\gamma$)^{72}Ge	$T_{1/2} = 3.35$ ps	n scat. on Ge, asym.
834.85		^{54}Mn	$p = 99.9$ %	Cu activ.
840.84	<0.45	^{54}Mn + Cr BE		Ge activ.
843.74	<0.276	^{27}Al(n, n$'\gamma$)^{27}Al	$T_{1/2} = 35$ ps	aluminium activ.
846.77	<0.225	^{56}Co	$p = 99.9$ %	Cu activ.
860.53	0.39(18)	^{208}Tl (^{232}Th)	$p = 12.4$ %	contam.
897.80	0.35(17)	^{207}Pb(n, n$'\gamma$)^{207}Pb	$T_{1/2} = 0.11$ ps	n scat. on Pb
911.20	3.70(29)	^{228}Ac (^{232}Th)	$p = 26.2$ %	contam.
934.06	0.49(18)	^{214}Bi (^{238}U)	$p = 3.10$ %	contam.
968.96	1.59(26)	^{228}Ac (^{232}Th)	$p = 15.9$ %	contam.

Continued on next page.

Table B.1.: (Continued.)

Energy [keV]	Net count rate [counts/d]	Nuclide (Chain) / Reaction	Intensity / Half-life	Remarks
962.06	0.57(21)	^{63}Cu(n, n′γ)^{63}Cu	$T_{1/2} = 0.57$ ps	n scat. on Cu
964.79		^{228}Ac (^{232}Th)	$p = 4.99$ %	contam.
1001.03	1.58(24)	^{234m}Pa (^{238}U)	$p = 0.85$ %	contam.
1014.4	<0.276	^{27}Al(n, n′γ)^{27}Al	$T_{1/2} = 1.5$ ps	n scat. on Al
1037.83	<0.51	^{56}Co	$p = 14.0$ %	Cu activ.
1063.66	0.61(18)	^{207}Pb(n, n′γ)^{207}Pb	$T_{1/2} = 0.81$ s	Pb activ.
1077.34	<0.237	^{68}Ga (^{68}Ge)	$p = 3.23$ %	Ge activ.
1085.19	<0.166	^{76}Ge(n, γ)^{77}Ge	$T_{1/2} = 11.2$ h	Ge activ.
1099.25	<0.215	^{59}Fe	$p = 56.5$ %	iron activ.
1115.55	<0.54	^{65}Cu(n, n′γ)^{65}Cu	$T_{1/2} = 0.28$ ps	Cu activ.
1120.29	2.25(26)	^{214}Bi (^{238}U)	$p = 14.9$ %	contam.
1124.53	<0.42	^{65}Zn + Cu BE		Ge activ.
1173.23	0.97(21)	^{60}Co	$p = 99.8$ %	iron contam., Cu activ.
1238.11	1.81(21)	^{214}Bi (^{238}U)	$p = 5.83$ %	contam.
1238.27		^{56}Co	$p = 66.4$ %	Cu activ.
1291.60	<0.232	^{59}Fe	$p = 43.2$ %	iron activ.
1327.03	<0.50	^{63}Cu(n, n′γ)^{63}Cu	$T_{1/2} = 0.61$ ps	n scat. on Cu
1332.49	1.15(21)	^{60}Co	$p = 99.9$ %	iron impurity, Cu activ.
1377.67	0.43(16)	^{214}Bi (^{238}U)	$p = 3.97$ %	contam.
1407.98	0.39(15)	^{214}Bi (^{238}U)	$p = 2.39$ %	contam.
1412.08	<0.266	^{63}Cu(n, n′γ)^{63}Cu	$T_{1/2} = 1.7$ ps	Cu activ.
1460.82	12.83(41)	^{40}K	$p = 10.5$ %	contam.
1481.84	0.22(12)	^{65}Cu(n, n′γ)^{65}Cu	$T_{1/2} = 0.41$ ps	n scat. on Cu
1547.04	<0.334	^{63}Cu(n, n′γ)^{63}Cu	$T_{1/2} = 0.12$ ps	n scat. on Cu
1620.5	<0.297	^{212}Bi (^{232}Th)	$p = 1.51$ %	contam.
1630.62	0.39(13)	^{228}Ac (^{232}Th)	$p = 1.52$ %	contam.
1764.49	2.84(29)	^{214}Bi (^{238}U)	$p = 15.3$ %	contam.
1771.23	<0.239	^{56}Co	$p = 15.5$ %	contam.
1778.987	<0.268	^{27}Al(n, γ)^{28}Al	$T_{1/2} = 2.25$ min	aluminum activ.
1847.42	0.23(12)	^{214}Bi (^{238}U)	$p = 2.03$ %	contam.
2204.21	0.56(15)	^{214}Bi (^{238}U)	$p = 4.91$ %	contam.
2341.3	<0.159	^{76}Ge(n, γ)^{77}Ge	$T_{1/2} = 11.2$ h	Ge activ.
2614.51	4.58(25)	^{208}Tl (^{232}Th)	$p = 99.8$ %	contam.
2614.53		^{207}Pb(n, γ)^{208}Pb	$T_{1/2} = 16.7$ ps	n capt. on Pb

C. Supervised and co-supervised theses

Carolin Linker: *Gammaspektrometrische Vermessung eines Radiopharmakons in der Dortmund Low Background Facility*, Bachelor's thesis, TU Dortmund, 2015.

Sedef Ibisi: *Untersuchung einer mit Protonen aktivierten Messing-Probe mit der Gamma-Spektroskopie in der DLB*, Bachelor's thesis, TU Dortmund, 2015.

Marcel Gerhardt: *Monte Carlo Simulations of the Muon-induced Background and Completion of the Muon Veto of the Dortmund Low Background Facility*, Master's thesis, TU Dortmund, 2016.

Carolin Weber: *Messung und Simulation der Energiedeposition kosmischer Myonen in organischen Kunststoffszintillatoren*, Bachelor's thesis, TU Dortmund, 2016.

Azad Yazgan: *Gammaspektroskopische Untersuchung einer im Protonenfeld aktivierten Amalgamlegierung und Berechnung der Aktivierungswirkungsquerschnitte an Aluminium und Graphit*, Master's thesis, TU Dortmund, 2017.

Hilda Siregar: *Bestimmung von (p, x)-Wirkungsquerschnitten in Aluminium und Titan mittels Gammaspektroskopie nach Aktivierung in der Protonenstrahltherapie*, Bachelor's thesis, TU Dortmund, 2017.

Anna Lena Borghoff: *Inbetriebnahme einer neuen Auslese-Elektronik für die Dortmund Low Background Facility*, Bachelor's thesis, TU Dortmund, 2017.

Hannah Rullkötter: *Gammaspektroskopische Vermessung einer ^{22}Na-Probe und Monte Carlo Simujlationsstudien zur Abschirmung eines Germaniumdetektors*, Master's thesis, TU Dortmund, 2018.

Miriam Schwarze: *Monte-Carlo-Simulationsstudien eines Anti-Compton-Vetos für*

Germaniumdetektoren, Bachelor's thesis, TU Dortmund, 2018.

Simon Jansen: *Verhalten eines neuen digitalen zeitaufgelösten Auslesesystems für die Dortmund Low Background Facility bei unterschiedlich hohen Zählraten*, Bachelor's thesis, TU Dortmund, 2018.

Samantha Kauer: *Gammaspektrometrische Untersuchung der Aktivierung von Titanproben in der Protonentherapie in Hinblick auf klinische Anwendungen und Berechnung der Aktivierungswirkungsquerschnitte*, Master's thesis, TU Dortmund, 2018.

Claus Maximilian Bäcker: *Untersuchung der* $^{nat}\mathrm{C}(p,x)^{11}\mathrm{C}$*-Anregungsfunktion für Protonenenergien von* 100 *bis* 230 MeV *mittels Gammaspektrometrie*, Master's thesis, TU Dortmund, 2018.

Publications

Scientific Articles

Christian Bäumer, Claus Maximilian Bäcker, ..., **Christian Nitsch**, ...
Measurement of absolute activation cross sections from carbon and aluminum for proton therapy
Nuclear Instruments and Methods in Physics Research Section A, Volume 440, 75-81, 2019

Lucas Bodenstein-Dresler, Yingjie Chu, ..., **Christian Nitsch**, ...
Quenching of g_A deduced from the β-spectrum shapeof ^{113}Cd measured by the COBRA experiment
submitted to Physical Review Letters, 2018

Christian Nitsch, Marcel Gerhardt, Claus Gößling and Kevin Kröninger
Improvements to the muon veto of the Dortmund Low Background Facility
Applied Radiation and Isotopes, Volume 126, 201-203
Proceedings of the 7th International Conference on Radionuclide Metrology – Low-Level Radioactivity Measurement Techniques, 2017

Jan-Hendrick Arling, Marcel Gerhardt, ..., **Christian Nitsch**, ...
Suppression of alpha-induced lateral surface events in the COBRA experiment using CdZnTe detectors with an instrumented guard-ring electrode
Journal of Instrumentation, Volume 12, 2017

Jochen Ebert, Daniel Gehre, ..., **Christian Nitsch**, ...
Results of a search for neutrinoless double-β decay using the COBRA demonstrator
Physical Review C, Volume 94, 024603, 2016

Christian Nitsch, Holger Gastrich, Claus Gößling, Reiner Klingenberg, Kevin Kröninger, Till Neddermann, Thomas Quante and Kai Zuber
The Dortmund Low Background Facility — Low-background gamma ray spectrometry

with an artificial overburden
Applied Radiation and Isotopes, Volume 112, 165-176, 2016

Jochen Ebert, Daniel Gehre, ..., **Christian Nitsch**, ...
Long-term stability of underground operated CZT detectors based on the analysis of intrinsic ^{113}Cd β^--decay
Nuclear Instruments and Methods in Physics Research Section A, Volume 821, 109-115, 2016

Jochen Ebert, Daniel Gehre, ..., **Christian Nitsch**, ...
The COBRA demonstrator at the LNGS underground laboratory
Nuclear Instruments and Methods in Physics Research Section A, Volume 806, 159-168, 2016

Jochen Ebert, Matthew Fritts, ..., **Christian Nitsch**, ...
Characterization of a large CdZnTe coplanar quad-grid semiconductor detector
Nuclear Instruments and Methods in Physics Research Section A, Volume 807, 114-120, 2016

Conference Talks

C. Nitsch
The Dortmund Low Background Facility
CELLAR Meeting
Dezember 08 – 09, 2015, Monaco (Monaco)

Conference Poster

C. Nitsch
The Dortmund Low Background Facility
7th International Conference on Radionuclide Metrology – Low-Level Radioactivity Measurement Techniques
September 26 – 30, 2016, Seattle (United States)

C. Nitsch
Experimental Study on Radioactivity in Brass Collimators Induced During Proton-Beam Therapy
Neutron and Ion Dosimetry Symposium (NEUDOS-13)
May 14 – 19, 2017, Krakow (Poland)

Bibliography

[A+14] ABGRALL, N. ET AL. *The Majorana Demonstrator Neutrinoless Double-Beta Decay Experiment*. *Adv. High Energy Phys.* (2014). 2014:365–432.

[A+17a] AKIMOV, D. ET AL. *Observation of Coherent Elastic Neutrino-Nucleus Scattering*. *Science* (2017). 357(6356):1123–1126.

[A+17b] APRILE, E. ET AL. *The XENON1T Dark Matter Experiment*. *Eur. Phys. J.* (2017). C77(12):881.

[AAA+03] AGOSTINELLI, S. ET AL. *Geant4 — a simulation toolkit*. *Nucl. Instrum. Methods Phys. Res. A* (2003). 506(3):250–303.

[AAA+09] AHARMIM, B. ET AL. *Measurement of the cosmic ray and neutrino-induced muon flux at the Sudbury neutrino observatory*. *Phys. Rev. D* (2009). 80.

[AAA+15] AIELLO, S. ET AL. *Measurement of the atmospheric muon depth intensity relation with the NEMO Phase-2 tower*. *Astropart. Phys.* (2015). 66:1 – 7.

[AAA+16] ABGRALL, N. ET AL. *The Majorana Demonstrator radioassay program*. *Nucl. Instrum. Methods Phys. Res. A* (2016). 828:22 – 36.

[AAA+18a] AALSETH, C. E. ET AL. *Search for Neutrinoless Double-β Decay in ^{76}Ge with the Majorana Demonstrator*. *Phys. Rev. Lett.* (2018). 120:132502.

[AAA+18b] AARTSEN, M. ET AL. *Multimessenger observations of a flaring blazar coincident with high-energy neutrino IceCube-170922A*. *Science* (2018). 361(6398).

[AAA+18c] AARTSEN, M. ET AL. *Neutrino emission from the direction of the blazar TXS 0506+056 prior to the IceCube-170922A alert*. *Science* (2018). 361(6398):147–151.

[AAD68] ALLKOFER, O. C., ANDRESEN, R. D. and DAU, W. D. *The muon spectra near the geomagnetic equator*. *Can. J. Phys.* (1968). 46(10):S301–S305.

[AAdA+17] ABRAHÃO, T. ET AL. *Cosmic-muon characterization and annual modulation measurement with Double Chooz detectors*. *J. Cosmol. Astropart. Phys.* (2017). 2017(02):017.

[ABB+] AN, F. ET AL. *Seasonal variation of the underground cosmic muon flux observed at Daya Bay*. *J. Cosmol. Astropart. Phys.* 2018(01):001.

[ABB+16] ANGLOHER, G. ET AL. *Results on light dark matter particles with a low-threshold CRESST-II detector*. *Eur. Phys. J. C* (2016). 76(1):25.

[ABB+18] AGOSTINI, M. ET AL. *Improved Limit on Neutrinoless Double-β Decay of* ^{76}Ge *from GERDA Phase II*. *Phys. Rev. Lett.* (2018). 120:132503.

[ACD71] ALLKOFER, O. C., CARSTENSEN, K. and DAU, W. D. *The absolute cosmic ray muon spectrum at sea level*. *Phys. Lett. B* (1971). 36(4):425–427.

[AMG13] AKBARI, K., MAHMOUDI, J. and GHANBARI, M. *Influence of indoor air conditions on radon concentration in a detached house*. *J. Environ. Radioact.* (2013). 116:166 – 173.

[B+06] BOGDANOVA, L. N. ET AL. *Cosmic muon flux at shallow depths underground*. *Phys. Atom. Nucl.* (2006). 69:1293–1298.

[B+07] BUDJAS, D. ET AL. *Highly Sensitive Gamma-Spectrometers of GERDA for Material Screening: Part 2* (2007).

[B+12a] BELLINI, G. ET AL. *Cosmic-muon flux and annual modulation in Borexino at 3800 m water-equivalent depth*. *J. Cosmol. Astropart. Phys.* (2012). 1205:15.

[B+12b] BERINGER, J. ET AL. *Review of Particle Physics*. *Phys. Rev. D* (2012). 86:010001.

[BAH+17] BÄUMER, C. ET AL. *Dosimetry intercomparison of four proton therapy institutions in Germany employing spot scanning*. *Zeitschrift für Medizinische Physik* (2017). 27(2):80 – 85.

[BBC+52] BARRETT, P. H. ET AL. *Interpretation of Cosmic-Ray Measurements Far Underground*. *Rev. Mod. Phys.* (1952). 24:133–178.

[BBG+19] BÄUMER, C. ET AL. *Measurement of absolute activation cross sections from carbon and aluminum for proton therapy*. *Nucl. Instrum. Methods Phys. Res. B* (2019). 440:75 – 81.

[BBI+17] BANDAC, I. ET AL. *Ultra-low background and environmental measurements at Laboratorio Subterráneo de Canfranc (LSC)*. *Appl. Radiat. Isot.* (2017). 126:127 – 129. Proceedings of the 7th International Conference on Radionuclide Metrology – Low-Level Radioactivity Measurement Techniques.

[BBL+18] BREIER, R. ET AL. *Environmental radionuclides as contaminants of HPGe gamma-ray spectrometers: Monte Carlo simulations for Modane underground laboratory*. *J. Environ. Radioact.* (2018). 190-191:134 – 140.

[BCC+99] BELLOTTI, R. ET AL. *Balloon measurements of cosmic ray muon spectra in the atmosphere along with those of primary protons and helium nuclei over midlatitude*. *Phys. Rev. D* (1999). 60:052002.

[BCC+14] BÖHLEN, T. ET AL. *The FLUKA Code: Developments and Challenges for High Energy and Medical Applications*. *Nuclear Data Sheets* (2014). 120:211 – 214.

[BD+18] BODENSTEIN-DRESLER, L. ET AL. *Quenching of g_A deduced from the β-spectrum shape of ^{113}Cd measured with the COBRA experiment* (2018). Submitted.
URL `https://arxiv.org/abs/1806.02254`

[BEH+17] BRUDANIN, V. ET AL. *Development of the ultra-low background HPGe spectrometer OBELIX at Modane underground laboratory*. *J. Instrum.* (2017). 12(02):P02004.

[BFA+11] BAUDIS, L. ET AL. *Gator: a low-background counting facility at the Gran Sasso Underground Laboratory*. *J. Instrum.* (2011). 6(08):P08010.

[BFM+89] BERGER, C. ET AL. *Experimental study of muon bundles observed in the Fréjus detector*. *Phys. Rev. D* (1989). 40:2163–2171.

[BGK+17] BÄUMER, C. ET AL. *Comprehensive clinical commissioning and validation of the RayStation treatment planning system for proton therapy with active scanning and passive treatment techniques* (2017). 43:15–24.

[BHS+10] BERGER, M. J. ET AL. *XCOM: Photon Cross Section Database (version 1.5)*. Website, National Institute of Standards and Technology (NIST), Gaithersburg, MD. (2010).
URL `http://physics.nist.gov/xcom`

[BKPS15] BAUDIS, L. ET AL. *Cosmogenic activation of xenon and copper*. *Eur. Phys. J. C* (2015). 75(10):485.

[BLP17] BREIER, R., LAUBENSTEIN, M. and POVINEC, P. *Monte Carlo simulation of background characteristics of a HPGe detector operating underground in the Gran Sasso National Laboratory*. *Appl. Radiat. Isot.* (2017). 126:188 – 190. Proceedings of the 7th International Conference on Radionuclide Metrology – Low-Level Radioactivity Measurement Techniques.

[BMN+98] BUGAEV, E. V. ET AL. *Atmospheric muon flux at sea level, underground and underwater*. *Phys. Rev. D* (1998). 58:054001.

[Bos05] BOSSEW, P. *A very long-term HPGe-background gamma spectrum*. *Appl. Radiat. Isot.* (2005). 62(4):635 – 644.

[BR97] BRUN, R. and RADEMAKERS, F. *ROOT — An object oriented data analysis framework*. *Nucl. Instrum. Methods Phys. Res. A* (1997). 389(1–2):81–86. See also `http://root.cern.ch/`.

[Bun18] BUNDESAMT FÜR STRAHLENSCHUTZ (BFS). *Radon in buildings*. Website (2018).
URL `http://www.bfs.de/EN/home/home_node.html`

[BVP18] BAGINOVA, M., VOJTYLA, P. and POVINEC, P. P. *Investigation of neutron interactions with Ge detectors*. *Nucl. Instrum. Methods Phys. Res. A* (2018). 897:22 – 31.

[Can08] CANBERRA INDUSTRIES, INC. *Ultra Low-Background Cryostats (ULB)*. Website (2008).
URL `http://www.canberra.com/products/detectors/pdf/Ultra-LowBkgrnd-Cryo-SS-CSP0173.pdf`

[Can09] CANBERRA INDUSTRIES, INC. *Standard Electrode Coaxial Ge Detectors (SEGe)*. Website (2009).
URL `http://www.canberra.com/products/detectors/pdf/SEGe-SS-C37419.pdf`

[Can10] CANBERRA INDUSTRIES, INC. *Inner drawing p-type, S/N 07064*. Data sheet (2010).

[Ceb17] CEBRIÁN, S. *Cosmogenic activation of materials*. *Int. J. Mod. Phys. A* (2017). 32(30):1743006.

[CIG+13] CHO, J. ET AL. *Feasibility of proton-activated implantable markers for proton range verification using PET*. *Phys. Med. Biol.* (2013). 21(58):7497–7512.

[CMF+14] CHEN, H. ET AL. *Dosimetric evaluation of hybrid brass/stainless-steel apertures for proton therapy*. *Phys. Med. Biol.* (2014). 59(17):5043.

[CMS10] CESANA, A., MAURO, E. and SILARI, M. *Induced radioactivity in a patient-specific collimator used in proton therapy*. *J. Instrum.Nucl. Instrum. Methods Phys. Res. B* (2010). 268(13):2272 – 2280.

[Con10] CONFERENCE, I. G. *Production and Supply of Molybdenum-99 - NTR2010 Supplement*. In *General Conference Archive*. IAEA General Conference (2010).

[Cur68] CURRIE, L. *Limits for qualitative detection and quantitative determination. Application to radiochemistry* (1968). 40:586–593.

[DCD+] DOWDELL, S. J. ET AL. *Monte Carlo study of the potential reduction in out-of-field dose using a patient-specific aperture in pencil beam scanning proton therapy*. *Phys. Med. Biol.* 57(10):2829.

[DIN97] *Nachweisgrenze und Erkennungsgrenze bei Kernstrahlungsmessungen - Teil 5: Zählende hochauflösende gammaspektrometrische Messungen ohne Berücksichtigung des Probenbehandlungseinflusses - Beispiele und Erläuterungen* (1997).

[DIN11] *Bestimmung der charakteristischen Grenzen (Erkennungsgrenze, Nachweisgrenze und Grenzen des Vertrauensbereichs) bei Messungen ionisierender Strahlung – Grundlagen und Anwendungen* (2011).

[DRW+09] DAWSON, J. ET AL. *An Investigation into the ^{113}Cd Beta Decay Spectrum using a CdZnTe Array*. *Nuclear Physics A* (2009). 818(3–4):264–278.

[E+16a] EBERT, J. ET AL. *Characterization of a large CdZnTe coplanar quad-grid semiconductor detector*. *Nucl. Instrum. Methods Phys. Res. A* (2016). 806:159–168.

[E+16b] EBERT, J. ET AL. *The COBRA demonstrator at the LNGS underground laboratory*. *Nucl. Instrum. Methods Phys. Res. A* (2016). 807:114–120.

[EAB+15] ERCHINGER, J. ET AL. *Development of a low background liquid scintillation counter for a shallow underground laboratory*. *Appl. Radiat. Isot.* (2015). 105:209 – 218.

[EFG+16] EBERT, J. ET AL. *Results of a search for neutrinoless double-β decay using the COBRA demonstrator*. *Phys. Rev. C* (2016). 94:024603.

[EGG+16] EBERT, J. ET AL. *Long-term stability of underground operated CZT detectors based on the analysis of intrinsic 113Cd β- decay*. *Nucl. Instrum. Methods Phys. Res. A* (2016). 821:109 – 115.

[ELJ] ELJEN TECHNOLOGY. 1300 W. Broadway, Sweetwater, TX 79556. URL `https://eljentechnology.com`

[EOA+17] ERCHINGER, J. ET AL. *Background characterization of an ultra-low background liquid scintillation counter*. *Appl. Radiat. Isot.* (2017). 126:168 – 170. Proceedings of the 7th International Conference on Radionuclide Metrology – Low-Level Radioactivity Measurement Techniques.

[ET] ET ENTERPRISES. 45 Riverside Way, Uxbridge, United Kingdom. URL `http://et-enterprises.com`

[FFEE15] FLUEHS, D. ET AL. *Polyethylene Naphthalate Scintillator: A Novel Detector for the Dosimetry of Radioactive Ophthalmic Applicators*. *Ocular Oncology and Pathology* (2015). 2:5–12.

[FFF+15] FAMULOK, N. ET AL. *Ultrasensitive detection method for primordial nuclides in copper with Accelerator Mass Spectrometry*. *J. Instrum.Nucl. Instrum. Methods Phys. Res. B* (2015). 361:193 – 196. The Thirteenth Accelerator Mass Spectrometry Conference.

[Fit16] FITZGERALD, R. *Corrections for the combined effects of decay and dead time in live-timed counting of short-lived radionuclides*. *Appl. Radiat. Isot.* (2016). 109:335 – 340. Proceedings of the 20th International Conference on Radionuclide Metrology and its Applications 8–11 June 2015, Vienna, Austria.

[FLRX18] FARZAN, Y. ET AL. *Probing neutrino coupling to a light scalar with coherent neutrino scattering*. *JHEP* (2018). 05:066.

[FSFR05] FERRARI, A. ET AL. *FLUKA: A multi-particle transport code (Program version 2005)* (2005).

[FSLQ97] FASSBENDER, M. ET AL. *Experimental studies and nuclear model calculations on the formation of radioactive products in interactions of medium energy protons with copper, zinc and brass: Estimation of collimator activation in proton therapy facilities*. *Appl. Radiat. Isot.* (1997). 48(9):1221 – 1230.

[Gas09] GASTRICH, H. *Die Dortmund Low Background Facility - Aufbau einer inneren Abschirmung und Inbetriebnahme des HPGe-Detektors*. Diploma thesis, TU Dortmund (May 2009).

[GCB+17] GREENWOOD, L. ET AL. *Low-background gamma-ray spectrometry for the international monitoring system*. *Appl. Radiat. Isot.* (2017). 126:240 – 242. Proceedings of the 7th International Conference on Radionuclide Metrology – Low-Level Radioactivity Measurement Techniques.

[Ger14] GERHARDT, M. *Entwicklung und Inbetriebnahme einer zusätzlichen Wand des Myon-Vetos für die DLB*. Bachelor's thesis, TU Dortmund (Aug. 2014).

[Ger16] GERHARDT, M. *Monte Carlo Simulation of the Muon-induced Background and Completion of the Muon Veto of the Dortmund Low Background Facility*. Master's thesis, TU Dortmund (Sep. 2016).

[Gil08] GILMORE, G. R. *Practical gamma-ray spectrometry*. John Wiley & Sons, Ltd (2008).

[GMS01] GROOM, D. E., MOKHOV, N. V. and STRIGANOV, S. I. *Muon stopping power and range tables 10 MeV–100 TeV*. *Atomic Data and Nuclear Data Tables* (2001). 78(2):183–356. `http://pdg.lbl.gov/2012/AtomicNuclearProperties/adndt.pdf`.

[Gri01] GRIEDER, P. K. (Editor). *Cosmic Rays at Earth*. Amsterdam (2001).

[Hay15] HAYNES, W. *CRC Handbook of Chemistry and Physics*. CRC Press, 96 ed. (2015).

[HCK+00] HULT, M. ET AL. *Recent developments in ultra low-level γ-ray spectrometry at IRMM. Appl. Radiat. Isot.* (2000). 53(1):225 – 229.

[Heu93] HEUSSER, G. *Cosmic ray-induced background in Ge-spectrometry. J. Instrum.Nucl. Instrum. Methods Phys. Res. B* (1993). 83(1-2):223–228.

[Heu95] HEUSSER, G. *Low-radioactivity background techniques. Annual Review of Nuclear and Particle Science* (1995). 45(1):543–590.

[HJN+18] HANUŠOVÁ, T. ET AL. *Activation of QA devices and phantom materials under clinical scanning proton beams—a gamma spectrometry study. Phys. Med. Biol.* (2018). 63(11):115014.

[HJW00] HURTGEN, C., JEROME, S. and WOODS, M. *Revisiting Currie — how low can you go? Appl. Radiat. Isot.* (2000). 53(1):45 – 50.

[HLN06] HEUSSER, G., LAUBENSTEIN, M. and NEDER, H. *Low-level germanium gamma-ray spectrometry at the µBq/kg level and future developments towards higher sensitivity*. In POVINEC, P. and SANCHEZ-CABEZA, J. (Editors), *Radionuclides in the Environment - Int. Conf. On Isotopes in Env. Studies*, vol. 8 of *Radioactivity in the Environment*, pp. 495 – 510 (2006).

[HMH16] HAKENMÜLLER, J., MANESCHG, W. and HEUSSER, G. *Simulation and verification of the cosmogenic background at the shallow depth GIOVE detector. Journal of Physics: Conference Series* (2016). 718(4):042028.

[HMS+18] HULT, M. ET AL. *Characterisation of an ultra low-background point contact HPGe well-detector for an underground laboratory. Appl. Radiat. Isot.* (2018). 134:446 – 449. ICRM 2017 Proceedings of the 21st International Conference on Radionuclide Metrology and its Applications.

[HWH+15] HEUSSER, G. ET AL. *GIOVE: a new detector setup for high sensitivity germanium spectroscopy at shallow depth. Eur. Phys. J. C* (2015). 75(11):531.

[Ian16] IANNI, A. *The Canfranc Underground Laboratory: a multidisciplinary underground facility. Journal of Physics: Conference Series* (2016). 675(1):012002.

[Ion] ION BEAM APPLICATIONS (IBA). Chemin du Cyclotron, 3 – 1348 Louvain-la-Neuve, Belgique.
URL `https://www.iba-worldwide.com`

[ISO00] *Determination of detection limit and decision threshold for ionizing radiation measurements - Part 3: Fundamentals and application to counting measurements by high resolution gamma spectrometry, without the influence of sample treatment* (2000).

[Jan18] JANSEN, S. *Verhalten eines neuen digitalen zeitaufgelösten Auslesesystems für die Dortmund Low Background Facility bei unterschiedlich hohen Zählraten*. Bachelor's thesis, TU Dortmund (Jul. 2018).

[Jun74] JUNOD, E. *Corrections of counting losses in gamma-spectrometry of short-lived radionuclides*. *Journal of Radioanalytical Chemistry* (1974). 20:113–134.

[K+99] KREMER, J. ET AL. *Measurements of ground-level muons at two geomagnetic locations*. *Phys. Rev. Lett.* (1999). 83:4241–4244.

[K+04] KOEHLER, M. ET AL. *Reference measurements of low levels of ^{60}Co in steel*. *Appl. Radiat. Isot.* (2004). 61:207 – 211.

[K+10] KHACHATRYAN, V. ET AL. *Measurement of the charge ratio of atmospheric muons with the CMS detector*. *Phys. Lett. B* (2010). 692:83–104.

[KAC12] KIM, J. S., AN, S. J. and CHUNG, Y. H. *New concept of a range verification system for proton therapy using a photon counting detector*. *Nucl. Instrum. Methods Phys. Res. A* (2012). 677:18 – 21.

[KCQ09] KETTERN, K., COENEN, H. and QAIM, S. *Quantification of radiation dose from short-lived positron emitters formed in human tissue under proton therapy conditions*. *Radiation Physics and Chemistry* (2009). 78(6):380 – 385.

[KDL+09] KÖHLER, M. ET AL. *A new low-level γ-ray spectrometry system for environmental radioactivity at the underground laboratory Felsenkeller*. *Appl. Radiat. Isot.* (2009). 67(5):736 – 740. 5th International Conference on Radionuclide Metrology - Low-Level Radioactivity Measurement Techniques ICRM-LLRMT'08.

[KKP17] KUČERA, J., KAMENÍK, J. and POVINEC, P. P. *Radiochemical separation of mostly short-lived neutron activation products*. *Journal of Radioanalytical and Nuclear Chemistry* (2017). 311(2):1299–1307.

[Köt12] KÖTTIG, T. *Sensitivity Studies of CdZnTe Semiconductor Detectors for the COBRA Experiment*. Ph.D. thesis, TU Dortmund (Sep. 2012).

[Lab18] LABORATOIRE NATIONAL DE MÉTROLOGIE ET D'ESSAIS - LABORATOIRE NATIONAL HENRI BECQUEREL (LNE-LNHB). *Decay Data Evaluation Project*. Website (2018).
URL `http://www.nucleide.org/DDEP_WG/DDEPdata.htm`

[Lan44] LANDAU, L. *On the energy loss of fast particles by ionization*. *J. Phys.(USSR)* (1944). 8:201–205.

[Lau17] LAUBENSTEIN, M. *Screening of materials with high purity germanium detectors at the Laboratori Nazionali del Gran Sasso*. *International Journal of Modern Physics A* (2017). 32(30):1743002.

[LBP+15] LOAIZA, P. ET AL. *Obelix, a new low-background HPGe at Modane Underground Laboratory*. *AIP Conference Proceedings* (2015). 1672(1):130002.

[LCY+12] LEE, S. H. ET AL. *Evaluation of radioactivity induced by patient-specific devices in proton therapy*. *Journal of the Korean Physical Society* (2012). 60(1):125–128.

[Leo94] LEO, W. R. *Techniques for Nuclear and Particle Physics Experiments - A How-To Approach*. Berlin Heidelberg New York, 2nd rev ed. (1994).

[LH09] LAUBENSTEIN, M. and HEUSSER, G. *Cosmogenic radionuclides in metals as indicator for sea level exposure history*. *Appl. Radiat. Isot.* (2009). 67(5):750 – 754. 5th International Conference on Radionuclide Metrology - Low-Level Radioactivity Measurement Techniques ICRM-LLRMT'08.

[LHG+04] LAUBENSTEIN, M. ET AL. *Underground measurements of radioactivity*. *Appl. Radiat. Isot.* (2004). 61(2-3):167 – 172. Low Level Radionuclide Measurement Techniques - ICRM.

[Lib64] LIBBY, W. F. *Radiocarbon Dating*. *Nobel Lectures, Chemistry 1942-1962* (1964).

[Lib65] LIBBY, W. F. *Unsolved Problems in Physics: Tasks for the Immediate Future in Cosmic Ray Studies*. *Nobel Lectures, Physics 1922-1941* (1965).

[Lin15] LINKER, C. *Gammaspektrometrische Vermessung eines Radiopharmakons in der Domrtund Low Background Facility*. Bachelor's thesis, TU Dortmund (2015).

[LK12] L'ANNUNZIATA, M. F. and KESSLER, M. J. *Chapter 7 - Liquid Scintillation Analysis: Principles and Practice*. In L'ANNUNZIATA, M. F. (Editor), *Handbook of Radioactivity Analysis (Third Edition)*, pp. 423 – 573. Academic Press, Amsterdam, third edition ed. (2012).

[LLSL90] LINDSTROM, R. M. ET AL. *A low-background gamma-ray assay laboratory for activation analysis*. *Nucl. Instrum. Methods Phys. Res. A* (1990). 299(1):425 – 429.

[Luk94] LUKE, P. N. *Single-polarity charge sensing in ionization detectors using coplanar electrodes*. *Applied Physics Letters* (1994). 65:2884–2886.

[MBC17] M.J. BERGER1, M. Z., J.S. Coursey and CHANG, J. *Stopping-Power and Range Tables for Electrons, Protons, and Helium Ions*. Website, National Institute of Standards and Technology (NIST), Physical Measurement Laboratory (PML) (2017).
URL `https://dx.doi.org/10.18434/T4NC7P`

[MBCB+16] MEIJA, J. ET AL. *Isotopic compositions of the elements 2013 (IUPAC Technical Report)* (2016). 88:293–306.

[MEF+18] MAJOROVITS, B. ET AL. *PEN as self-vetoing structural material*. *AIP Conference Proceedings* (2018). 1921(1):090001.

[Miy73] MIYAKE, S. *Rapporteur Paper on Muons and Neutrinos*. *13th international Cosmic Ray Conference, Denver, 17-30 August 1973, Conference Papers, Volume 1* (1973). pp. 3638–3655.

[Mug18] MUGHABGHAB, S. *Recommended Thermal Cross Sections, Resonance Properties, and Resonance Parameters for Z = 1–60*. *Atlas of Neutron Resonances (Sixth Edition)* (2018). pp. 89 – 822.

[Muk12] MUKHERJEE, B. *Radiation safety issues relevant to proton therapy and radioisotope production medical cyclotrons*. *Radiat Prot Environ* (2012). 35(3):126–134.

[MZW+13] MIN, C. H. ET AL. *Clinical Application of In-Room Positron Emission Tomography for In Vivo Treatment Monitoring in Proton Radiation Therapy*. *International Journal of Radiation Oncology, Biology, Physics* (2013). 86(1):183–189.

[NCDDV17] NISI, S. ET AL. *ICP-MS measurement of natural radioactivity at LNGS*. *International Journal of Modern Physics A* (2017). 32(30):1743003.

[Ned09] NEDDERMANN, T. *Äußere Abschirmung und aktives Myon-Veto der Dortmund-Low-Background-HPGe-Facility*. Diploma thesis, TU Dortmund (Apr. 2009).

[Ned14] NEDDERMANN, T. *Material Screening by means of Low-level Gamma Ray Spectrometry with the Dortmund Low Background HPGe Facility*. Ph.D. thesis, TU Dortmund (Feb. 2014).

[NGG+16] NITSCH, C. ET AL. *The Dortmund Low Background Facility — Low-background gamma ray spectrometry with an artificial overburden*. *Appl. Radiat. Isot.* (2016). 112:165–176.

[NGGK17] NITSCH, C. ET AL. *Improvements to the muon veto of the Dortmund Low Background Facility*. *Appl. Radiat. Isot.* (2017). 126:201 – 203. Proceedings of the 7th International Conference on Radionuclide Metrology – Low-Level Radioactivity Measurement Techniques.

[Nic] NICHIPOROV, D. *Verification of absolute ionization chamber dosimetry in a proton beam using carbon activation measurements*. *Medical Physics* 30(5):972–978.

[Nie08] NIESE, S. *Underground laboratories for low-level radioactivity measurements*. In *Analysis of Environmental Radionuclides*, vol. 11, pp. 209 – 239. Elsevier (2008).

[Nit12] NITSCH, C. *Entwicklung einer alternativen Methode zur Szintillatorauslese für das Myon-Veto der DLB*. Bachelor's thesis, TU Dortmund (Sep. 2012).

[Nit14] NITSCH, C. *Upgrade of the Muon Veto and Measurements with the Dortmund Low Background Facility*. Master's thesis, TU Dortmund (Sep. 2014).

[NNDCN18] NATIONAL NUCLEAR DATA CENTER (NNDC). *NuDat 2.7*. Website (2018).
URL `http://www.nndc.bnl.gov/nudat2/`

[Noba] *The Nobel Prize in Chemistry 1960*. Website.
URL `https://www.nobelprize.org/prizes/chemistry/1960/summary/`

[Nobb] *The Nobel Prize in Physics 1936*. Website.
URL `https://www.nobelprize.org/prizes/physics/1936/summary/`

[NS13] NEGRET, A. and SINGH, B. *Nuclear Data Sheets for A = 75*. *Nuclear Data Sheets* (2013). 114(8):841 – 1040.

[NSTS11] NAKAMURA, H. ET AL. *Evidence of deep-blue photon emission at high efficiency by common plastic*. *EPL (Europhysics Letters)* (2011). 95(2):22001.

[Num07] NUMAJIRI, M. *Evaluation of the radioactivity of the pre-dominant gamma emitters in components used at high-energy proton accelerator facilities*. *Radiation Protection Dosimetry* (2007). 123(4):417–425.

[NZ15] NEWHAUSER, W. D. and ZHANG, R. *The physics of proton therapy*. *Phys. Med. Biol.* (2015). 60(8):R155.

[O+14] OLIVE, K. A. ET AL. *Review of Particle Physics*. *Chin. Phys.* (2014). C38:090001.

[Par18] PARTICLE THERAPY CO-OPERATIVE GROUP (PTCOG). Website (2018).
URL `https://www.ptcog.ch`

[Pau71] PAUL, J. M. *The density effect and rate of energy loss in common plastic scintillators*. *Nuclear Instruments and Methods* (1971). 96(1):51–59.

[PBE+18] PFEILER, T. ET AL. *Experimental validation of a 4D dose calculation routine for pencil beam scanning proton therapy*. *Zeitschrift für Medizinische Physik* (2018). 28(2):121 – 133.

[PBJV08] POVINEC, P. P. ET AL. *New Isotope Technologies in Environmental Physics*. *Acta Physica Slovaca* (2008). 58:1 – 154.

[PCLP04] POVINEC, P., COMANDUCCI, J.-F. and LEVY-PALOMO, I. *IAEA-MEL's underground counting laboratory in Monaco—background characteristics of HPGe detectors with anti-cosmic shielding*. *Appl. Radiat. Isot.* (2004). 61(2):85 – 93. Low Level Radionuclide Measurement Techniques - ICRM.

[PDM+17] PETHURAJ, S. ET AL. *Measurement of cosmic muon angular distribution and vertical integrated flux by 2 m × 2 m RPC stack at IICHEP-Madurai*. *J. Cosmol. Astropart. Phys.* (2017). 2017(09):021.

[Pel11] PELLICCIONI, M. *Radiation protection at Hadron therapy facilities*. *Radiation Protection Dosimetry* (2011). 146(4):407–413.

[Pov17] POVINEC, P. P. *Analysis of radionuclides at ultra-low levels: A comparison of low and high-energy mass spectrometry with gamma-spectrometry for radiopurity measurements*. *Appl. Radiat. Isot.* (2017). 126:26 – 30. Proceedings of the 7th International Conference on Radionuclide Metrology – Low-Level Radioactivity Measurement Techniques.

[Pov18] POVINEC, P. P. *New ultra-sensitive radioanalytical technologies for new science*. *Journal of Radioanalytical and Nuclear Chemistry* (2018). 316(3):893–931.

[Qua12] QUANTE, T. *Upgrade of the Active Muon Veto and Software Development for the Dortmund Low Background Facility*. Master's thesis, TU Dortmund (Sep. 2012).

[R+96] RHODE, W. ET AL. *Limits on the flux of very high-energetic neutrinos with the Frejus detector*. *Astropart. Phys.* (1996). 4:217–225.

[RCLM88] RINDI, A. ET AL. *Underground Neutron Flux Measurement*. *Nucl. Instrum. Meth.* (1988). A272:871.

[Rey06] REYNA, D. *A Simple parameterization of the cosmic-ray muon momentum spectra at the surface as a function of zenith angle* (2006).

[Rul18] RULLKÖTTER, H. *Gammaspektroskopische Vermessung einer* ^{22}Na*-Probe und Monte Carlo Simujlationsstudien zur Abschirmung eines Germaniumdetektors*. Master's thesis, TU Dortmund (May 2018).

[Sai18] SAINT-GOBAIN CRYSTALS. *Datasheet BC-408* (2018). Hiram, USA. URL `www.detectors.saint-gobain.com`

[ŠAK+92] ŠKORO, G. P. ET AL. *Environmental neutrons as seen by a germanium gamma-ray spectrometer*. *Nucl. Instrum. Methods Phys. Res. A* (1992). 316(2–3):333 – 336.

[SCI] SCIONIX, H. B. *3980 CC Bunnik, The Netherlands*.
URL `https://scionix.nl`

[SHM+14] SIVERS, M. ET AL. *Low-level γ-ray spectrometry at the underground laboratory Garching*. *Appl. Radiat. Isot.* (2014). 91:49 – 56.

[Sis02] SISTERSON, J. *Selected radiation safety issues at proton therapy facilities*. *12th Biennial Radiation Protection and Shielding Division Topical Meeting* (2002).

[SOM+17] SEMKOVA, VALENTINA ET AL. *EXFOR - a global experimental nuclear reaction data repository: Status and new developments*. *EPJ Web Conf.* (2017). 146:07003.

[SRP+12] SMEETS, J. ET AL. *Prompt gamma imaging with a slit camera for real-time range control in proton therapy*. *Phys. Med. Biol.* (2012). 57(11).

[Tan18] TANABASHI, M. e. a. *Review of Particle Physics (RPP)*. *Phys. Rev. D* (2018). 98:030001.

[The96] THEODÓRSSON, P. *Measurement of weak radioactivity*. World Scientific (1996).

[THSKT06] TANG, A. ET AL. *Muon simulations for Super-Kamiokande, KamLAND and CHOOZ*. *Phys. Rev.* (2006). D74:053007.

[TNB+14] THOMADSEN, B. ET AL. *Potential Hazard Due to Induced Radioactivity Secondary to Radiotherapy: The Report of Task Group 136 of the American Association of Physicists in Medicine*. *Health Physics* (2014). 107(5).

[Ver17] VERBEEK, N. *Umsetzung Faraday Cup-basierter Dosimetrie im Nadelstrahlverfahren in der Protonentherapie*. Master's thesis, Heinrich Heine Universität Düsseldorf (2017).

[vSHRS16] VON SIVERS, M. ET AL. *The GeMSE facility for low-background gamma-ray spectrometry*. *J. Instrum.* (2016). 11(12):P12017.

[W+13] WU, Y.-C. ET AL. *Measurement of Cosmic Ray Flux in China JinPing underground Laboratory*. *Chin. Phys.* (2013). C37(8).

[Wah07] WAHL, W. *$\alpha\beta\gamma$-Table*. Handbook (2007).
URL `http://www.isus.de/english/table.htm`

[WB09] WIESER, M. E. and BERGLUND, M. *Atomic weights of the elements 2007 (IUPAC Technical Report)*. *Pure and Applied Chemistry* (2009). 81(11):2131–2156.

[WCR04] WROE, A. J., CORNELIUS, I. M. and ROSENFELD, A. B. *The role of nonelastic reactions in absorbed dose distributions from therapeutic proton beams in different medium*. *Medical Physics* (2004). 32(1):37–41.

[Web09] WEBER, M. *Experimente zum Entwurf einer Detektorabschirmung für ein neues Gamma - Spektrometer*. Diploma's thesis, Ruprecht - Karls - Universität Heidelberg (Nov. 2009).

[WEDJ14] WALKER, P. K. ET AL. *Radiation Safety Considerations in Proton Aperture Disposal*. *Health Physics* (2014). 106(4):523 – 527.

[Wil46] WILSON, R. R. *Radiological Use of Fast Protons*. *Radiology* (1946). 47(5):487–491.

[Wil04] WILKENS, J. *Activation of Implanted Gold Markers in Therapeutic Proton Beams*. *Physics Division - Massachusetts General Hospital, Department of Radiation Oncology* (2004).

[WMA+96] WORDEL, R. ET AL. *Study of neutron and muon background in low-level germanium gamma-ray spectrometry*. *Nucl. Instrum. Methods Phys. Res. A* (1996). 369(2-3):557–562.

[WMZ17] WEI, W.-Z., MEI, D.-M. and ZHANG, C. *Cosmogenic activation of germanium used for tonne-scale rare event search experiments*. *Astropart. Phys.* (2017). 96:24 – 31.

[WWL+16] WU, Q. ET AL. *Study on patient-induced radioactivity during proton treatment in hengjian proton medical facility*. *Appl. Radiat. Isot.* (2016). 115:235 – 250.

[WZK+17] WILSENACH, H. ET AL. *A low background ionisation chamber for alpha-spectroscopy*. *EPJ Web of Conferences* (2017). 146:10015.

[XLK15] XIE, D., LIAO, M. and KEARFOTT, K. J. *Influence of environmental factors on indoor radon concentration levels in the basement and ground*

floor of a building – A case study. *Radiation Measurements* (2015). 82:52 – 58.

[ZP18] ZERKIN, V. and PRITYCHENKO, B. *The experimental nuclear reaction data (EXFOR): Extended computer database and Web retrieval system*. *Nucl. Instrum. Methods Phys. Res. A* (2018). 888:31 – 43.

List of Figures

List of Tables